

ABSTRACT

ZHANG, YUQI. Bioresponsive Drug Delivery by Microneedle Patches. (Under the direction of Dr. Zhen Gu).

Transdermal drug delivery based on microneedle (MN) patches have been widely investigated as an attractive alternative administration route. The patches can enable drug transport through the skin in a painless, convenient, and continuous manner. By integrating with bioresponsive formulations that can respond to physiological signals to tune drug release rates, these smart patches have been spotlighted as a promising approach to improve therapeutic efficiency in the last decade. This thesis study focused on developing bioresponsive drug delivery systems based on MN patches for smart drug delivery to treat several diseases including thromboembolism, obesity, acne, and diabetes. In order to achieve long-term auto-anticoagulant regulation, a thrombin-responsive patch was developed to release heparin for the prevention of blood coagulation. The integration of the thrombin-cleavable peptide allowed real-time monitoring of blood thrombin concentrations and subsequent on-demand release of anticoagulant drug. A glucose-responsive patch loaded with browning agents was designed to locally induce adipose tissue transformation for obesity treatment. The local release triggered by blood glucose could effectively deliver drug to the subcutaneous adipocytes in a sustained manner, thus minimizing systemic side effects. In addition, an inflammatory signal-triggered patch was developed for acne treatment. Compared to commonly used anti-acne cream, enhanced efficacy toward dermis lesions could be achieved through the skin penetration by MNs. We also designed a self-regulated glucose-responsive insulin delivery system based on MN patches for diabetes treatment. The integration of H₂O₂ and pH-responsive insulin complexes enabled closed-loop glucose-mediated insulin delivery for blood glucose regulation.

© Copyright 2018 Yuqi Zhang

All Rights Reserved

Bioresponsive Drug Delivery by Microneedle Patches

by
Yuqi Zhang

A dissertation submitted to the Graduate Faculty of
North Carolina State University
in partial fulfillment of the
requirements for the degree of
Doctor of Philosophy

Biomedical Engineering

Raleigh, North Carolina

2018

APPROVED BY:

Dr. Zhen Gu
Committee Chair

Dr. Yevgeny Brudno

Dr. Ke Cheng

Dr. Matthew Fisher

BIOGRAPHY

Yuqi Zhang obtained her B.S. degree in chemistry in 2015 from Nanjing University. She then joined Prof. Zhen Gu's iMedication Laboratory in 2015 and has since been pursuing her Ph.D. degree in the Joint Department of Biomedical Engineering of the University of North Carolina at Chapel Hill and North Carolina State University. Her research interests include stimuli-responsive biomaterials and controlled drug delivery.

ACKNOWLEDGMENTS

I would first and foremost like to thank my advisor, Dr. Zhen Gu for his constant guidance and unwavering support. Dr. Gu is an exceptional innovator and advisor, whose enthusiasm in research always inspired me throughout my doctoral studies. Anytime I have a problem, he is willing to answer with his insightfulness. I would also like to thank my co-advisor, Dr. Yong Zhu, for his patient, guidance, and advice regarding my work. I am very grateful to the rest of my committee, Dr. Yevgeny Brudno, Dr. Ke Cheng, and Dr. Matthew Fisher, for agreeing to be part of my PhD journey and providing assistance and support for my research.

I would like to express my appreciation to all the current members as well as all the alumni of Prof. Zhen Gu's iMedication Laboratory for their support, company, and friendship. In addition, I would like to thank my collaborators, Dr. Qiang Li, Dr. John B. Buse, Dr. Qundong Shen, Dr. Caterina M. Gallippi, and Dr. Jacqueline H. Cole for their great efforts. I must also acknowledge all the faculties and staffs of the Joint Department of Biomedical Engineering at North Carolina State University and University of North Carolina at Chapel Hill.

Lastly, I would like to thank my families and friends who are always supportive, and my husband Jicheng Yu. This work would not have been possible without your companionship and encouragement.

Chapter 1 of this dissertation is a version of "Jicheng Yu, Yuqi Zhang, Anna R Kahkoska, Zhen Gu. Bioresponsive transcutaneous patches. *Current Opinion in Biotechnology* 48: 28-32 (2017)". Chapter 2 is a version of "Yuqi Zhang, Jicheng Yu, Jinqiang Wang, Nicholas J

Hanne, Zheng Cui, Chenggen Qian, Chao Wang, Hongliang Xin, Jacqueline H Cole, Caterina M Gallippi, Yong Zhu, Zhen Gu. Thrombin-responsive transcutaneous patch for auto-anticoagulant regulation. *Advanced Materials* 29: 1604043 (2017)". Chapter 3 is a version of "Yuqi Zhang, Qiongmeng Liu, Jicheng Yu, Shuangjiang Yu, Jinqiang Wang, Li Qiang, Zhen Gu. Locally induced adipose tissue browning by microneedle patch for obesity treatment. *ACS Nano* 11: 9223-9230 (2017)". Chapter 4 is a version of "Yuqi Zhang, Peijian Feng, Jicheng Yu, Jia Yang, Jiacheng Zhao, Jinqiang Wang, Qundong Shen, Zhen Gu. ROS-responsive microneedle patch for acne vulgaris treatment. *Advanced Therapeutics*, 1: 1800035 (2018)". Chapter 5 is a version of "Yuqi Zhang, Jinqiang Wang, Jicheng Yu, Di Wen, Anna R Kahkoska, Yue Lu, Xudong Zhang, John B Buse, Zhen Gu. Bioresponsive microneedles with a sheath structure for H₂O₂ and pH cascade-triggered insulin delivery. *Small* 14: 1704181 (2018)".

The work in this dissertation was supported by American Diabetes Association (ADA), Juvenile Diabetes Research Foundation (JDFR), National Institute of Health (NIH), National Science Foundation (NSF), Sloan Research Fellowship, Advanced Self-Powered Systems of Integrated Sensors and Technologies Center (ASSIST), North Carolina Translational and Clinical Sciences (NC TraCS), Clinical & Translational Science Awards (CTSA), Graduate Student Support Plan (GSSP) and various other grants that provided funding during my doctoral education.

TABLE OF CONTENTS

LIST OF TABLES	x
LIST OF FIGURES	xi
CHAPTER 1 INTRODUCTION	1
1.1 Introduction	1
1.2 pH-Responsive Transdermal Patches	2
1.3 Glucose-Responsive Transdermal Patches	3
1.4 Enzymes-Activated Transdermal Patches	6
1.5 Conclusions and Outlook	8
1.6 Dissertation Scope and Organization	9
CHAPTER 2 THROMBIN-RESPONSIVE TRANSCUTANEOUS PATCH FOR AUTO-ANTICOAGULANT REGULATION	11
2.1 Introduction	11
2.2 Experimental Section	14
2.2.1 Materials	14
2.2.2 LC-MS analysis of peptide cleavage	14
2.2.3 Synthesis of acrylate modified HA (<i>m</i> -HA)	14
2.2.4 Synthesis of HA-Pep conjugates	15
2.2.5 Synthesis of TR-HAHP conjugates	15
2.2.6 Synthesis of NR-HAHP conjugates	16
2.2.7 Preparation of TR-HAHP hydrogel	16
2.2.8 <i>In vitro</i> release studies	16
2.2.9 Anticoagulant assays	17

2.2.10 Fabrication of TR-HAHP MNs.....	18
2.2.11 Mechanical strength test	19
2.2.12 Skin penetration efficiency test.....	19
2.2.13 Biocompatibility analysis.....	19
2.2.14 <i>In vivo</i> thrombosis model.....	19
2.2.15 Tail bleeding test.....	20
2.2.16 Statistical analysis	20
2.3 Results and Discussion.....	21
2.3.1 Preparation and characterization of thrombin-responsive heparin hydrogel .	21
2.3.2 <i>In vitro</i> anticoagulant regulation evaluation	25
2.3.3 Fabrication and characterization of thrombin-responsive MNs.....	27
2.3.4 <i>In vivo</i> studies in a thrombolytic challenge mouse model	30
2.4 Conclusion	35
 CHAPTER 3 LOCALLY-INDUCED ADIPOSE TISSUE BROWNING BY	
MICRONEEDLE PATCH FOR OBESITY TREATMENT	
	37
3.1 Introduction.....	37
3.2 Experimental Section.....	39
3.2.1 Materials	39
3.2.2 Synthesis of pendant acetal-modified dextran (<i>m</i> -dextran)	40
3.2.3 Preparation of rosiglitazone-loaded dextran nanoparticles.....	40
3.2.4 <i>In vitro</i> release studies	41
3.2.5 Fabrication of browning agent MN patch.....	41
3.2.6 Mechanical strength test	42

3.2.7 Skin penetration efficiency test.....	42
3.2.8 <i>In vivo</i> browning studies in lean mice.....	43
3.2.9 Browning MN patch treatments on diet induced obesity (DIO) mice	43
3.2.10 RNA analysis	44
3.2.11 Statistical analysis	46
3.3 Results and Discussion.....	47
3.3.1 Synthesis and characterization of Rosi-loaded NPs.....	47
3.3.2 Fabrication and characterization of browning agent MN-array patch	50
3.3.3 <i>In vivo</i> studies of the MNs on lean mice.....	51
3.3.4 <i>In vivo</i> studies of the MNs on diet-induced obese mice	58
3.4 Conclusion	62
 CHAPTER 4 ROS-RESPONSIVE MICRONEEDLE PATCH FOR ACNE	
VULGARIS TREATMENT.....	
4.1 Introduction.....	63
4.2 Experimental Section.....	65
4.2.1 Materials	65
4.2.2 Synthesis of ROS-responsive crosslinker (TSPBA)	65
4.2.3 Preparation of RR-PVA hydrogels	66
4.2.4 Preparation of NR-PVA hydrogels	66
4.2.5 <i>In vitro</i> release profiles	66
4.2.6 <i>In vitro</i> antibacterial effect.....	67
4.2.7 Fabrication of ROS-responsive (RR) microneedle patch	67
4.2.8 Microneedle mechanical strength test.....	68

4.2.9 Oil adsorption capacity test of diatomaceous earth (DE)	69
4.2.10 <i>In vivo</i> acne treatment efficacy evaluation.....	69
4.2.11 Histological analysis of infected skin	69
4.2.12 Statistical analysis	70
4.3 Results and Discussion	70
4.3.1 Preparation and characterization of ROS-responsive gel	70
4.3.2 <i>In vitro</i> antibacterial effect evaluation	72
4.3.3 Fabrication and characterization of drug-loaded MN-array patch.....	73
4.3.4 <i>In vivo</i> antibacterial studies on an acne-mouse model.....	76
4.4 Conclusion	79
 CHAPTER 5 BIORESPONSIVE MICRONEEDLE WITH A SHEATH	
STRUCTURE FOR H₂O₂ AND pH CASCADE-TRIGGERED INSULIN	
DELIVERY	80
5.1 Introduction	80
5.2 Experimental Section	83
5.2.1 Materials	83
5.2.2 Synthesis of MPEG _{5K} -P(DMAEMA) _{6K}	83
5.2.3 Synthesis of MPEG _{5K} -P(DMAEMA-PBA) _{6K}	84
5.2.4 Synthesis of poly(DMAEMA).....	85
5.2.5 Synthesis of poly(DMAEMA-PBA).....	86
5.2.6 Synthesis of poly(vinyl alcohol) methacrylate	87
5.2.7 Rhodamine B or FITC labeled insulin or CAT.....	87
5.2.8 H ₂ O ₂ generation rate assay.....	88

5.2.9 Preparation of insulin-NCs or GOx-NCs.....	88
5.2.10 <i>In vitro</i> insulin release from the complex of insulin and poly(DMAEMA-PBA)	88
5.2.11 <i>In vitro</i> insulin (or GOx) release from Ins-NCs (or GOx-NCs) from the PVA methacrylate gel (with insulin as an example).....	89
5.2.12 Fabrication of microneedle array patch (with MN(G+C+I) as an example).....	89
5.2.13 Mechanical strength test	90
5.2.14 <i>In vitro</i> cytotoxicity assay	90
5.2.15 <i>In vivo</i> studies using streptozotocin-induced diabetic mice.....	91
5.2.16 <i>In vitro</i> skin penetration test	91
5.2.17 Animal experiment.....	91
5.2.18 Statistical analysis	91
5.3 Results and Discussion	92
5.3.1 Synthesis and characterization of nano-complexes	92
5.3.2 <i>In vitro</i> glucose-responsive insulin release	97
5.3.3 Fabrication and characterization of insulin-loaded MN-array patch	102
5.3.4 <i>In vivo</i> studies of the MNs for type 1 diabetes treatment	105
5.4 Conclusion	111
CHAPTER 6 SUMMARY AND OUTLOOK	112
REFERENCES	115

LIST OF TABLES

Table 1.1 Summary of recently developed bioresponsive transcutaneous patches.....	9
Table 2.1 Elemental analysis of <i>m</i> -HA, HP and TR-HAHP	21
Table 3.1 Q-PCR Primer sequences	45

LIST OF FIGURES

Figure 1.1 Typical physiological signals (bio-triggers) for bioresponsive transcutaneous patches.....	2
Figure 2.1 (a) Formation and mechanism of the feedback-controlled heparin delivery system based on thrombin-responsive HAHP (TR-HAHP) conjugate. (b) Schematic of the TR-HAHP MN array patch in response to thrombin. (c) <i>In vitro</i> accumulated FITC-labeled HP release from the TR-HAHP hydrogel in several thrombin concentrations at 37 °C. (d) Pulsatile release profile of FITC-HP from the TR-HAHP hydrogel (blue: w/o thrombin; pink: w/thrombin). (e) Fluorescence microscopy images of the TR-HAHP hydrogel in thrombin solution at indicated time points. Scale bar: 1 mm. Error bars indicate s.d. (n = 3).....	13
Figure 2.2 LCMS spectra of peptide (a) before and (b) after thrombin cleavage.....	22
Figure 2.3 Photographies of TR-HAHP gel before (left) and after (right) UV irradiation....	23
Figure 2.4 Fluorescence microscopy images of the TR-HAHP and NR-HAHP hydrogels in thrombin solutions at indicated time points.....	24
Figure 2.5 Release profiles of HP from TR-HAHP and NR-HAHP hydrogels in different concentrations thrombin solutions respectively. Error bars indicate s.d. (n=3) ...	24
Figure 2.6 <i>In vitro</i> anticoagulant capacity of the TR-HAHP hydrogel. (a) <i>In vitro</i> analysis of the activated thromboplastin time (aPTT) of untreated (HA), HP treated, non-cross-linked, and cross-linked TR-HAHP or NR-HAHP treated plasma. (b) Prothrombin time (PT) tests of plasma incubated with HA, HP, TR-HAHP, and NR-HAHP hydrogels. (c) Thrombin clotting time (TCT) of plasma added	

with various hydrogels. (d) Concentrations of F1+2 fragment after each incubation period (3 h) indicates that only the TR-HAHP hydrogel can effectively suppress the thrombin generation during the second incubation. Error bars indicate s.d. (n = 3) 26

Figure 2.7 Mechanical behavior of one TR-HAHP MN..... 28

Figure 2.8 Fabrication and *in vitro* characterization of the TR-HAHP MN array patch. (a) Photos of the MNs array. Scale bar: 1 mm. (b) A fluorescence microscopy image of rhodamine-labeled MN loaded with FITC-labeled TR-HAHP. Scale bar: 200 μm . (c) A SEM image of MNs. Scale bar: 200 μm . (d) Pulsatile release profile of FITC-HP from the TR-HAHP MNs. (blue: w/o thrombin; pink: w/thrombin). (e) Self-regulated FITC-HP release from MNs in different thrombin solutions. Error bars indicate s.d. (n = 3) 29

Figure 2.9 *In vivo* studies of the TR-HAHP patch for thrombosis prevention. (a) Photograph of a mouse transcutaneously administered with the MN array patch (left). H&E-stained microscopy image of mouse skin penetrated by one MN (right top) and the image of the trypan blue staining (right bottom) showing the penetration of the MN patch into the mouse skin. Scale bars are 100 μm and 1 mm, respectively. (b) Kaplan–Meier survival curves for the mice challenged with thrombin injection. Each group was pre-treated with HP *i.v.* injection or different types of the MN patch (HP: 200 U/kg). Shown are eight mice per treatment group. (c) Kaplan–Meier survival curves for thrombotic challenge mouse model 6 h post MN treatments (HP: 200 U/kg). Shown are eight mice per treatment group. (d) H&E-stained sections of mouse

skin tissue at the MN-treated sites. Scale bar: 100 μm . (e)	
Immunofluorescence images of mouse skin tissue stained with TUNEL assay (green) and Hoechst (blue). Scale bar: 50 μm	31
Figure 2.10 Skin puncture marks at 0, 1, 2 and 4 h post-treatment. Scale bar: 2 mm	31
Figure 2.11 Representative images of FITC-labeled TR-HAHP MNs and NR-HAHP MNs inserted into mice skins after injection of thrombin (1000 U/kg). The white dashed line indicates the boundary of the injected MN. Scale bar: 200 μm	33
Figure 2.12 Histological observation of the lungs of the mice treated with HA, HP, TR-HAHP and NR-HAHP MNs after challenge of thrombin. Scale bar: 100 μm	33
Figure 2.13 Histological observation of the lungs of the thrombotic challenge mice 6-h post treatment with HP <i>i.v.</i> injection, HP MNs, and TR-HAHP MNs Scale bar: 100 μm	34
Figure 2.14. H&E-stained skin sections administered HA, HP, TR-HAHP and NR-HAHP MNs (from left to right) with surrounding tissues 24 h postadministration of the MN-array patch. Scale bar: 100 μm	35
Figure 2.15 (a) Tail transection bleeding time and (b) amounts of red blood cells from the tail wound of animals pretreated with empty HA MN, HP MN, TR-HAHP MN, and NR-HAHP MN. Error bars indicate s.d. (n=5).....	35
Figure 3.1 Schematic illustration of the browning reagents-loaded transcutaneous MN patch. Nanoparticles (NPs) encapsulating rosiglitazone (Rosi), glucose oxidase (GOx), and catalase (CAT) are prepared from pH-sensitive acetal-modified dextran and coated with alginate. NPs are further loaded into the	

microneedle-array patch made of crosslinked hyaluronic acid (HA) matrix for the brown remodeling of the white fat 39

Figure 3.2 Scheme of synthesis and dissociation routes of *m*-dextran 48

Figure 3.3 Fabrication and characterization of browning reagent microneedles. (a) The average hydrodynamic sizes of Rosi NPs determined by DLS. (b) Relevant pH changes of dextran NPs with or without GOx in PBS buffer in the presence of 100 mg/dL glucose. (n=3) (c) *In vitro* accumulated Rosi release from the acid-degradable dextran NPs (w/ or w/o GOx) in PBS buffer containing 100 mg/dL glucose at 37°C. (n=3) (d) UV absorbance of NPs suspensions $A_{400\text{ nm}}$. (n=3) (e) SEM images of Rosi NPs incubated in PBS buffer with 100 mg/dL glucose at 37 °C on day 0 and day 4 (scale bar: 2 μm), inset pictures show the transparency change of the NPs suspension. (f) Comparable adipogenesis between Rosi NPs- and Rosi compound-treated PgKO-MEFs as assessed by *aP2* and *Perilipin* gene expression. (n=4). (g) Same level of browning induced by Rosi NPs or Rosi compound in the mature 3T3-L1 white adipocytes. (n=4). (h) SEM image of the MN array (scale bar: 200 μm). (i) Higher magnification of SEM imaging of MN tip confirmed that the MN was loaded with NPs (scale bar: 10 μm). (j) SEM image of MNs 3 days post administration. (scale bar: 200 μm) (k) Trypan blue staining image of mouse skin administered with MN patch (scale bar: 1 mm). Error bars indicate standard deviation (SD), two-tailed Student's *t*-test, * $P < 0.05$, ** $P < 0.01$ 49

Figure 3.4 Mechanical behavior of one NP-loaded MN 51

Figure 3.5 Fluorescence microscopy image of inguinal adipose tissue section after treatment of fluorescein isothiocyanate (FITC)-encapsulated NP through the microneedle patch (scale bar: 200 μm)..... 53

Figure 3.6 *In vivo* fluorescence imaging of the mouse treated with Cy5.5-labelled NPs-loaded MNs at different time points. Cy5.5-labelled non-degradable NPs without glucose specific enzyme were loaded into crosslinked HA MNs..... 53

Figure 3.7 *In vivo* fluorescence imaging of the MN-treated mice at different time points. The fluorescent signal showed the MN patch loaded with free Cy5.5 (upper panel) or Cy5.5-entrapped NPs (lower panel) 54

Figure 3.8 *In vivo* browning induction by MN patches in the lean mice. (a) H&E-stained section of the cross-sectional mouse inguinal adipose tissue treated with HA empty MN patch (left), Rosi NP-loaded MN patch (middle), and CL 316243 NP-loaded MN patch (right) (scale bar: 25 μm). (b) Q-PCR analysis of gene expression in inguinal WAT treated with MN patches loaded with HA empty vehicle (EV), Rosi, or CL 316243 (CL). NP-loaded MN patch. Error bars indicate standard error of the mean (SEM), two-tailed Student's *t*-test, * $P < 0.05$, ** $P < 0.01$ compared to EV (n=6)..... 55

Figure 3.9 Indirect calorimetric analysis of healthy mice treated with HA empty MN patch (EV), Rosi NP-loaded MN patch (Rosi), or CL 316243 NP-loaded MN patch (CL). (a) Body weight change after the 6-day treatment. (b) Normalized inguinal fat pad size. (c) Normalized epididymal fat pad size. (d) Average food intake during the treatment. (e) Locomotor activity during one 24-h dark/light cycle. The panel on the right is the area under curve (AUC). (f) Oxygen

consumption and AUC. (g) Respiration exchange ratio (RER) and AUC during one dark/light cycle. Error bars indicate SEM, two-tailed Student's *t*-test, * $P < 0.05$, ** $P < 0.01$ compared to EV (n=6) 57

Figure 3.10 *In vivo* antiobesity and antidiabetic effects of MN patches in an HFD-induced obese mouse model. (a) Picture illustrating the mice treated with browning agent patch on one inguinal side (red) and empty vehicle patch on the other side (blue). (b) Normalized body weight of mice without treatment or treated with browning agent patches. (c) IPGTT test in mice 2 weeks post-treatment. (d) Blood glucose levels of mice treated with browning agent patches or empty patches after 16 h fasting. (e) Normalized epididymal fat pad size in mice with different treatments. (f) Normalized weight of interscapular fat pad size in mice with different treatments. (g) Ratio of the treated inguinal fat pad size to untreated side. (h) Photos of two sides of inguinal adipose tissues from obese mice 4-weeks post treatment. (i) H&E staining of inguinal adipose tissues (scale bar: 50 μm). (j) Q-PCR analysis of adipocyte gene expressions in inguinal tissues. (b-g) Error bars indicate SD, two-tailed Student's *t*-test, * $P < 0.05$, ** $P < 0.01$ compared to EV (n=5); (j) Error bars indicate SEM, two-tailed Student's *t*-test, * $P < 0.05$, ** $P < 0.01$ compared to EV (n=5) 60

Figure 3.11 H&E-stained skin sections administered empty, Rosi NP-loaded, and CL 316243 NP-loaded MNs (from left to right) with surrounding tissues after one month treatment (scale bar: 100 μm) 62

Figure 4.1 Schematic illustration of the formation and mechanism of a ROS-responsive microneedle patch for acne vulgaris treatment 65

Figure 4.2 Synthesis route of ROS-responsive linker TSPBA	71
Figure 4.3 <i>In vitro</i> responsiveness and antibacterial effect of the RR-PVA gel. a) Degradation of RR-PVA gel in the PBS solution with 1 mM H ₂ O ₂ or without H ₂ O ₂ . b) Accumulated release profile of CDM from RR-PVA gel with or without H ₂ O ₂ . c) Quantitative analysis of colony-forming units (CFUs) in each group. d) <i>P. acne</i> suspension cultured on RCM agar plate for 72 h, with addition of PBS buffer, the incubation medium with RR-PVA gel in the absence of H ₂ O ₂ , free CDM solution and the incubation medium with RR-PVA gel in the presence of H ₂ O ₂ . Error bars indicate s.d. (n = 3), two-tailed Student's <i>t</i> -test, * <i>P</i> <0.05.....	71
Figure 4.4 Incubation of NR-PVA gel in PBS buffer with 10 mM H ₂ O ₂ at 37 °C.....	72
Figure 4.5 Degradation of RR-PVA gel in PBS solution with 10 mM H ₂ O ₂ at 37 °C	72
Figure 4.6 Accumulated release of CDM from RR-PVA gel in the presence of 10 mM H ₂ O ₂	72
Figure 4.7 Fabrication and characterization of the RR-MN array patch. a) An SEM image of the MN array. Scale bar: 200 μm. b) A fluorescence microscopy image showing rhodamine-labeled PVA MN and FITC-labeled HA base. Scale bar: 200 μm. c) A photograph of the MN patch. Scale bar: 1 mm. d) Photos showing the MN patch wrapped on a cotton stick for temporary usage. Scale bar: 10 mm. e) Mechanical strength of one MN	74
Figure 4.8 SEM images of DE showing its porous structure. Scale bars: 10 μm (left), 500 nm (right)	74

Figure 4.9 Oil adsorption test of DE. The upper row presents DE or activated carbon (AC) adsorption of Nile red (NR) containing fatty acids (FA) with different weight ratios. The bottom row shows remained FA/NR under UV light..... 75

Figure 4.10 Adsorption capability of small molecular dye by DE. a) Adsorption of Rhodamine B (RhB) by different amount of DE in aqueous solution. b) Quantitative analysis of remained RhB in figure S7a..... 75

Figure 4.11 Adsorption of RhB by *m*-HA or *m*-HA/DE film with incubation in RhB containing PBS solution at 37°C for 30 min. a) A photo showing the *m*-HA and *m*-HA/DE films after incubation in RhB solution. b) Quantitative analysis of remained RhB in solution after adsorption by the *m*-HA and *m*-HA/DE films 75

Figure 4.12 *In vivo* treatment of acne using different MN array patches. a) Images showing the dramatic decrease in swelling volume of the RR-MN treated back skin of *P. acnes*-induced mice after 6-day treatment. Scale bar: 5mm. b) Comparison of swelling volume size in the back skins of *P. acnes*-induced mice during the treatment period. Statistical significance was calculated by one-way ANOVA, * $P < 0.05$. c) Histological analysis of skin tissues obtained from normal mice, *P. acnes*-induced mice, and *P. acnes*-induced mice treated with CDM cream, RR-MN, blank MN, CDM MN and NR-MN. Scale bar: 200 μm . d) Quantitative analysis of thickness of skin from mice in each group. e) Quantitative analysis of infiltrated inflammation cells in each group. f) Semiquantitative summary of the histological analysis results with a 3-point scale. Error bars indicate s.d. (n = 7) 77

Figure 4.13 <i>In vivo</i> fluorescence whole body imaging showing the release of Cy5.5 from RR-MN, CDM MN and NR-MN in acne area.....	78
Figure 5.1 Schematic of the glucose-responsive insulin delivery system utilizing H ₂ O ₂ and pH cascade-responsive NC-loading MN-array patch. (a) Formation of Ins-NCs and GOx-NCs and mechanism of glucose-responsive insulin release. (b) Schematic of H ₂ O ₂ -triggered charge reduction of the polymer. (c) Schematic of the NC-containing MN-array patch with a CAT sheath structure for <i>in vivo</i> insulin delivery. Insulin release is triggered under a hyperglycemic state	82
Figure 5.2 Synthetic routes of polymers utilized in this study.....	83
Figure 5.3 The ¹ H-NMR spectrum of MPEG _{5K} -P(DMAEMA) _{6K}	84
Figure 5.4 The ¹ H-NMR spectra of MPEG _{5K} -P(DMAEMA-PBA) _{14K} before and after H ₂ O ₂ (80 mM) treatment.....	85
Figure 5.5 The ¹ H-NMR spectrum of poly(DMAEMA) synthesized by ATRP initiated by ethyl α -bromoisobutyrate.....	86
Figure 5.6 The ¹ H-NMR spectrum of poly(DMAEMA-PBA).....	86
Figure 5.7 ¹ H-NMR of PVA methacrylate and its gel in aqueous solution	87
Figure 5.8 The FT-IR spectrum of MPEG _{5K} -P(DMAEMA) _{6K}	93
Figure 5.9 The FT-IR spectrum of MPEG _{5K} -P(DMAEMA-PBA) _{14K}	94
Figure 5.10 The FT-IR spectrum of poly(DMAEMA) synthesized by ATRP initiated by ethyl α -bromoisobutyrate.....	94
Figure 5.11 The FT-IR spectrum of poly(DMAEMA-PBA).....	95
Figure 5.12 Characterizations of Ins-NCs and GOx-NCs. (a) Representative image of Ins-NC solution and hydrodynamic size distribution of Ins-NCs as determined by	

DLS. Inset: A representative picture of the Ins-NC solution sample (insulin concentration: 1 mg/mL). (b) Representative TEM image of Ins-NCs. Scale bar: 100 nm. (c) H₂O₂ generation in PBS (10 mM, pH 7.4) of various glucose (400 mg/dL) as catalyzed by GOx and GOx-NCs. (d) The pH change of PBS solution containing different glucose concentrations (100 or 400 mg/dL) in the presence of GOx-NCs (0.2 mg/mL GOx-eq. concentration). Data points represent mean \pm SD (n=3). Error bars indicate SD 96

Figure 5.13 Representative TEM image and size distribution of Ins-NCs after treatment with PBS containing glucose (400 mg/dL) in the presence of GOx..... 97

Figure 5.14 Representative TEM images and size distribution of GOx-NCs. Scale bar: 50 nm 97

Figure 5.15 *In vitro* characterization of glucose-responsive insulin release. (a) Glucose concentration-dependent insulin release from a complex of insulin in PBS 7.4 in the presence of GOx (0.2 mg/mL). The glucose concentration was set as 0, 100 and 400 mg/dL. (b) H₂O₂ (5 mM) and pH cascade-triggered insulin release from a complex of insulin. (c) Glucose concentration-dependent insulin release from Ins-NCs loaded in *m*-PVA gel in PBS 7.4 in the presence of GOx (0.2 mg/mL). (d) Glucose concentration-dependent GOx release from GOx-NCs encapsulated in *m*-PVA gel in PBS 7.4. Additional GOx (0.2 mg/mL) was added. The glucose concentration was set as 100 and 400 mg/dL. Data points represent mean \pm SD (*n* = 3). Error bars indicate SD 98

Figure 5.16 Insulin release profile from complex formed between insulin and poly(DMAEMA-PBA) in PBS at pH 7.4 in the presence of GOx (0.2 mg/mL) with different glucose concentration (400, 100 and 0 mg/dL)	100
Figure 5.17 Self-regulated insulin release profile as a function of glucose concentration. Data points represent mean \pm SD (n = 3). Error bars indicate SD.....	100
Figure 5.18 Pulsatile insulin release profile as a function of glucose concentrations over time. Data points represent mean \pm SD (n = 3). Error bars indicate SD.....	101
Figure 5.19 CD spectra of native insulin solution and insulin released from the gels incubated with 400 mg/dL glucose	102
Figure 5.20 Representative TEM image of CAT-NG. Scale bar: 20 nm.....	103
Figure 5.21 The H ₂ O ₂ generation rate <i>via</i> glucose oxidation as catalyzed by GOx-NC in the presence of CAT-NG in glucose solution (100 or 400 mg/dL) in PBS with an initial pH at 7.4. The concentration of GOx and CAT was set to 0.2 mg/mL GOx-eq. concentration and 0.08 mg/mL CAT-eq. concentration, respectively. .	103
Figure 5.22 Characterization of the MN array patch with a sheath structure. (a) Representative scanning electron microscopy (SEM) image of microneedle array patch. Scale bar: 600 μ m. (b) Representative fluorescence microscopy image of MN arrays loaded with rhodamine B-labeled insulin. Scale bar: 600 μ m. (c) Representative images of a cross-section of MN with a CAT-NG sheath: rhodamine B labeled insulin (red), FITC labeled CAT sheath layer (green), and merging of both images. The sheath layer was 23 \pm 6 μ m thick as analyzed using software ImageJ. Scale bar: 100 μ m	104
Figure 5.23 The mechanical strength test of microneedle	105

Figure 5.24 Images of a mouse treated by MN (a) and the trypan blue staining (b). Scale bars: 1 cm for (a) and 600 μm for (b) 106

Figure 5.25 Skin puncture marks at 0, 5 and 120 min post-treatment of MNs. Scale bar: 0.5 cm..... 106

Figure 5.26 *In vivo* evaluation of MN array patches for type 1 diabetes treatment. (a) Blood glucose levels of type 1 diabetic mice treated with various kinds of microneedle array patches. (b) Blood insulin level of mice treated with MN array patches. Data points represent mean \pm SD (n = 3). * $P < 0.05$, ** $P < 0.01$ (analyzed by two-tailed Student's t-test) for MN-(G+C+I) compared with control MN-(C+I). (c) Representative images of skins at the treated site of mice. Mice were treated with MN-Gel, MN-(G+I) and MN-(G+C+I) for 12 h, and the skins were gathered after the mice were euthanized. Scale bar: 1 cm. (d) H&E staining and immunohistologic staining with TUNEL assay (green) and Hoechst (blue) of skins treated with MN-(G+C+I). Scale bar: 300 μm . (e) Analysis of blood white cells of mice treated with MN-(G+C+I). Blood samples were obtained 2 d posttreatment. WBC: white blood cells; NEUT: neutrophils; LYMPH: lymphocytes; MONO: monocytes; EO: eosinophils; BASO: basophils..... 107

Figure 5.27 IPGTT and responsiveness. (a) *In vivo* glucose tolerance test toward diabetic mice at one-hour post-treatment of MN-(G+C+I) or subcutaneously injected with insulin. Healthy mice were used as the control. (b) Responsiveness was calculated based on the area under the curve (AUC) in 120 min, with the baseline set at the 0-min blood glucose reading. Data points represent mean \pm

SD (n = 5). $**P < 0.01$ (analyzed by one-way ANOVA) for MN-(G+C+I) compared with control groups 108

Figure 5.28 Hypoglycemic test of MN on healthy mice. (a) Blood glucose levels change of healthy mice treated with MN array patch or subcutaneously injected insulin. The treatment was given at 0 min. (b) Quantification of the hypoglycemia index, identified as the difference between the initial and nadir blood glucose readings divided by the time at which nadir was reached. Data points represent mean \pm SD (n = 5). $**P < 0.01$ (analyzed by two-tailed Student's *t*-test) for MN-(G+C+I) compared with the insulin-treated group 109

Figure 5.29 Cytotoxicity evaluation of the matrix materials utilized in this study toward HeLa cell..... 110

Figure 5.30 H&E staining and immunohistologic staining results of skins treated by blank MN and MN-(G+I). Scale bar: 300 μ m 111

CHAPTER 1 INTRODUCTION

1.1 Introduction

Hypodermic injection is a widely used delivery technique for most biotherapeutics and represents a low-cost and rapid delivery approach.¹ However, injections are often associated with poor patient adherence and may lead to injection phobia and distress.²⁻⁵ An attractive alternative to hypodermic injection is to deliver therapeutics across the skin using transcutaneous patches.^{2-3, 6} Typically, these transcutaneous patches incorporate arrays of microneedles (MNs) that are designed to penetrate skin's outer stratum corneum layer to enhance delivery capabilities.^{2, 7-9} Since the needles are micron-size, they can deliver almost any drug or small particulate formulation as well as facilitate localized tissue delivery.² Critically, transcutaneous patches are a more appealing approach to patients as this method of drug delivery is painless and can be self-administered.^{2-3, 6}

Recently, transdermal patch models that incorporate stimuli-responsive MNs which release drug in response to an internally-generated stimuli have been proposed for smart and precise drug release.¹⁰⁻¹³ Compared to delivery systems triggered by external stimuli like electric field,¹⁴⁻¹⁵ light,¹⁶⁻¹⁷ or mechanical force,¹⁸ the MN patches activated by a physiological signal provide self-regulated delivery of drug in response to the abnormal physiological signals, thereby maximizing therapeutic efficiency and minimizing side effects or toxicity.¹⁹

For instance, glucose-responsive MNs can be triggered to release insulin in response to abnormally high glucose levels in vascular and lymph capillary networks while showing basal insulin release in euglycemic conditions, achieving a smart closed-loop system for insulin

delivery.²⁰ Herein, we will summarize and classify recent advances in the development of bioresponsive transcutaneous patches, including pH-responsive, glucose-responsive, and enzyme-activated systems (Figure 1.1), and discuss the advantages, limitations of these current formulations. Future challenges and opportunities in terms of clinical translation will also be discussed.

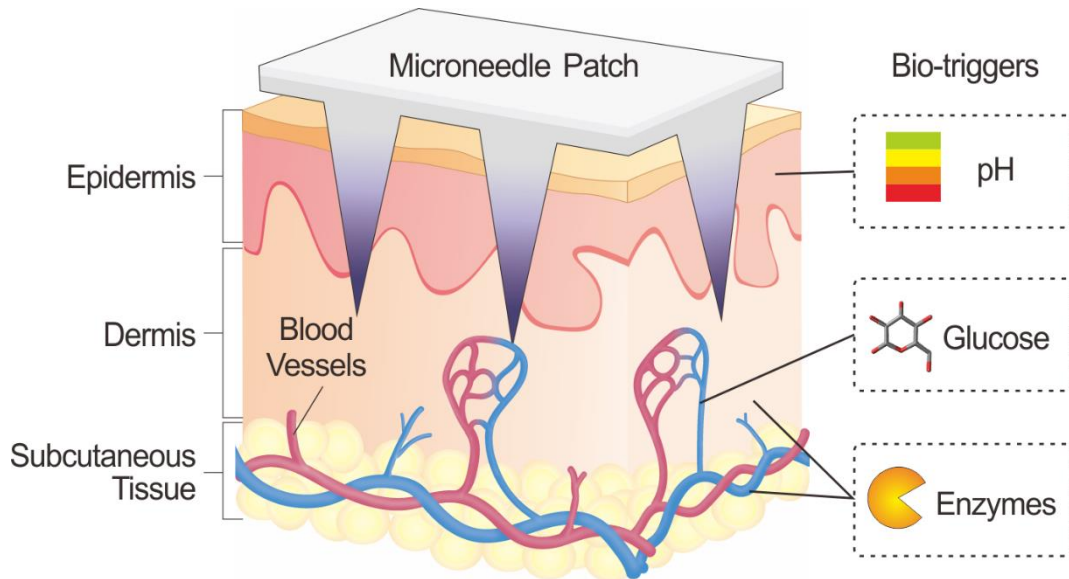


Figure 1.1 Typical physiological signals (bio-triggers) for bioresponsive transcutaneous patches.

1.2 pH-Responsive Transdermal Patches

Normal skin is slightly acidic, with a pH ranging from 4.0-7.0, which provides a barrier to bacteria, viruses and other potential contaminants.²¹ In particular, the acid mantle secreted by sebaceous glands maintains the epidermis pH at approximately 5.5.²² The acidic properties of skin enable the use of pH-sensitive patches for on-demand transdermal drug delivery. For example, MNs filled pH-responsive poly(lactic-co-glycolic acid) (PLGA) hollow microspheres were developed and reported to sequentially co-deliver multiple drugs to skin tissue by Ke *et al.*²³ In this system, hollow PLGA microspheres encapsulated an aqueous core

containing red-fluorescent dye Cy5 as a model drug and sodium bicarbonate (NaHCO_3) loaded *via* a double-emulsion method. The Cy5-loaded microspheres and a second model drug, Alexa 488, were further encapsulated together in polyvinylpyrrolidone (PVP) MN arrays. Upon application to the skin, the PVP rapidly dissolved within minutes, simultaneously releasing the Alexa 488 dye. The acidic environment of the skin stimulated NaHCO_3 in the PLGA microspheres to generate CO_2 bubbles, thereby creating the channels in the PLGA shell and releasing the Cy5. Researchers demonstrated the sequential release of the two dyes into the porcine cadaver skin *ex vivo* using fluorescence microscopy. pH-sensitive surface modification was also reported in the fabrication of pH-sensitive microneedles. Here, MNs were coated with ovalbumin, a model antigen, and a pH-sensitive pyridine surface.²⁴ Upon insertion into the acidic skin conditions, reduced electrostatic interactions allowed the ovalbumin to be efficiently released. Layer-by-layer assembly of polyelectrolytes has also been shown to achieve pH-triggered drug release through weakened electrostatic binding that occurs between the negatively and positively charged layers in the physiological pH.²⁵⁻²⁶

1.3 Glucose-Responsive Transdermal Patches

Since MNs inserted into skin can directly contact the dermal microcirculation, these MNs can sense serum biomarker levels and changes thereof in a real-time manner.^{8, 27} For patients with diabetes who are tasked with frequent monitoring of blood glucose levels and timely injection of insulin as part of diabetes self-management,²⁸⁻²⁹ insulin-loaded MNs with glucose-responsive moieties are desirable for achieving closed-loop insulin delivery. Based on this concept, Yu *et al.* have developed a “smart insulin patch” that effectively releases insulin in response to hyperglycemic conditions for diabetes treatment.²⁰ In this study, glucose-

responsive vesicles containing insulin and the glucose-specific enzyme (GOx) were loaded into the tips of MN arrays. These vesicles were formed from hypoxia-sensitive hyaluronic acid (HA) conjugated with a hydrophobic group that could be bio-reduced to hydrophilic under hypoxic conditions (2-nitroimidazole). In hyperglycemic conditions, oxygen consumption from the enzymatic conversion of glucose to gluconic acid generated a local hypoxic environment, which resulted in the reduction of 2-nitroimidazole to hydrophilic 2-aminoimidazole, disassembly of the vesicles, and subsequent insulin release. Researchers demonstrated this glucose-responsive insulin-delivery system was able to quickly “sense” and correct elevated blood glucose levels of chemically induced type 1 diabetic mice to the normal state within 0.5 h and maintain euglycemic conditions for several hours thereafter.

Furthermore, Gu group have also designed an MN patch integrated with insulin-secreting pancreatic *beta*-cells and loaded with glucose-signal amplifiers for glucose-responsive insulin delivery.³⁰ Instead of direct insulin release from glucose-responsive vesicles, these vesicles were encapsulated with GOx, α -amylase as well as glucoamylase and acted as synthetic glucose-signal amplifiers. In high glucose concentrations, α -amylase and glucoamylase were released and hydrolyzed the α -amylose that loaded in MNs into glucose. This amplified glucose signal further diffused into the externally positioned *beta*-cell capsules on the base of MN patch, prompting secretion of insulin for diffusion into the vascular and lymph capillary networks. This model showed extended therapeutic efficacy compared the MNs without glucose-signal amplifiers, where one patch was shown to effective control on blood glucose levels for 6 h in diabetic mouse.

Besides enzymatically-generated hypoxia, H_2O_2 produced during the enzymatic oxidation of glucose can also act as a trigger to facilitate insulin release from MNs. Hu *et al.* described a glucose-responsive insulin delivery device integrating H_2O_2 -sensitive polymeric vesicles with an MNs-array patch.³¹ The insulin-loaded polymeric vesicles (PVs) were self-assembled from block copolymers incorporated with polyethylene glycol (PEG) and phenylboronic ester (PBE)-conjugated polyserine. In this system, the PBE pendant were degraded in a H_2O_2 -mediated manner, leading to the disassociation of PVs. *In vivo* performance of the patch integrating with these PVs demonstrated the ability to correct hyperglycemia and self-regulate blood glucose levels in a diabetic mouse model.

Most recently, Gu group have integrated hypoxia and H_2O_2 dual-sensitive vesicles to design MNs for enhanced glucose-responsive insulin delivery.³² These dual-sensitive vesicles were prepared by diblock copolymer consisting of poly(ethylene glycol) (PEG) and polyserine modified with 2-nitroimidazole *via* a thioether moiety. Hydrophobic 2-nitroimidazole could be bio-reduced into hydrophilic 2-aminoimidazole under a hypoxic condition. In addition, the thioether acted as a H_2O_2 -sensitive moiety that increased the aqueous solubility of the copolymer upon conversion to a sulfone by H_2O_2 . When these vesicles encapsulating insulin and GOx were exposed to a high blood glucose level in the vascular and lymph capillaries, the quick oxygen consumption and H_2O_2 generation led to the increased water-solubility of copolymer, promoting the dissociation of the glucose-responsive vesicles and subsequent release of the insulin. Importantly, the undesirable H_2O_2 was eliminated during the conversion of thioether to sulfone, thereby mitigating free radical-induced damage to skin tissue and maintaining the activity of the GOx. Researchers demonstrated this integrated smart insulin

patch could effectively regulate blood glucose levels in diabetic mice for 10 h and was associated with insignificant inflammation during a longer two-week period of usage.

Aside from the use of hyperglycemia as a disease-associated trigger for the release of therapeutics such as insulin, normal blood glucose level can also be used as a physiological signal to achieve sustained drug release. For instance, Wang *et al.* reported an anti-PD-1 loaded MN patch for sustained drug delivery in a glucose-mediated degradation manner for the melanoma treatment.³³ The checkpoint inhibitor (anti-PD-1) that blocks the programmed death-1 (PD-1) pathway was encapsulated in glucose-responsive nanoparticles. With the GOx/Catalase enzymatic system immobilized inside the NPs, gluconic acid generated from the enzymatic oxidation of glucose facilitated the gradual self-dissociation of NPs, creating a sustained release of anti-PD-1 over a three-day administration period. *In vivo* studies demonstrated robust immune responses in a B16F10 mouse melanoma model treated with the aPD1 patches compared to control groups administrated with patches that cannot be triggered to degrade or intratumoral injection of free aPD1 with the same dose.

1.4 Enzymes-Activated Transdermal Patches

Disease-associated enzymes have recently attracted remarkable attention as targets for precision medications.³⁴⁻³⁵ For example, hyaluronidase (HAase) is overexpressed by various types of cancer cells and has become recognized as a tumor marker.³⁶ Recently, a HAase-activated drug delivery system was developed for synergistic transcutaneous immunotherapy to enhance antitumor immune responses.³⁷ In this study, 1-methyl-DL-tryptophan (1-MT), an inhibitor of immunosuppressive enzyme indoleamine 2,3-dioxygenase (IDO), was conjugated

to hyaluronic acid (HA) to give an amphiphilic polymer that was self-assembled into therapeutic nanocapsule to encapsulate anti-PD1 antibody (aPD1), the inhibitor of the immunoinhibitory receptor programmed cell death protein 1 (PD1). Integrated with the MN arrays, this combination of therapeutics was shown to be readily transported across the stratum corneum and successfully reach the network of skin-resident dendritic cells (DCs) around the melanoma tumor. Drug release was facilitated by the high levels of HAase overexpressed in the tumor region, which activated by the enzymatic degradation of HA. This system exhibited enhanced local retention of the therapeutics and a potent antitumor effect in a B16F10 mouse melanoma model.

In another study, in order to achieve long-term auto-regulation of blood coagulation, Zhang *et al.* designed a thrombin-responsive patch for on-demand heparin delivery.³⁸ Heparin, a common anticoagulant, was conjugated to the main chain of hyaluronic acid through a thrombin-cleavage peptide (GGLVPR|GSGGC) to create a closed-loop device for sustained anticoagulant regulation. The MNs prepared from the heparin-HA conjugate were shown to quickly respond to an increased thrombin levels by releasing heparin, preventing the undesirable formation of blood clots by the thrombin-triggered cleavage of the linker. Under normal blood conditions, no drug was released. Subsequent *in vivo* thrombolytic challenge experiments revealed potential for this patch as an efficient, long-term protection against abnormal blood clotting and acute pulmonary thromboembolism.

1.5 Conclusions and Outlook

Bioresponsive transcutaneous patches hold tremendous promise for on-demand drug delivery to enhance therapy efficacy while minimizing associated toxicity or side effects. In Table 1.1, we summarize typical responsive mechanisms triggered by a variety of the physiological stimuli described in this chapter, including changes in pH, serum glucose levels, and enzyme activity. Looking ahead, physiological signal-responsive devices may be highly desirable for the precision treatment of diseases that are associated with metabolic levels.³⁹

Despite remarkable achievements in this area, the field of bioresponsive transdermal delivery is still in its infancy, and the investigation of these systems remains centered in *in vivo* preclinical models or early clinical trials. How to achieve sufficient biocompatibility and complete safety is a critical issue to be solved in future research that is focused on translation from the bench to clinical use.⁴⁰⁻⁴² This work requires a closer investigation of the response rate of the patches, detailed characterization of the relevant physiological gradients required to achieve smart and precise release of cargoes, and thorough evaluation of the local and systemic side effect of such transcutaneous patches. In addition, most *in vivo* experiments use rodent animal models, and the potential for translation to human studies could be limited by the loading capacity of general patches. It is essential that the next-generation of transcutaneous devices are developed with sufficient loading capacity to match the long-term dosage of the specific therapeutics.

Table 1.1 Summary of recently developed bioresponsive transcutaneous patches.

Stimulus	Materials	Model therapeutics	Ref
pH	PVP, pH-sensitive PLGA nanoparticles	Alexa488 and Cy5	23
	Pyridine modified silicon, <i>N</i> -trimethyl chitosan	Ovalbumin	24, 26
	Metal, polydopamine, heparin, and albumin	DNA	25
Glucose	HA, hypoxia-sensitive vesicles	Insulin	20, 30
	HA, H ₂ O ₂ -sensitive polymersomes	Insulin	31
	HA, hypoxia and H ₂ O ₂ dual-sensitive polymersomes	Insulin	32
	HA, pH-sensitive dextran nanoparticles	anti-PD-1	33
Enzyme	1-MT conjugated HA	1-MT and anti-PD-1	37
	Heparin conjugated HA	Heparin	38

1.6 Dissertation Scope and Organization

The aim of this dissertation is to develop bioresponsive drug delivery systems based on transcutaneous patches of arrayed microneedles for therapeutic applications. This dissertation is presented as four separate manuscripts (Chapter 2-5) with a comprehensive introduction (Chapter 1) highlighting recent advances in the development and application of bioresponsive microneedle patches for transdermal drug delivery in an on-demand manner. A summary that concludes the primary findings described in Chapter 2 to 5 is also provided.

Chapter 2 reports a thrombin-responsive microneedle patch for closed-loop heparin delivery to achieve long-term prevention of coagulation. In Chapter 3, we describe a glucose-triggered

microneedle patch to locally induce adipose tissue browning for obesity treatment. Chapter 4 reports an inflammatory signal-activated patch to deliver antibiotic into dermis for enhanced acne treatment. Chapter 5 describes a glucose-responsive microneedle patch comprised of pH and H₂O₂-sensitive nanocomplexes for self-regulated insulin delivery to manage diabetes. Finally, conclusions were given in Chapter 6 with further discussion, implications of previous results, and insights in developing bioresponsive drug delivery systems based on microneedle patches for therapeutic applications.

CHAPTER 2 THROMBIN-RESPONSIVE TRANSCUTANEOUS PATCH FOR AUTO-ANTICOAGULANT REGULATION

2.1 Introduction

Thrombosis, a pathological hemostatic condition, has become one of the leading causes of cardiovascular mortalities and morbidities worldwide.⁴³⁻⁴⁴ The unwanted intravascular blood thrombi can cause vascular occlusions, organ damage, and severe cardiovascular diseases, including myocardial infarction and stroke.⁴⁵⁻⁴⁷ As a first line of defense, anticoagulant drugs can prevent and delay the obstruction in blood flow.^{44, 48} Heparin (HP), a common anticoagulant, is routinely administered to counteract coagulation activation.⁴⁹⁻⁵⁰ Dosing schemes for HP usually involve daily intravenous administration for weeks to months.⁵¹ Unfortunately, systemic (intravenous) or local (catheter) delivery of anticoagulants remains difficult for precise anticoagulant regulation.⁵² Under- or over-dosage may lead to dangerous consequences due to either rapid clearance in the body or bleeding complications that may lead to spontaneous hemorrhages.⁵³ Moreover, it is known that the timely delivery of drugs is critical for cardiovascular patients when an unpredictable attack happens,⁵⁴ which makes sustained protection from pathogenesis imperative. Therefore, a controlled and on-demand drug delivery system, one that enhances therapeutic efficacy while minimizing side effects and time-to-treatment, is urgently needed for the management of thrombotic diseases.⁵⁵⁻⁵⁷

Herein, we report an engineered feedback-controlled anticoagulant system based on thrombin-responsive polymer-drug conjugates. Thrombin is a trypsin-like serine proteinase that plays an imperative role in blood coagulation systems to produce insoluble fibrin from soluble fibrinogen.⁵⁸ Recently, thrombin-responsive systems based on the thrombin-cleavable peptide

have attracted great attention due to associated high sensitivity and fast response rate.⁵⁹⁻⁶⁰ In our system, a thrombin-cleavable peptide is introduced as a linker during the conjugation of HP to the main chain of hyaluronic acid (HA).⁶¹ The peptide can be cleaved when thrombin is activated,⁶²⁻⁶³ triggering the release of drug from the backbone in a thrombin-responsive fashion (Figure 2.1a). The thrombin-responsive HP conjugated HA (TR-HAHP) matrix can be obtained *via* polymerization under ultraviolet (UV) light treatment. In the presence of the elevated thrombin concentration, HP can be promptly released from the TR-HAHP matrix, whereas HP is trapped in the matrix and cannot be released without thrombin. The released HP is able to inhibit the coagulation activation by inactivating thrombin, which suppresses the release of HP from the matrix and minimizes the risk of undesirable spontaneous hemorrhage.

The TR-HAHP derivative can be further integrated into a disposable microneedle (MN)-array based transcutaneous device for potential long-term autoregulation of blood coagulation. The micro-size needles on the patch enable convenient administration in a painless manner.^{1, 20, 64-66} Owing to the thrombin-responsive property, this MN patch acts as a closed-loop “smart” device that can be safely inserted in the skin without drug leaking under normal blood environment, but rapidly responds to an increased thrombin level and releases a corresponding dose of anticoagulant drug to prevent the undesired formation of blood clots (Figure 2.1b). We demonstrate that this “smart” HP patch can offer sustained autoregulation of blood coagulation in a safe and convenient manner.

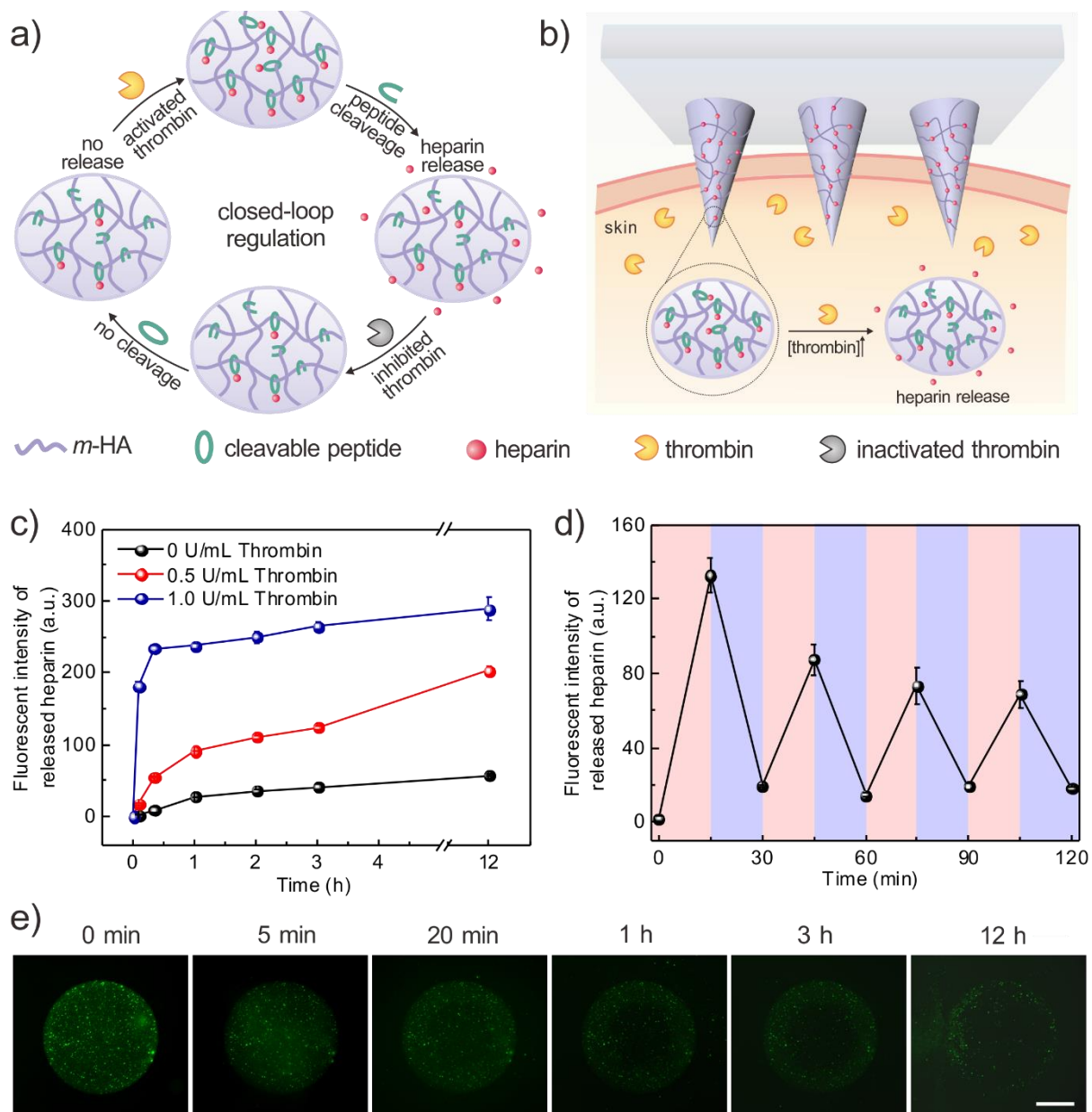


Figure 2.1 (a) Formation and mechanism of the feedback-controlled heparin delivery system based on thrombin-responsive HAHP (TR-HAHP) conjugate. (b) Schematic of the TR-HAHP MN array patch in response to thrombin. (c) *In vitro* accumulated FITC-labeled HP release from the TR-HAHP hydrogel in several thrombin concentrations at 37 °C. (d) Pulsatile release profile of FITC-HP from the TR-HAHP hydrogel (blue: w/o thrombin; pink: w/thrombin). (e) Fluorescence microscopy images of the TR-HAHP hydrogel in thrombin solution at indicated time points. Scale bar: 1 mm. Error bars indicate s.d. (n = 3).

2.2 Experimental Section

2.2.1 Materials

All chemicals were purchased from Sigma-Aldrich unless otherwise specified and were used as received. Thrombin cleavable peptide (GGLVPRGSGGC) was ordered from GL Biochem Ltd (Shanghai, China). Heparin with an activity of 212 U/mg was obtained from Sigma-Aldrich. aPTT, PT, TCT reagents and human plasma were purchased from Helena Laboratories, Inc (Beaumont, TA, USA). Human F1+2 ELISA kit was purchased from MyBioSource, Inc (San Diego, CA, USA). The deionized water was prepared by a Millipore NanoPure purification system (resistivity higher than 18.2 M Ω cm⁻¹).

2.2.2 LC-MS analysis of peptide cleavage

Peptide with sequence GGLVPR|GSGGC was incubated with thrombin (1 U/mL) in Tris buffer (20 mM Tris, 150 mM NaCl, 2.5mM KCl, pH 7.4) for 12 h. The LC-MS analysis of intact peptide and cleaved peptide (GGLVPR) was shown in Figure 2.2.

2.2.3 Synthesis of acrylate modified HA (*m*-HA)

m-HA was synthesized follow the previously reported method.⁶⁷ Briefly, 2.0 g of HA was dissolved in 100 mL of DI water at 4 °C, to which 1.6 mL of methacrylic anhydride (MA) was dropwise added. The reaction solution was adjusted to pH 8-9 by the addition of 5 M NaOH and stir at 4 °C for 24 h. The resulting polymer was obtained by precipitation in acetone, followed by washing with ethanol for 3 times. The product re-dissolved in DI water and the solution dialyzed against DI water for 2 days. *m*-HA was achieved by lyophilization with a yield of 87.5%. The degree of modification was calculated to be 15% by comparing the ratio

of the areas under the proton peaks at 5.74 and 6.17 ppm (methacrylate protons) to the peak at 1.99 ppm (*N*-acetyl glucosamine of HA) after performing a standard deconvolution algorithm to separate closely spaced peaks. ^1H NMR (300 MHz, D_2O , δ): 1.85-1.96 (m, 3H, $\text{CH}_2=\text{C}(\text{CH}_3)\text{CO}$), 1.99 (s, 3H, NHCOCH_3), 5.74 (s, 1H, $\text{CH}^1\text{H}^2=\text{C}(\text{CH}_3)\text{CO}$), 6.17 (s, 1H, $\text{CH}^1\text{H}^2=\text{C}(\text{CH}_3)\text{CO}$).

2.2.4 Synthesis of HA-Pep conjugates

50 mg of *m*-HA was mixed with 1-ethyl-3(3-dimethylaminopropyl) carbodiimide (EDC)/*N*-hydroxysuccinimide (NHS) (117 mg/81 mg) for the activation of carbonyl groups on *m*-HA in a pH 5.0 sodium acetic buffer for 30 min at RT, and the unreacted EDC and NHS were removed using a centrifugal filter (100, 000 Da MWCO, Millipore). Then 30 mg peptide was added to react with *m*-HA in a pH 7.4 PBS buffer at RT for overnight. Free peptides were removed using a centrifugal filter (100, 000 Da MWCO).

2.2.5 Synthesis of TR-HAHP conjugates

The carbonyl groups on HP was activated by mixing with EDC/NHS and stirred for 30 min. Then 1,6-diaminohexane was added for another 4 h at RT (pH 8.5). The reaction solution was thoroughly dialyzed against DI water for 1 day and followed by lyophilization (Freeze Dry System, Labconco, Kansas City, MO, USA) to remove the residual water. The pre-modified HP was mixed with sulfosuccinimidyl-4-(*N*-maleimidomethyl)- cyclohexane-1-carboxylate (Sulfo-SMCC, Pierce) in PBS (pH 7.4) at a molar ratio of 1:5 for 0.5 h at RT and purified with a centrifugal filter (10, 000 Da MWCO). Finally, the activated HP and the HA-Pep conjugates were mixed in PBS (pH 8.0). After 24-h reaction at 4 °C, the obtained TR-HAHP was washed

with water using a centrifugal filter (100, 000 Da MWCO) and stored at 4 °C till use. The elemental analysis of TR-HAHP was measured using a FEI Verios 460L field-emission scanning electron microscope (FESEM) combined with energy dispersive X-ray microanalysis. Fluorescein isothiocyanate (FITC) labelled HP was obtained by mix the FITC with HP for 24 h at RT. The free FITC were removed by a centrifugal filter (10, 000 Da MWCO).

2.2.6 Synthesis of NR-HAHP conjugates

The NR-HAHP conjugates was prepared by directly mix carbonyl group-activated *m*-HA with the HP derivative in PBS buffer (pH 7.4) for overnight reaction. Free HP was removed by ultracentrifugation as mention above.

2.2.7 Preparation of TR-HAHP hydrogel

Cross-linker *N,N'*-methylenebisacrylamide (MBA, w/v: 2%) and photoinitiator (Irgacure 2959, w/v: 0.2%) were mixed in TR-HAHP solution. After UV irradiation (wavelength: 365 nm) for 60 s, the mixture underwent the crosslinking polymerization to form the hydrogel.

2.2.8 *In vitro* release studies

To evaluate the thrombin-responsive characteristics of TR-HAHP hydrogels, the hydrogels were incubated in Tris buffer (20 mM Tris, 150 mM NaCl, 2.5mM KCl, pH 7.4) at 37 °C on an orbital shaker, to which various amounts of thrombin were added to reach concentrations at 0, 0.5, and 1 U/mL. At predetermined time points, 100 μ L of the supernatant was taken out for analysis by measuring the emission intensity of FITC at 519 nm with the excitation wavelength at 495 nm on the Infinite 200 PRO multimode plate reader (Tecan Group Ltd., Switzerland).

To access the hydrogel's ability to adapt to cyclical changes in thrombin concentrations, the TR-HAHP hydrogel was first incubated in Tris buffer with thrombin (0.6 U/mL) for 15 min. At that point, the supernatant was removed and the FITC intensity was measured using the same method mentioned above. Then the hydrogel was incubated in Tris buffer without thrombin for another 15 min. This cycle was repeated numerous times.

The release profiles of FITC-heparin from MNs were monitored by immersing the tips of MNs into Tris buffer with different concentrations of thrombin. At predetermined time points, 100 μ L of the medium was taken out, and the fluorescence intensity was then measured using the same method mentioned above to quantify the release amount of FITC-heparin.

2.2.9 Anticoagulant assays

In vitro Activated Partial Thromboplastin Time (aPTT) assay and Prothrombin Time (PT) assay were performed to examine the anticoagulant activity of TR-HAHP. Specifically, the hydrogel (HA, HP, NR-HAHP, TR-HAHP), human plasma, and aPTT or PT reagent were mixed together at a ratio of 1:9:10 and incubated at 37 °C for 3 min. Then, 0.025 μ M calcium chloride was added to the samples, and the time was recorded for clot formation. For the Thrombin Clotting Time (TCT) assay, the human plasma was first incubated with hydrogel for 3 min at 37 °C. Afterwards, the TCT reagent was added into the mixture and the clotting time was recorded. The hydrogels with and without crosslink were tested separately for each assay. To evaluate the thrombin responsiveness of TR-HAHP, the hydrogels were incubated with human plasma for two cycles. Each cycle was performed at 37 °C under constant revolution and avoiding air contact for 3 h. The blood plasma was removed after the first incubation and

replaced with fresh human plasma. After each incubation period, ELISA tests using commercial kits for prothrombin F1+2 fragment was performed.

2.2.10 Fabrication of TR-HAHP MNs

All the MNs in this study were fabricated using the uniform silicone molds from Blueacre Technology Ltd. Each needle had a 300 μm by 300 μm round base tapering to a height of 600 μm with a tip diameter of around 10 μm . The needles were arranged in a 20 \times 20 array with 600 μm tip-to-tip spacing. To fabricate TR-HAHP MN, TR-HAHP solution with MBA (w/v=2%), photoinitiator (Irgacure 2959, w/v=0.5%) was first deposited by pipet onto the MN mold surface (100 μL /array). Then, molds were placed under vacuum (600 mmHg) for 20 min to allow the solution filled the MN cavities and became more viscose. Afterwards, the covered molds were centrifuged using a Hettich Universal 32R centrifuge for 20 min at 2000 rpm. Finally, 3 mL premixed *N,N'*-methylenebisacrylamide (MBA, w/v: 2%), photoinitiator (Irgacure 2959, w/v: 0.5%) and *m*-HA solution(w/v: 4%) was added into the prepared micromold reservoir and allowed to dry at 20 $^{\circ}\text{C}$ under vacuum desiccator. After completely desiccation, the MN patch was carefully detached from the silicone mold and underwent the crosslinking polymerization *via* UV irradiation (wavelength: 365 nm at an intensity of 9 mW/cm^2) for 30 s. The resulting MN-array patches were stored in a sealed six well container for later study. The morphology of the MNs was characterized *via* a FEI Verios 460L field-emission scanning electron microscope.

2.2.11 Mechanical strength test

The mechanical strength of MNs was measured by pressing MNs against a stainless steel plate. The speed of the top stainless steel plate movement towards the MN-array patch was 1 $\mu\text{m/s}$. The fracture force of MNs was recorded as the needle began to buckle.

2.2.12 Skin penetration efficiency test

The MN-array was applied to the back of the mouse skin for 30min. After euthanized by CO₂ asphyxiation, the skin was excised and stained with trypan blue for 30 min for imaging by optical microscopy (Leica EZ4 D stereo microscope).

2.2.13 Biocompatibility analysis

To evaluate the biocompatibility of the MN-array patches, mice were euthanized by CO₂ asphyxiation and the surrounding tissues were excised after 24-hour MN administration. The tissues were fixed in 10% formalin for 18 h and then embedded in paraffin, cut into 50 μm sections, and stained using hematoxylin and eosin (H&E) and fluorescent TUNEL staining for histological analysis.

2.2.14 *In vivo* thrombosis model

Pulmonary thromboembolism in mice was induced follow the literature.⁶⁸⁻⁶⁹ Briefly, female CD-1 mice (Charles Rives, Raleigh, NC, USA), weighing 20-25 g were used. The animal study protocol was approved by the Institutional Animal Care and Use Committee at North Carolina State University and University of North Carolina at Chapel Hill. Mice were caged and fed a regular diet for at least one week before use. Eight mice for each group were selected and pre-

administered with the drugs (HA MN, HAHP MN, NR-HAHP MN, TR-HAHP MN) for tests (HP dose: 5 U/patch). The thrombotic challenge was induced by the rapid *i.v.* injection of 0.2 mL of bovine thrombin solution (1000 U/kg) into the mouse tail vein. The cumulative end point to be overcome was the immediate death of the animal or prolonged paralysis of the hind limbs (for more than 15 min). The total duration of each experiment was 15 min. The animals which did not die within this time were sacrificed by exposure to CO₂ and will be recorded as survivors. No anesthesia was used during the experiment because of the short duration and because anesthesia has been reported to interfere with thromboembolism in this model.⁷⁰ After sacrifice, the lungs of mice were collected, fixed, and sectioned for H&E staining and observed by optical microscopy.

2.2.15 Tail bleeding test

For safety test of the TR-HAHP MN *in vivo*, 5 mice (male C57B6, Jackson Lab, U.S.A.) in each group were pretreated with different MN patches (with a dose of 200 U/kg HP) and then placed on a 37 °C heating pad. About 2–4 mm from the tip of the mouse's tail (in about 1 mm diameter), a cut was made with a disposable surgical blade. After transection, the tail was immediately placed in a 50-ml falcon tube filled with 37 °C saline. The bleeding time was recorded up to 30 min, red blood cells were counted in each collected blood sample.

2.2.16 Statistical analysis

All results presented are Mean \pm SD. Statistical analysis was performed using Student's *t-test* or ANOVA test. With a *P* value < 0.05, the differences between experimental groups and control groups were considered statistically significant.

2.3 Results and Discussion

2.3.1 Preparation and characterization of thrombin-responsive heparin hydrogel

To achieve the stimuli-triggered heparin delivery, a thrombin cleavable peptide with a sequence of GGLVPR|GSGGC, was introduced as a linker to obtain the TR-HAHP. The cleavage of the peptide by thrombin was verified by liquid chromatography mass spectrometry (LCMS) analysis, which showed that the peptides were efficiently cleaved after 12-h incubation with 1 U/mL thrombin in Tris buffer (20 mM Tris, 150 mM NaCl, 2.5mM KCl, pH 7.4) (Figure 2.2). To prepare the TR-HAHP, the cleavable peptide was first conjugated to the methacrylated HA (*m*-HA) through the formation of an amide bond. Then, HP was further covalently bound to the cysteine residue of the peptide to obtain the TR-HAHP. In the presence of the activated thrombin, the short peptide can be selectively recognized and cleaved between Arg (R) and Gly (G) to achieve specific HP release.⁶² The successful conjugation of HP to *m*-HA was evidenced by the elemental analysis and the increase in molecular weight from 314 to 606 kDa (Table 2.1).

Table 2.1 Elemental analysis of *m*-HA, HP and TR-HAHP.

Percent (%)	C	O	N	S
<i>m</i> -HA	45.8±0.5	35.3±0.4	3.8±0.5	0.7±0.2
HP	26.2±0.4	39.1±0.5	1.4±0.4	17.1±0.5
TR-HAHP	49.7±0.5	27.5±0.4	7.8±0.5	8.6±0.4

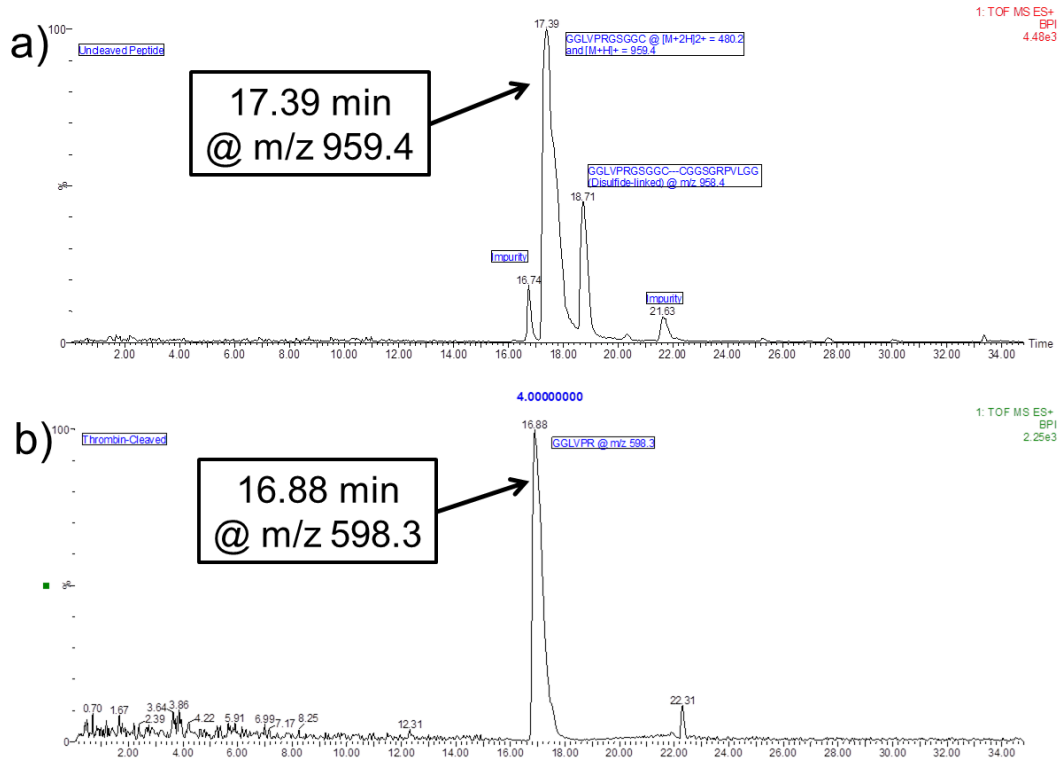


Figure 2.2 LCMS spectra of peptide (a) before and (b) after thrombin cleavage.

In order to examine the effect of thrombin in the TR-HAHP based system, a TR-HAHP hydrogel was prepared *via* photo-polymerization (Figure 2.3). The prepared hydrogels were incubated in thrombin solutions with different concentrations (0, 0.5 and 1 U mL), and the release kinetics were obtained by measuring the fluorescence intensity of FITC-labeled HP. As shown in Figure 2.1c, the release profiles presented a high dependence on the thrombin level. The TR-HAHP hydrogel quickly responded to the relative higher thrombin concentration (1 U/mL), and released most of the conjugated HP within 20 min, allowing for a fast action of the drug under urgent clinical situations. In contrast, the hydrogel was stable in the buffer without thrombin for up to 12 h (Figure 2.1c and 2.4). Furthermore, a pulsatile release pattern was observed when the TR-HAHP hydrogel was alternately exposed every 15 min for several cycles to solutions with and without thrombin (Figure 2.1d). The hydrogel performed the

repeatable and sustained release of HP, corresponding to the presence or absence of thrombin. Additionally, the release process was monitored in real time by fluorescence microscopy. As demonstrated in Figure 2.1e, the cleaved FITC-HP gradually diffused through the cross-linked hydrogel after the addition of thrombin, while the hydrogel maintained its original structure during the release period. In contrast, there was insignificant fluorescence signal detected in the buffer without thrombin after 12 h (Figure 2.4). To further confirm the thrombin-responsive release, a non-responsive HP-HA conjugate without the thrombin-sensitive peptide (NR-HAHP) was synthesized directly *via* a heterobifunctional linker as a negative control. From the fluorescence images and release profiles of the NR-HAHP hydrogel incubating with thrombin solutions, it was demonstrated that HP could not detach from the HA matrix without the degradation of the thrombin-sensitive peptide (Figure 2.4 and 2.5). Collectively, these results suggested that the thrombin-specific activation feature of the TR-HAHP is attributed to the incorporation of the cleavable peptide unit.

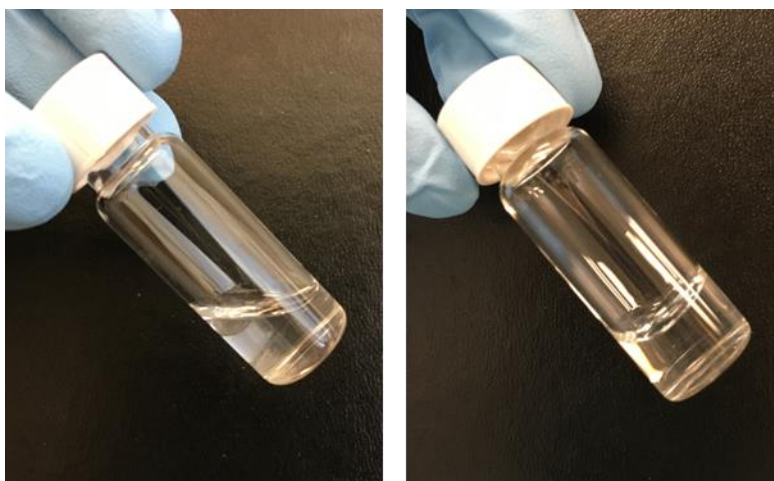


Figure 2.3 Photographies of TR-HAHP gel before (left) and after (right) UV irradiation.

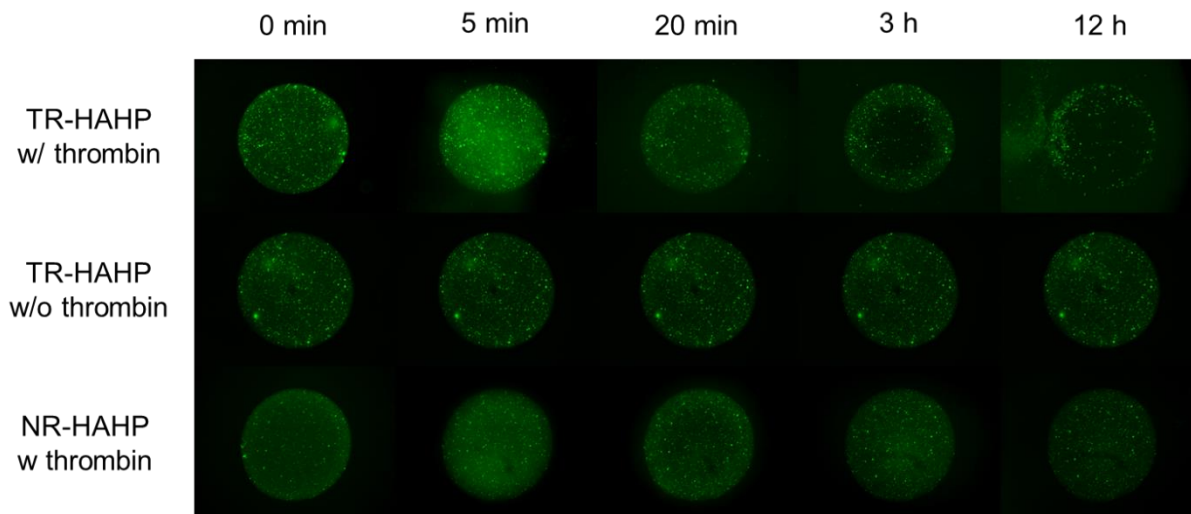


Figure 2.4 Fluorescence microscopy images of the TR-HAHP and NR-HAHP hydrogels in thrombin solutions at indicated time points.

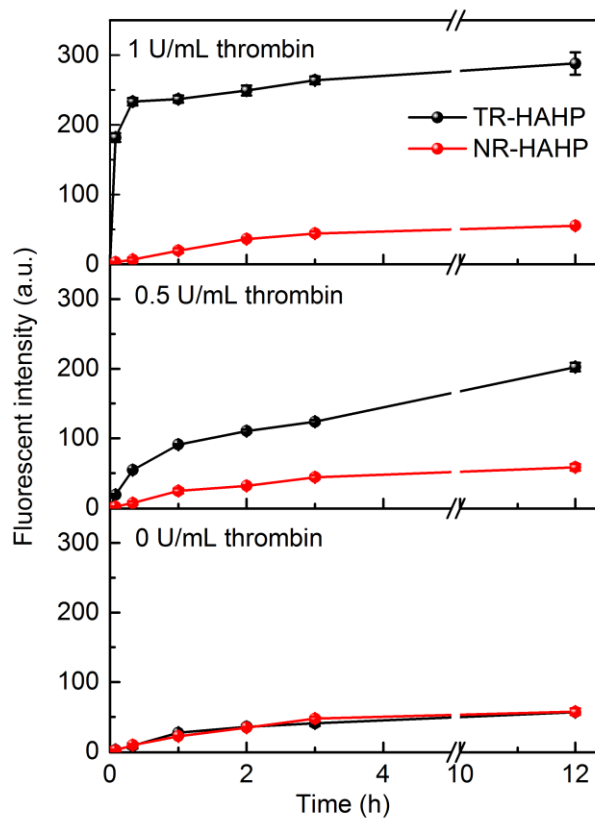


Figure 2.5 Release profiles of HP from TR-HAHP and NR-HAHP hydrogels in different concentrations thrombin solutions respectively. Error bars indicate s.d. (n=3).

2.3.2 *In vitro* anticoagulant regulation evaluation

To validate the *in vitro* anticoagulant regulation ability of TR-HAHP, the activated thromboplastin time (aPTT) and prothrombin time (PT) were measured to determine the anticoagulant potency of different samples, including the empty HA hydrogel, HA hydrogel containing free HP, TR-HAHP gel, and NR-HAHP gel by incubation with human plasma. The activated thromboplastin time measurement is commonly used for the evaluation of the intrinsic pathways of blood coagulation,⁷¹⁻⁷² while the PT measurement is a test for the evaluation of extrinsic pathways in clinical medicine.⁷³ Antithrombin III, a natural thrombin inhibitor, can inactivate thrombin *via* forming a covalent enzyme complex with thrombin.⁷⁴⁻⁷⁵ Since it has a specific heparin binding-site proximal to the pentasaccharide, the inactivation of thrombin by antithrombin III can be promoted by nearly three orders of magnitude in the presence of heparin.⁷⁶⁻⁷⁷ As shown in Figure 2.6a and b, compared with the healthy human plasma treated with empty gel, both TR-HAHP and NR-HAHP solutions prolonged aPTT and PT by up to 100 s. These prolonged aPTT and PT can be attributed to the existence of heparin based on an antithrombin-dependent mechanism.⁷⁸ However, once cross-linked by UV irradiation, the NR-HAHP gel could not inhibit the coagulation while the TR-HAHP gel still showed a remarkable increased in the aPTT and PT levels, indicating the thrombin-specific release of HP from the TR-HAHP gel. We further evaluated the anticoagulant capability of the TR-HAHP *via* a thrombin clotting time (TCT) assay, which is commonly performed on patients for diagnosis of coagulopathy by adding thrombin to citrated plasma and recording the time when a stable clot is formed.⁷⁹ Consistent with the aPTT and PT results, TCT was significantly delayed in the presence of the TR-HAHP gel (Figure 2.6c).

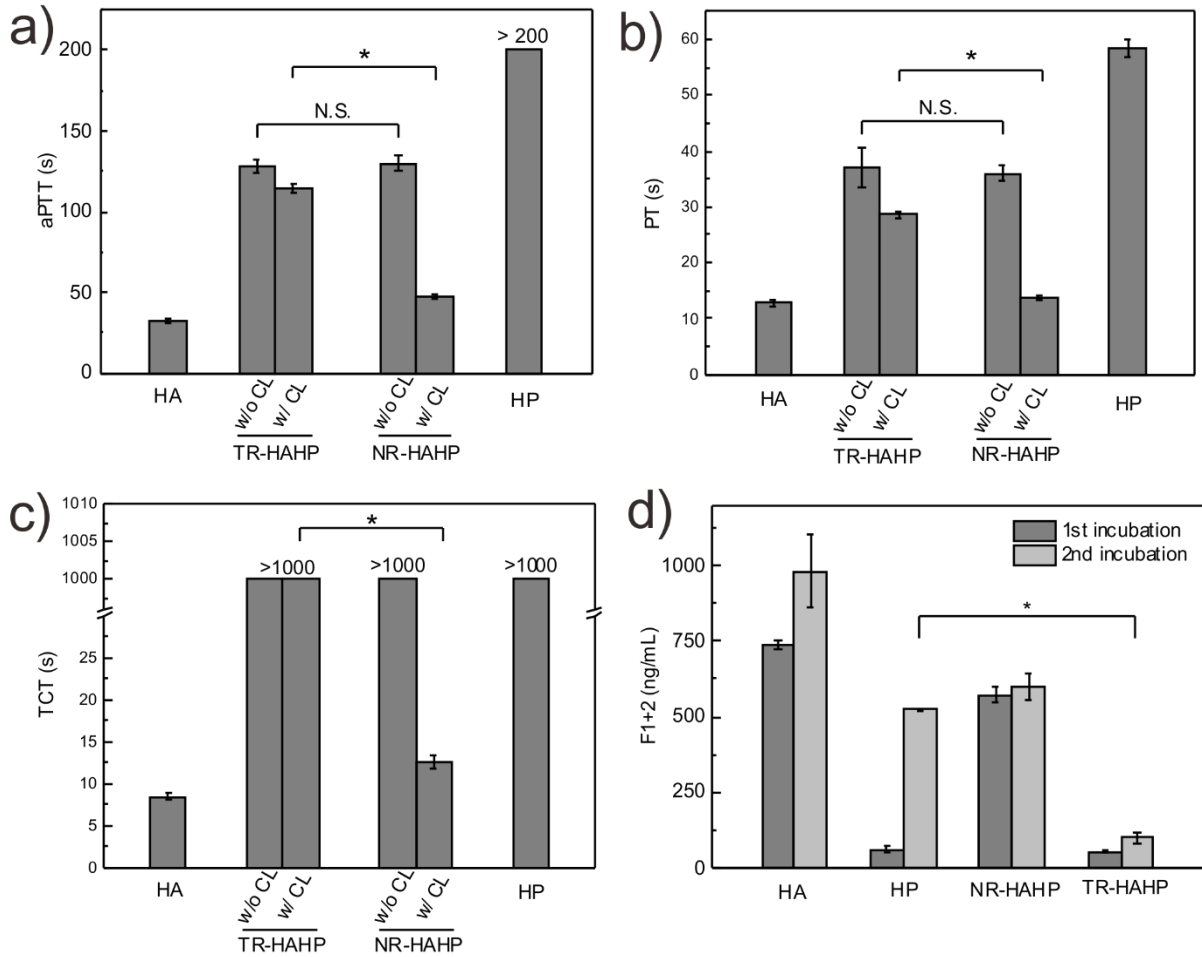


Figure 2.6 *In vitro* anticoagulant capacity of the TR-HAHP hydrogel. (a) *In vitro* analysis of the activated thromboplastin time (aPTT) of untreated (HA), HP treated, non-cross-linked, and cross-linked TR-HAHP or NR-HAHP treated plasma. (b) Prothrombin time (PT) tests of plasma incubated with HA, HP, TR-HAHP, and NR-HAHP hydrogels. (c) Thrombin clotting time (TCT) of plasma added with various hydrogels. (d) Concentrations of F1+2 fragment after each incubation period (3 h) indicates that only the TR-HAHP hydrogel can effectively suppress the thrombin generation during the second incubation. Error bars indicate s.d. (n = 3).

Encouraged by the above findings, we further incubated the hydrogels with human plasma twice with 3 h for each incubation cycle to examine the self-regulation ability of the TR-HAHP. Thrombin formation in plasma was determined by the level of the prothrombin F1+2 fragment, which is cleaved from prothrombin during the activation.⁸⁰ The coagulation activation levels of the TR-HAHP hydrogel versus non-responsive gels (HP and NR-HAHP) were reported in

Figure 2.6d. A high level of F1+2 was detected in the plasma incubated with the control groups (HA and NR-HAHP), while both HP gel and the TR-HAHP gel effectively inhibited coagulation activation in the first incubation cycle. In the presence of TR-HAHP hydrogel, plasma was protected from clotting over both investigated periods, whereas plasma in contact with the HP hydrogel could only prevent coagulation in the first incubation cycle due to the burst release of HP from the gel during the incubation. The thrombin responsiveness of the TR-HAHP enabled the controlled and repeatable HP release from the system, as less HP was released once thrombin was inhibited by the pre-released HP. The remarkable difference in F1+2 concentrations between plasmas incubated with the HP gel versus the TR-HAHP gel confirmed that the feedback system could inhibit coagulation over a long time period, as expected.

2.3.3 Fabrication and characterization of thrombin-responsive MNs

To achieve a functional form that enables painless and convenient HP delivery, we next fabricated a TR-HAHP MN-array patch to assess long-term anticoagulant regulation. Briefly, the TR-HAHP solution mixed with the cross-linker MBA and a photoinitiator was first loaded into the tip region of a silicone MN-mold by centrifugation. The cross-linked HA-based matrix enhances the stiffness of the MNs (Figure 2.7) for efficient penetration through the skin,¹ as well as restricts the loss of the TR-HAHP from the MNs. The MN-array contains 400 needles in a $12 \times 12 \text{ mm}^2$ patch with a 600- μm center-to-center interval (Figure 2.8a). Each MN was of a conical shape, with 300 μm in diameter at the base and 600 μm in height (Figure 2.8c). The fluorescence image in Figure 2.8b displayed a cross-sectional view of the MN with a

rhodamine-labeled *m*-HA matrix and FITC-labeled TR-HAHP loaded in MN tips with a homogenous distribution.

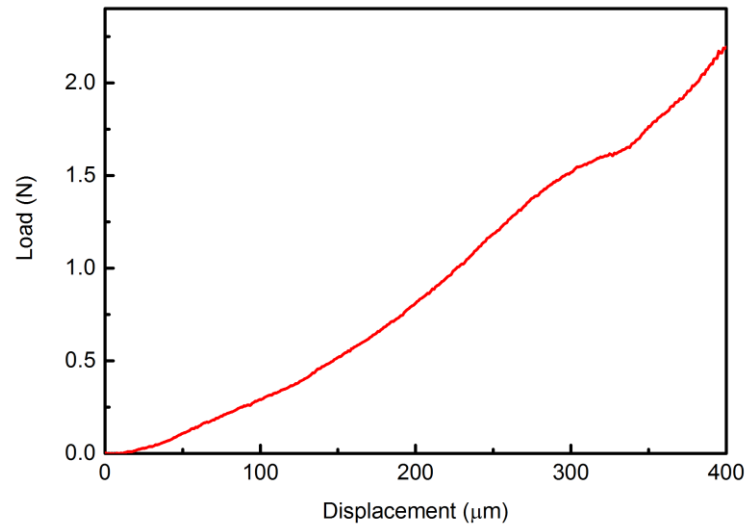


Figure 2.7 Mechanical behavior of one TR-HAHP MN.

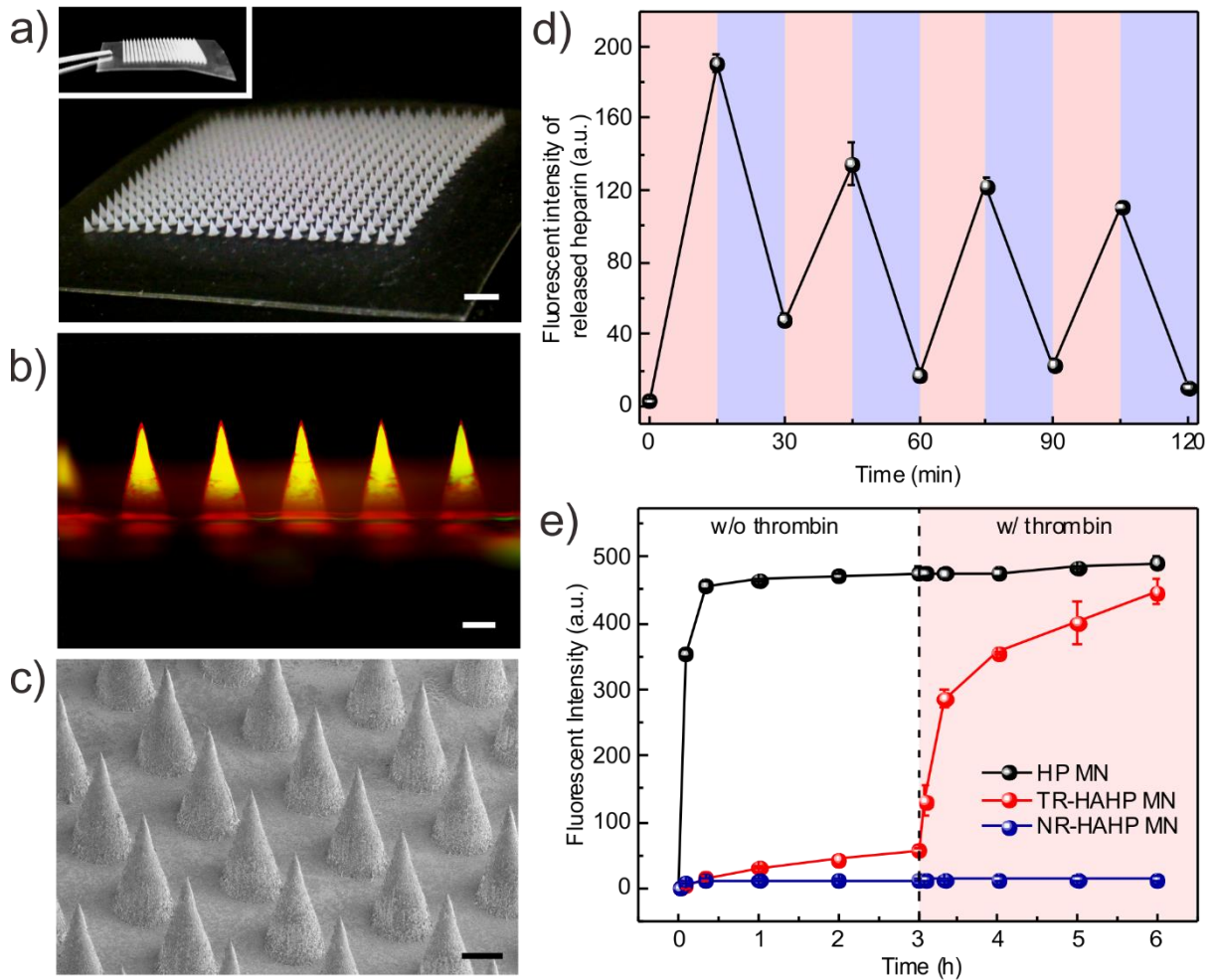


Figure 2.8 Fabrication and *in vitro* characterization of the TR-HAHP MN array patch. (a) Photos of the MNs array. Scale bar: 1 mm. (b) A fluorescence microscopy image of rhodamine-labeled MN loaded with FITC-labeled TR-HAHP. Scale bar: 200 μm . (c) A SEM image of MNs. Scale bar: 200 μm . (d) Pulsatile release profile of FITC-HP from the TR-HAHP MNs. (blue: w/o thrombin; pink: w/thrombin). (e) Self-regulated FITC-HP release from MNs in different thrombin solutions. Error bars indicate s.d. (n = 3).

The obtained TR-HAHP MNs exhibited thrombin-responsive performance similar to the TR-HAHP hydrogel. As shown in Figure 2.8d, a repeatable release profile of HP was observed corresponding to thrombin levels, which may further enable prolonged thrombin-mediated HP delivery. In addition, a tunable release kinetics can be achieved by varying the incubating condition (Figure 2.8e). A maximum of a 15.6-fold increase in the HP release rate was observed in 20 min once exposed to thrombin solution (0.6 U/mL). In contrast, the free HP-

loaded MNs exhibited a burst release in the Tris buffer even without thrombin, but an insignificant amount of HP was released from the NR-HAHP MNs.

2.3.4 *In vivo* studies in a thrombolytic challenge mouse model

To further evaluate the potential clinical relevance for the treatment of life-threatening acute thrombosis, we next verified the anticoagulant capacity of the TR-HAHP in a thrombotic challenge model.⁶⁹ The CD-1 mice were randomly divided into five groups (n=8), with one group intravenously (*i.v.*) injected with heparin solution and four groups transcutaneously administered with different samples: 1) the empty HA MN made of only cross-linked *m*-HA, 2) the HA MN encapsulating free HP (HP MN), 3) the TR-HAHP MN and 4) the NR-HAHP MN (HP dose: 200 U/kg). The MNs could penetrate the mouse skin efficiently, as evidenced by the hematoxylin and eosin (H&E) and trypan blue staining of the MN-treated tissue (Figure 2.9a), which allowed the MN tips to be exposed to the blood fluid in vascular-capillary network for real-time sensing and rapid response. The transient microchannels in the skin were quickly recovered 4 h post MN injection (Figure 2.10).

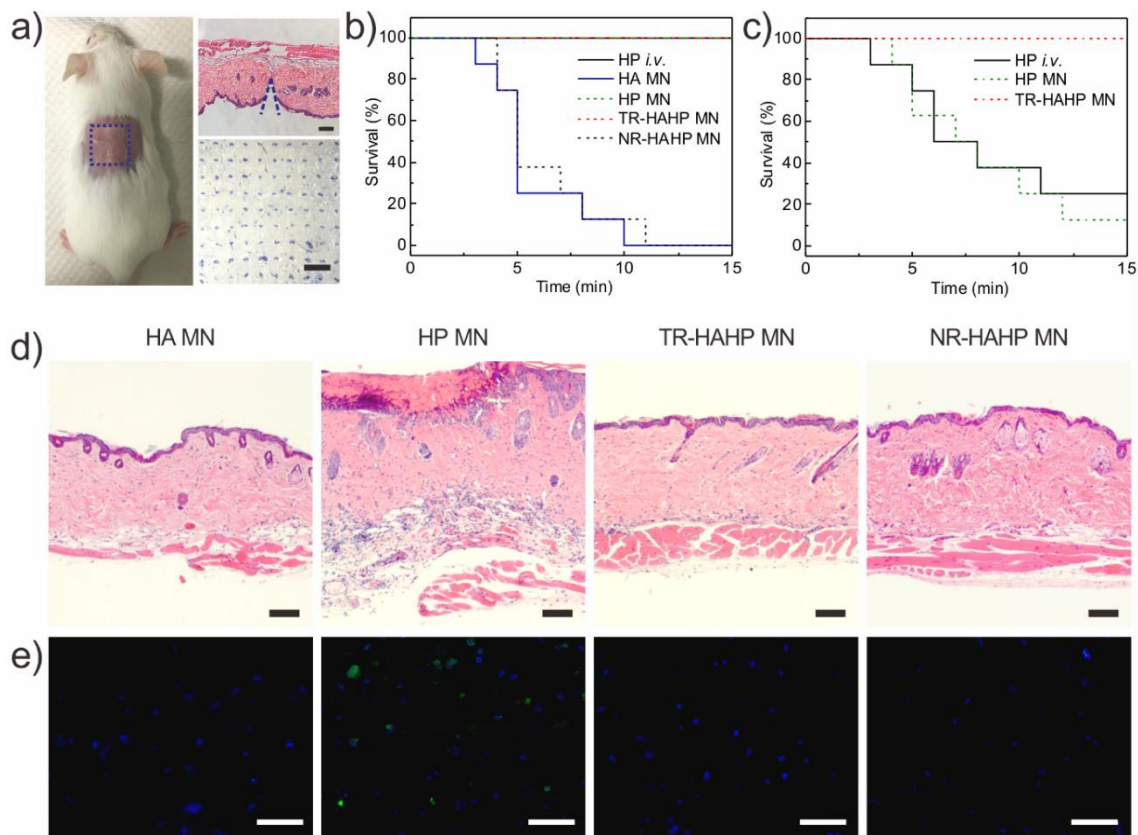


Figure 2.9 *In vivo* studies of the TR-HAHP patch for thrombosis prevention. (a) Photograph of a mouse transcutaneously administered with the MN array patch (left). H&E-stained microscopy image of mouse skin penetrated by one MN (right top) and the image of the trypan blue staining (right bottom) showing the penetration of the MN patch into the mouse skin. Scale bars are 100 μm and 1 mm, respectively. (b) Kaplan–Meier survival curves for the mice challenged with thrombin injection. Each group was pre-treated with HP *i.v.* injection or different types of the MN patch (HP: 200 U/kg). Shown are eight mice per treatment group. (c) Kaplan–Meier survival curves for thrombotic challenge mouse model 6 h post MN treatments (HP: 200 U/kg). Shown are eight mice per treatment group. (d) H&E-stained sections of mouse skin tissue at the MN-treated sites. Scale bar: 100 μm . (e) Immunofluorescence images of mouse skin tissue stained with TUNEL assay (green) and Hoechst (blue). Scale bar: 50 μm .

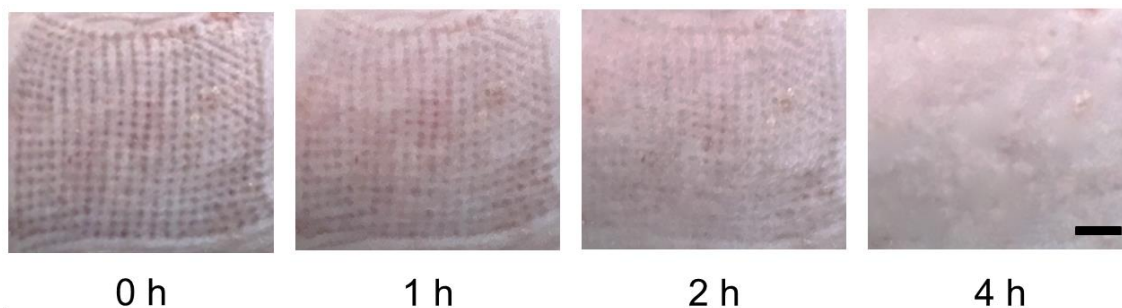


Figure 2.10 Skin puncture marks at 0, 1, 2 and 4 h post-treatment. Scale bar: 2 mm.

Each mouse was *i.v.* injected with thrombin (1000 U/kg) to induce an acute thromboembolism, which can lead to mortality in ~ 92% of mice.⁸¹ Heparin solution was *i.v.* injected into the mice before thrombosis induction. The MN patches were pre-administered on the dorsum skin of the mice 10 min before the challenge to be tested. All animals with empty HA MN or the NR-HAHP MN died within 15 min after the injection of thrombin, whereas all mice survived with the treatment of HP MN or TR-HAHP MN (Figure 2.9b) during the 15 min. The significantly enhanced survival rate implied fast and efficient HP release from the TR-HAHP MN in response to increased thrombin, which protected the mice from the thrombolytic risk. Through FITC labeled heparin, the *in vivo* release triggered by thrombin was also verified by fluorescence microscopy (Figure 2.11). In a further step, we also examined the survival rate 6 h post administration of MN patches and heparin injection. It was demonstrated that $\geq 80\%$ of mice treated with the HP MNs or *i.v.* injection of heparin died as a result of the short half-life of HP (~ 1 h) (Figure 2.9c).⁸² The increased mortality rate 6 h post administration of HP MNs suggested that the burst release of HP was not able to ensure protection from thrombotic risk. Contrary to the behavior of HP MN, the TR-HAHP MN maintained its function of anticoagulation and protected the animals from death. The superior anticoagulant capacity of TR-HAHP MN was also evidenced by H&E staining of lung sections. There were insignificant differences observed in the lung of mice treated with TR-HAHP MN compared with healthy mice (Figure 2.12 and 2.13); but intravascular and interstitial hemorrhage, blocked blood vessels, and atelectasis were observed in the challenged groups 6 h post administration of HP injection or HP MN (Figure 2.13). These data indicate that the stimulus-triggered feature of the TR-HAHP system enables its potential application in self-administered therapy.

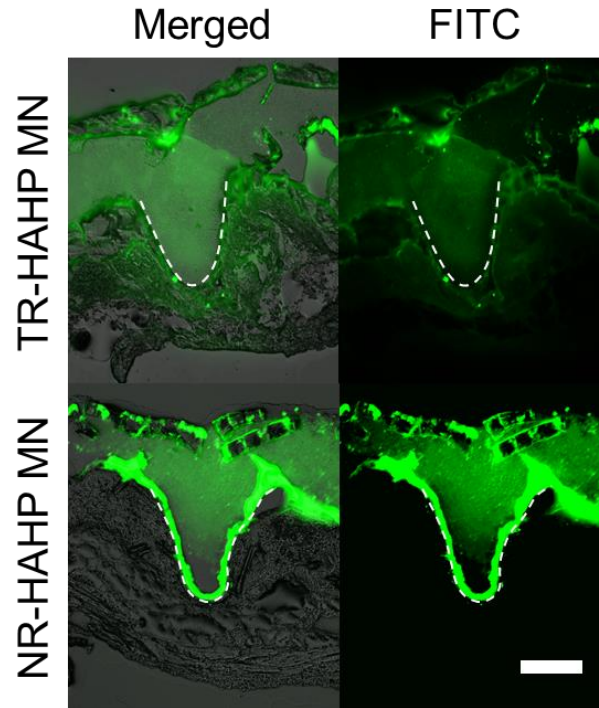


Figure 2.11 Representative images of FITC-labeled TR-HAHP MNs and NR-HAHP MNs inserted into mice skins after injection of thrombin (1000 U/kg). The white dashed line indicates the boundary of the injected MN. Scale bar: 200 μ m.

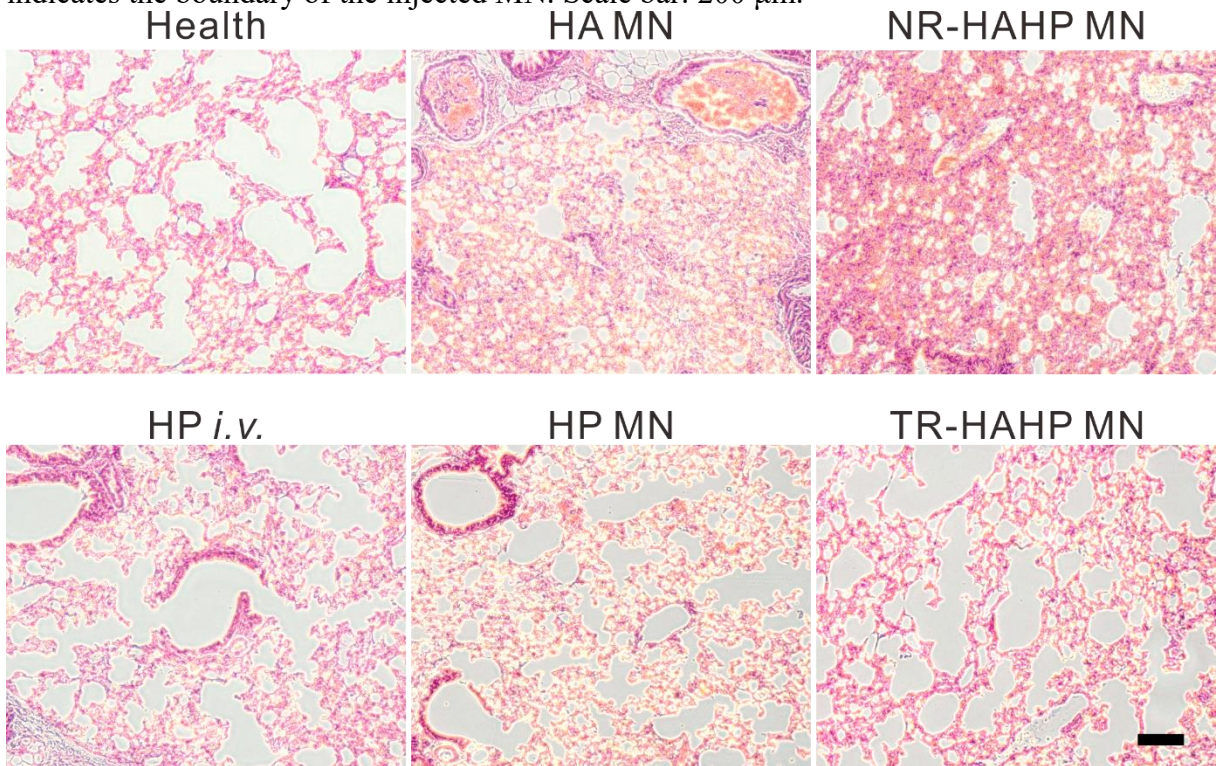


Figure 2.12 Histological observation of the lungs of the mice treated with HA, HP, TR-HAHP and NR-HAHP MNs after challenge of thrombin. Scale bar: 100 μ m.

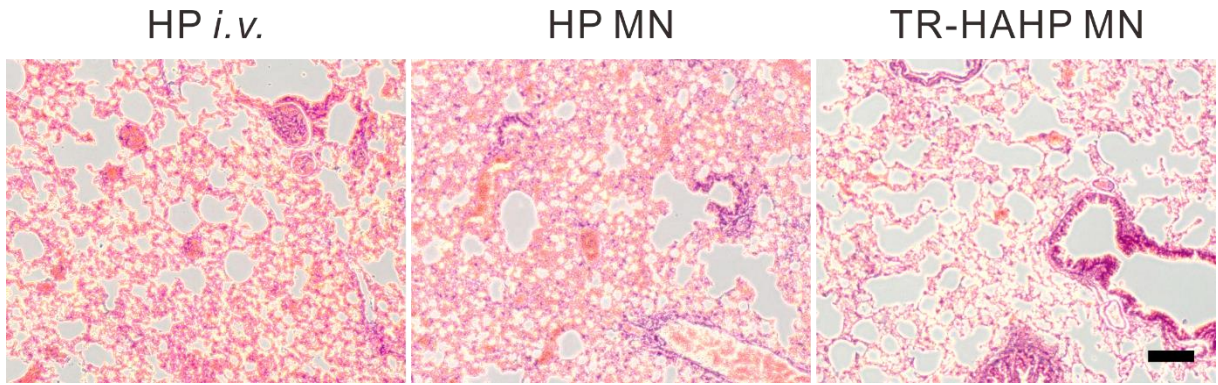


Figure 2.13 Histological observation of the lungs of the thrombotic challenge mice 6-h post treatment with HP *i.v.* injection, HP MNs, and TR-HAHP MNs Scale bar: 100 μm .

To further investigate the biocompatibility of the MN-array patches, the mouse skin surrounding the MN-treated area was excised for histological analysis after 24 h-administration. The pure HA MN was regarded as a negative control, which exhibited high biocompatibility as observed in the H&E stained histological images (Figure 2.9d and Figure 2.14), whereas obvious damage was observed in the skin treated with HP MN. The H&E images indicated neutrophil infiltration and a severe pathophysiological response because the HP caused subcutaneous bleeding. On the contrary, there were insignificant lesions at the TR-HAHP MN treated site because no HP leaked from the MN in the absence of thrombin. Moreover, as presented in the skin tissues stained with the *in situ* TUNEL assay, obvious cell apoptosis occurred in the skin treated with HP MN, while no significant cell death was observed in the skin treated with the TR-HAHP MN, NR-HAHP and pure HA MN (Figure 2.9e). Finally, the TR-HAHP MN avoided unwanted bleeding due to the locally generated, and considerably lower levels of activated thrombin at the sealing of the major wounds,⁸³⁻⁸⁴ which could not be sensed by the MNs in the treated subcutaneous tissue (Figure 2.15).³⁹

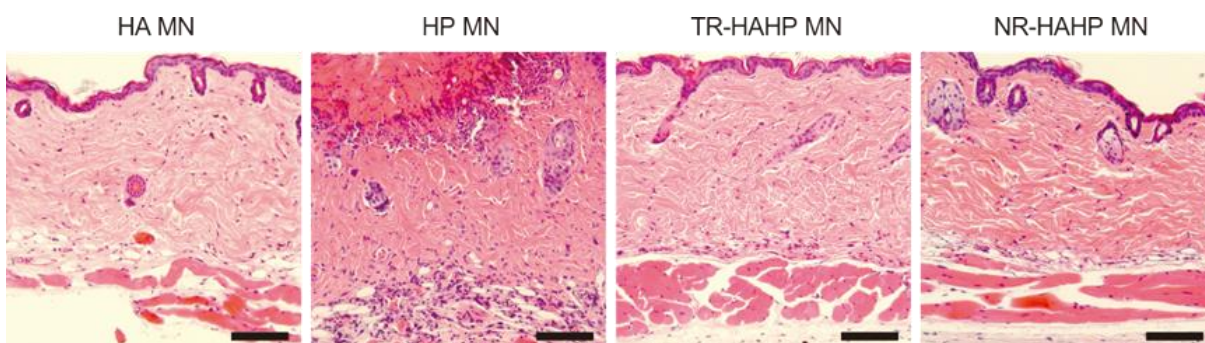


Figure 2.14. H&E-stained skin sections administered HA, HP, TR-HAHP and NR-HAHP MNs (from left to right) with surrounding tissues 24 h postadministration of the MN-array patch. Scale bar: 100 μ m.

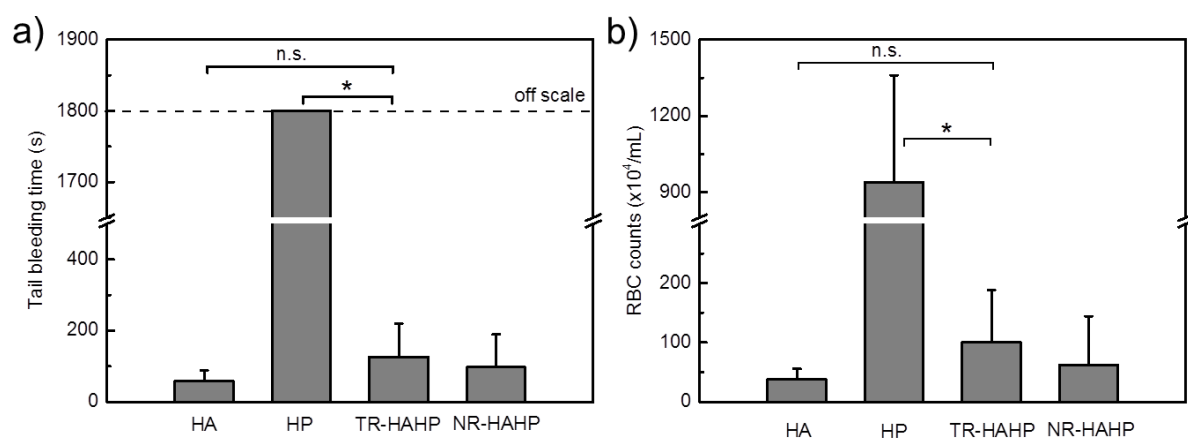


Figure 2.15 (a) Tail transection bleeding time and (b) amounts of red blood cells from the tail wound of animals pretreated with empty HA MN, HP MN, TR-HAHP MN, and NR-HAHP MN. Error bars indicate s.d. (n=5).

2.4 Conclusion

In conclusion, we developed a thrombin-responsive patch for auto-regulation of blood coagulation by integrating a TR-HAHP matrix with a MN-array. The thrombin-cleavable peptide unit enabled thrombin-specific activation of drug release from the system with a rate highly dependent on the thrombin concentration. More importantly, it enabled feedback-controlled anticoagulation therapy with minimized risk of over- or under-dosage. The *in vivo* studies in a thrombolytic challenge model demonstrated effective long-term protection from acute pulmonary thromboembolism. Taken together, this work provides a platform for

designing closed-loop based drug delivery systems for the treatment of intravascular diseases according to levels of related biomarkers. Moreover, the integration of MNs with stimuli-responsive drug carriers extends the administration methods of therapeutics.

CHAPTER 3 LOCALLY-INDUCED ADIPOSE TISSUE BROWNING BY MICRONEEDLE PATCH FOR OBESITY TREATMENT

3.1 Introduction

Obesity has been classified as a disease by the American Medical Association in 2013 and recognized as one of the most serious public health problems in the 21st century associated with rapid global socioeconomic development.⁸⁵ Obesity-associated disorders such as type-2 diabetes, cardiovascular diseases, and cancer, have become a global threat to human health. Particularly in the United States, more than one-third of the adult population is obese, and the prevalence is going to soar in the next decades.⁸⁶ Current treatments toward obesity include restriction of calorie intake by diet programs, promoting energy expenditure through physical exercise, pharmacological therapy, as well as bariatric surgeries and liposuction.⁸⁷⁻⁸⁸ However, most therapeutics come with undesired side effects on human organs such as gastrointestinal, liver, and kidney,⁸⁹⁻⁹⁰ and surgeries have high risks.⁹¹ Therefore there is an urgent requirement to exploit effective treatments for obesity.

Recent studies have revealed a crucial role of brown adipose tissue (BAT), a primary heat generation organ, in energy expenditure in mammals.⁹²⁻⁹³ It is known that the white adipose tissue (WAT) stores exceeded energy as triglycerides, leading to overweight; whereas BAT dissipates energy by producing heat through nonshivering thermogenesis, which may facilitate the suppression of obesity.⁹⁴ The transformation of WAT into BAT provides an alternative approach for the treatment of obesity and related metabolic disorders, which has garnered increasing attention in the past decade.⁹⁵⁻⁹⁷ A variety of genes and pathways that regulate adipocyte development have been identified.^{88, 98} However, numerous browning agents that

can promote “browning” on WAT face challenges in clinical application because of undesired side effects on other organs as a result of broad targeting spectrum.⁹⁹⁻¹⁰¹

In this chapter, we report a locally induced browning technology that based on a degradable microneedle (MN) patch consisted of drug-loaded nanoparticles (NPs) and crosslinked matrix (Figure 3.1). Rosiglitazone (Rosi) or CL 316243 was loaded in the NPs as the model browning agents.¹⁰² The NPs can be further integrated into a microneedle (MN)-array based transdermal device for sustained drug delivery into subcutaneous adipose tissue. The MN patch provides a localized, convenient, and painless administration method.^{1, 30, 33, 103} In a mouse model, we have demonstrated that this MN patch can offer local delivery of browning reagents in a safe and effective manner for inhibition of adipocyte hypertrophy and the consequent improvement of metabolism.

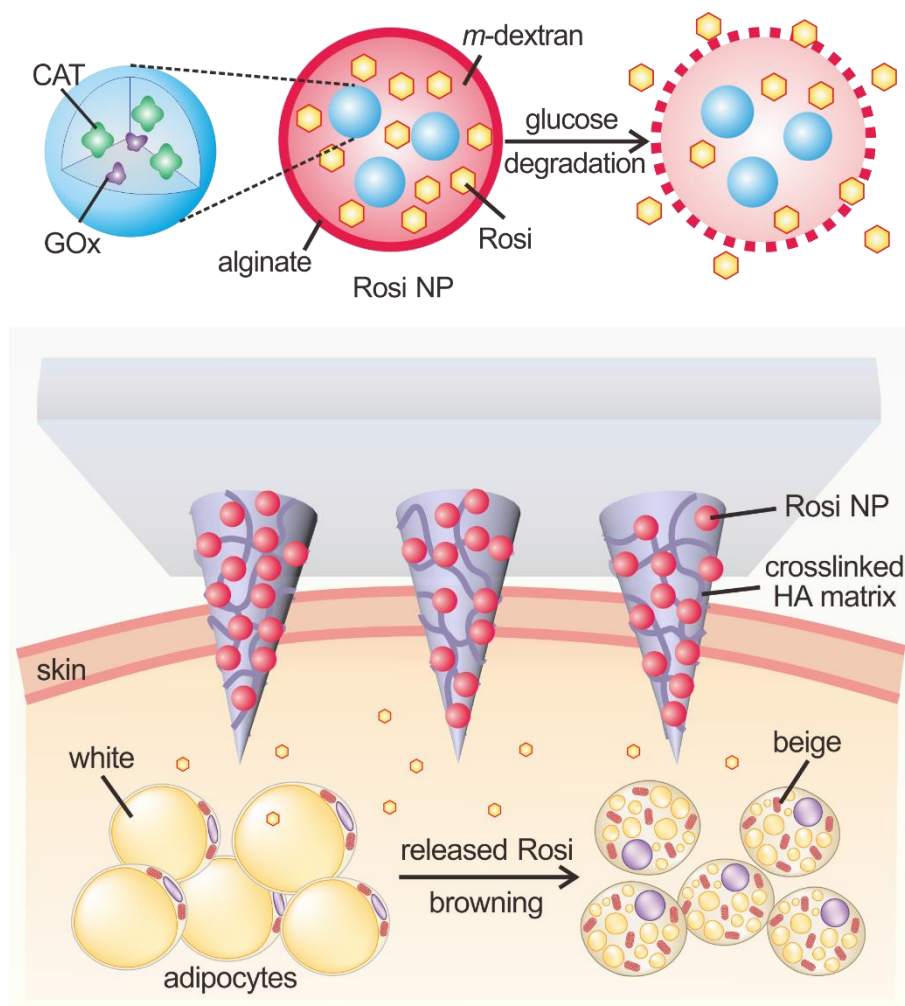


Figure 3.1 Schematic illustration of the browning reagents-loaded transcutaneous MN patch. Nanoparticles (NPs) encapsulating rosiglitazone (Rosi), glucose oxidase (GOx), and catalase (CAT) are prepared from pH-sensitive acetal-modified dextran and coated with alginate. NPs are further loaded into the microneedle-array patch made of crosslinked hyaluronic acid (HA) matrix for the brown remodeling of the white fat.

3.2 Experimental Section

3.2.1 Materials

All chemicals were purchased from Sigma-Aldrich unless otherwise specified and were used as received. Rosiglitazone was ordered from Abcam (Cambridge, MA). CL 316243 was purchased from Cayman Chemical (Ann Arbor, MI). The deionized water was prepared by a Millipore NanoPure purification system (resistivity higher than $18.2 \text{ M}\Omega \text{ cm}^{-1}$).

3.2.2 Synthesis of pendant acetal-modified dextran (*m*-dextran)

1.0 g of dextran ($M_n = 9\sim 11\text{kDa}$) was added to a flame-dried round-bottom flask and purged with nitrogen. 10 mL of anhydrous dimethyl sulfoxide (DMSO) was added to the flask and stirred until complete dissolution of the dextran. Pyridinium *p*-toluenesulfonate (PPTS, 15.6 mg, 0.062 mmol) was added to the solution followed by the addition of 2-ethoxypropene (4.16 mL, 37 mmol). The reaction mixture was purged with nitrogen and sealed with parafilm to prevent reactant evaporation. The reaction was stirred at room temperature for 30 min, and then quenched by the addition of 1 mL of triethylamine. The mixture was then precipitated and washed three times in basic water (pH ~ 8) to prevent undesired degradation and collected by centrifugation at 8000 rpm for 15 min. The product was lyophilized to obtain white solid. ^1H NMR (DMSO- d_6 , 300 MHz, δ ppm): 1.10 (m, OCH_2CH_3), 1.30 (m, $\text{C}(\text{CH}_3)_2$), 3.40 (m, OCH_2CH_3), 3.55-3.85 (br, dextran $\text{C}_2\text{-H} \sim \text{C}_6\text{-H}$), 4.88 (br, dextran $\text{C}_1\text{-H}$)

3.2.3 Preparation of rosiglitazone-loaded dextran nanoparticles

Dextran nanoparticles were prepared by an improved double emulsion method as reported before.¹⁰⁴ Briefly, 5 mL dichloromethane (DCM) containing 200 mg of *m*-dextran and 20 mg Rosi was emulsified with 0.5 mL of aqueous solution containing 3.5 mg of enzymes (weight ratio of glucose oxidase to catalase 4:1) by sonication for 45 cycles (1 s each with a duty of 40%). The resulting primary solution was further poured into 25 mL of 1% alginate aqueous solution ($M_v = 1.6 \times 10^5$ Da) for another 45-cycle sonication. The double emulsion was immediately transferred into 150 mL of 0.2% alginate and stirred at room temperature for 2 h to evaporate DCM. Afterward, nanoparticles were collected by centrifugation at 10000 rpm and washed with distilled water three times. The loading capacity (LC) and encapsulation

efficiency (EE) of Rosi were determined by measuring the UV-vis absorption of the released Rosi from nanoparticles using a Nanodrop 2000C spectrometer (Thermo Scientific) at absorbance 317 nm. LC and EE were calculated as $LC = B/C$, $EE = B/A$, where A was expected encapsulated amount of Rosi, B was the encapsulated amount of Rosi, and C was the total weight of the particles. Particle size and polydispersity intensity were measured by dynamic light scattering (DLS). The zeta potential of the NPs was determined by their electrophoretic mobility using the same instrument after appropriate dilution in DI water. Measurements were made in triplicate at room temperature. NPs morphology was investigated by a FEI Verios 460L field-emission scanning electron microscope (FESEM).

3.2.4 *In vitro* release studies

The *in vitro* release profile of Rosi from dextran nanoparticles was evaluated through incubation of nanoparticles in 1 mL of PBS buffer (NaCl, 137 mM; KCl, 2.7 mM; Na₂HPO₄, 10 mM; KH₂PO₄, 2 mM; pH 7.4) at 37°C on an orbital shaker, to which 100 mg/dL glucose was added to reach normoglycemic level in human body. At predetermined time points, the sample was centrifuged (10000 rpm, 1 min) and 10 µL of the supernatant was taken out for analysis by measuring the UV-vis absorbance at 317 nm using a Nanodrop 2000C spectrometer.

3.2.5 Fabrication of browning agent MN patch

All the MNs in this study were fabricated using the uniform silicone molds from Blueacre Technology Ltd. Each needle had a 300 µm by 300 µm round base tapering to a height of 800 µm. The needles were arranged in an 11 × 11 array with 600 µm tip-to-tip spacing. To fabricate a nanoparticle-loaded microneedle, the prepared nanoparticle suspension was first deposited

by pipet onto the MN mold surface (30 $\mu\text{L}/\text{array}$). Then, molds were placed under vacuum (600 mmHg) for 5 min to allow the solution filled the MN cavities. Afterward, the covered molds were centrifuged using a Hettich Universal 32R centrifuge for 10 min at 2000 rpm. Finally, 3 mL of premixed *N,N'*-methylenebis(acrylamide) (MBA, w/v 2%), photoinitiator (Irgacure 2959, w/v 0.5%) and *m*-HA solution(w/v 4%) was added into the prepared micromold reservoir and allowed to dry at 20 $^{\circ}\text{C}$ under vacuum desiccator. *m*-HA was synthesized following the previous reported method.⁶⁷ After complete desiccation, the MN patch was carefully detached from the silicone mold and underwent the cross-linking polymerization *via* UV irradiation (wavelength: 365 nm at an intensity of 9 mW/cm^2) for 30 s. The resulting MN-array patches were stored in a sealed six well container for later study. The morphology of the MNs was characterized *via* a FEI Verios 460L field-emission scanning electron microscope (FESEM).

3.2.6 Mechanical strength test

The mechanical strength of MNs was measured by pressing MNs against a stainless steel plate. The speed of the top stainless steel plate movement towards the MN-array patch was 1 $\mu\text{m}/\text{s}$.

3.2.7 Skin penetration efficiency test

After administered with the MN-array on skin at the inguinal site, mice were euthanized by CO_2 asphyxiation, and the skin was excised and stained with trypan blue for imaging by optical microscopy (Leica EZ4 D stereo microscope). To evaluate the biocompatibility of the MN-array patches, the tissue samples were fixed in 10% formalin for 18 h and then embedded in

paraffin, cut into 50 μm sections, and stained using hematoxylin and eosin (H&E) for histological analysis.

3.2.8 *In vivo* browning studies in lean mice

Eight-week old male C57BL/6 mice ordered from Charles River (Raleigh, NC) or the Jackson Laboratory were used. The animal study protocols were approved by the Institutional Animal Care and Use Committee at North Carolina State University and University of North Carolina at Chapel Hill, or by the Columbia University Animal Care and Utilization Committee. Mice were caged at $22 \pm 1^\circ\text{C}$ with free access to water and regular chow diet on a 12 h light/dark cycle. Mice were given least 1 week adaption before experiments. Three groups of animals ($n=6$) were treated with empty HA MN patch (EV), Rosi NP-loaded MN patch (10 mg/kg) (Rosi), or CL316243 NP-loaded MN patch (1 mg/kg) (CL) respectively on inguinal regions every 3 days. For indirect calorimetric studies, mice were subjected to the Comprehensive Lab Animal Monitoring System (CLAMS). Metabolic activities were monitored during the treatment, including oxygen consumption, food intake, locomotor activity and body weight. Six days post administration, animals were sacrificed and inguinal adipose tissues were collected for histological and RNA analysis. Interscapular BAT and epididymal WAT were weighted.

3.2.9 Browning MN patch treatments on diet induced obesity (DIO) mice

Male C57BL/6 mice were fed on a HFD (60% kcal from fat) for 8 weeks to induce obesity and insulin resistance. Three groups with five mice for each group were treated with empty HA, Rosi (10 mg/kg), or CL316243 (1 mg/kg) through a transdermal patch on one side of the

inguinal areas under isoflurane anesthesia. The other side of inguinal tissue of each mouse was administrated with an empty HA microneedle patch. The patch was changed every 3 days for 4 weeks. Body weight was monitored during the treatment period. The glucose tolerance test was performed in mice 3-weeks post-treatment. The mice were fasted for 16 h (overnight) before glucose administration. The mice were intraperitoneal injected with glucose at 2 g/kg diluted in PBS and blood glucose levels were monitored over time. At the end of 4-weeks MN treatment, the animals were euthanized by CO₂ asphyxiation, and adipose tissues (inguinal WAT, epididymal WAT, and interscapular BAT) were collected for analyses. The skin tissues around the treated areas were also collected for biocompatibility evaluation of MN patches.

3.2.10 RNA analysis

RNA was extracted from tissues or cells by combining TriZol reagent and NucleoSpin RNA kit with DNase I digestion (Macherey-Nagel) following manufacture's instruction. 1 µg total RNA was used to synthesize cDNA by using the High-capacity cDNA Reverse Transcription kit (Applied Biosystems). Quantitative real-time PCR (Q-PCR) were performed on a Bio-Rad CFX96 Real-Time PCR platform by using the GoTaq qPCR Master Mix (Promega). Relative gene expressions were calculated by using $\Delta\Delta C_t$ method with Cyclophilin A (cultured cells) or RPL23 (tissues) as the reference gene. Primer sequences are listed in Table 3.1.

Table 3.1 Q-PCR Primer sequences.

Genes	Q-PCR Primer sequences
<i>Adipsin</i>	Forward: CATGCTCGGCCCTACATGG Reverse: CACAGAGTCGTCATCCGTCAC
<i>Adiponectin</i>	Forward: GCACTGGCAAGTTCTACTGCAA Reverse: GTAGGTGAAGAGAACGGCCTTGT
<i>aP2</i>	Forward: ACACCGAGATTTCTTCAAAGT Reverse: CCATCTAGGGTTATGATGCTCTTCA
<i>Cidea</i>	Forward: TGCTCTTCTGTATCGCCCAGT Reverse: GCCGTGTTAAGGAATCTGCTG
<i>Cox7a1</i>	Forward: CAGCGTCATGGTCAGTCTGT Reverse: AGAAAACCGTGTGGCAGAGA
<i>Cox8b</i>	Forward: GAACCATGAAGCCAACGACT Reverse: GCGAAGTTCACAGTGGTTCC
<i>Cyclophilin A</i>	Forward: TATCTGCACTGCCAAGACTGAGTG Reverse: CTTCTTGCTGGTCTTGCCATTCC
<i>Dio2</i>	Forward: AGAGTGGAGGCGCATGCT Reverse: GGCATCTAGGAGGAAGCTGTTC
<i>Elovl3</i>	Forward: CCAACAACGATGAGCAACAG Reverse: CGGGTTAAAAATGGACCTGA
<i>IL-6</i>	Forward: TTCCATCCAGTTGCCTTCTT Reverse: ATTTCCACGATTTCCCAGAG

Table 3.1 Continued

<i>Perilipin</i>	Forward: GGCCTGGACGACAAAACC Reverse: CAGGATGGGCTCCATGAC
<i>Pgc-1α</i>	Forward: CCCTGCCATTGTAAAGACC Reverse: TGCTGCTGTTCCCTGTTTTTC
<i>Pparγ1</i>	Forward: AGAAGCGGTGAACCACTGAT Reverse: GAATGCGAGTGGTCTTCCAT
<i>Pparγ2</i>	Forward: TCTGGGAGATTCTCCTGTTGA Reverse: GGTGGGCCAGAATGGCATCT
<i>Prdm16</i>	Forward: TGGCCTTCATCACCTCTCTGAA Reverse: TTTCTGATCCACGGCTCCTGTGA
<i>Resistin</i>	Forward: AAGAACCTTTCATTTCCCCTCCT Reverse: GTCCAGCAATTTAAGCCAATGTT
<i>Rpl23</i>	Forward: TGTCGAATTACCACTGCTGG Reverse: CTGTGAAGGGAATCAAGGGA
<i>Ucp1</i>	Forward: ACTGCCACACCTCCAGTCATT Reverse: CTTTGCCTCACTCAGGATTGG

3.2.11 Statistical analysis

All results were presented as Mean \pm SEM or Mean \pm SD. Statistical analysis was performed using Student's *t*-test. With a *p* value < 0.05 , the differences between experimental groups and control groups were considered statistically significant.

3.3 Results and Discussion

3.3.1 Synthesis and characterization of Rosi-loaded NPs

The degradable NPs were prepared using an acid-sensitive dextran derivative by a double emulsion method.¹⁰⁴ The acid-sensitive dextran was synthesized through conjugation with ethoxypropene *via* an acid-catalyzed reaction, which rendered the derived dextran (*m*-dextran) with 89% substitution of hydroxyl to pendant acetals (Figure 3.2). Rosi, an agonist of peroxisome proliferator-activated receptor gamma (PPAR γ), has been reported to stimulate adipose tissue transformation by upregulating uncoupling proteins, VEGF, and angiopoietin-like 4.¹⁰⁵⁻¹⁰⁶ We encapsulated Rosi in the dextran NPs for WAT browning. Two enzymes, glucose oxidase (GOx) and catalase (CAT), were introduced into the system to generate acidic environment under the physiological glucose concentration. The GOx is able to convert glucose to gluconic acid to decrease the local pH;²⁹ while the CAT helps consume undesired hydrogen peroxide produced during the GOx-mediated enzymatic reaction.¹⁰⁷⁻¹⁰⁸ The resulting NPs had spherical shapes with monodisperse distribution as shown in the scanning electron microscopy (SEM) image (Figure 3.3e). The hydrodynamic particle size was around 250 nm as determined by dynamic light scattering (DLS) (Figure 3.3a). The NPs had a loading capacity of 5.2 wt % and encapsulated efficiency was around 55%. To monitor the release kinetics of Rosi, the NPs were incubated in the PBS buffer containing glucose at a normoglycemic level (100 mg/dL) in the human body. Then, the NPs gradually disassociated in the enzyme-induced acidic environment, triggering the encapsulated drug release (Figure 3.3b). The NPs with GOx gradually degraded in 3 days according to the reduction of the UV absorbance at 400 nm (Figure 3.3d), and subsequently released the embedded drug (Figure 3.3c, e). On the contrary, insignificant drug was collected from the NPs without GOx.

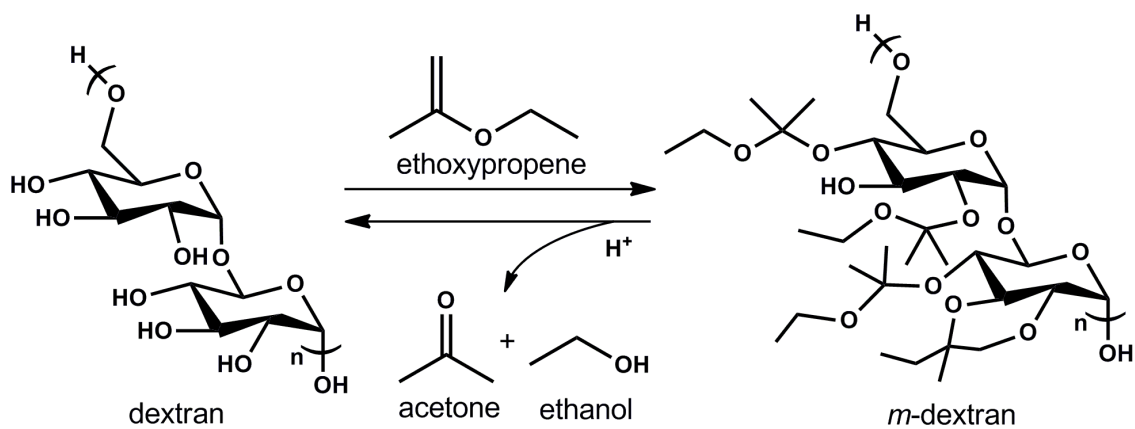


Figure 3.2 Scheme of synthesis and dissociation routes of *m*-dextran.

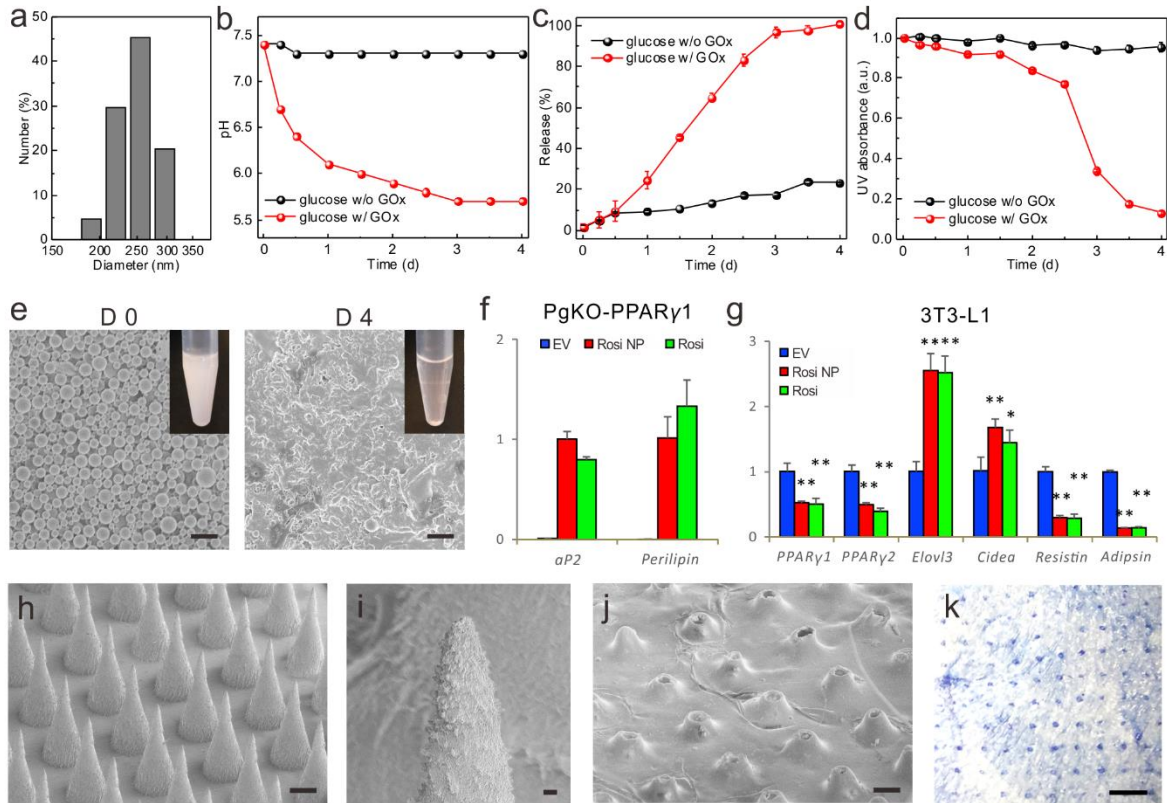


Figure 3.3 Fabrication and characterization of browning reagent microneedles. (a) The average hydrodynamic sizes of Rosi NPs determined by DLS. (b) Relevant pH changes of dextran NPs with or without GOx in PBS buffer in the presence of 100 mg/dL glucose. (n=3) (c) *In vitro* accumulated Rosi release from the acid-degradable dextran NPs (w/ or w/o GOx) in PBS buffer containing 100 mg/dL glucose at 37°C. (n=3) (d) UV absorbance of NPs suspensions $A_{400\text{ nm}}$. (n=3) (e) SEM images of Rosi NPs incubated in PBS buffer with 100 mg/dL glucose at 37 °C on day 0 and day 4 (scale bar: 2 μm), inset pictures show the transparency change of the NPs suspension. (f) Comparable adipogenesis between Rosi NPs- and Rosi compound-treated PgKO-MEFs as assessed by *aP2* and *Perilipin* gene expression. (n=4). (g) Same level of browning induced by Rosi NPs or Rosi compound in the mature 3T3-L1 white adipocytes. (n=4). (h) SEM image of the MN array (scale bar: 200 μm). (i) Higher magnification of SEM imaging of MN tip confirmed that the MN was loaded with NPs (scale bar: 10 μm). (j) SEM image of MNs 3 days post administration. (scale bar: 200 μm) (k) Trypan blue staining image of mouse skin administered with MN patch (scale bar: 1 mm). Error bars indicate standard deviation (SD), two-tailed Student's *t*-test, * $P < 0.05$, ** $P < 0.01$.

To validate the efficiency of Rosi NPs, we employed *in vitro* adipocyte model PgKO-PPAR γ 1 in which the reconstitution of a shorter form of PPAR γ (γ 1) in *Pparg*^{-/-} mouse embryonic fibroblast (MEF) rescues adipocyte differentiation only in the presence of exogenous

thiazolidinedione class of ligand (*e.g.* Rosi).¹⁰⁹ Rosi NPs were as efficient as nude Rosi to induce adipocyte formation, evidenced by the same induction of lipid droplet-binding protein genes *aP2* and *Perilipin* (Figure 3.3f), both of which are canonical PPAR γ target genes. Besides the adipogenic potential, we also compared the browning capacity of Rosi NPs. In fully differentiated 3T3-L1 adipocytes, Rosi NPs behaved the same as nude Rosi to up-regulate brown adipocyte markers *Elovl3* and *Cidea* as well as to repress white adipocyte genes *Resistin* and *Adipsin* (Figure 3.3g).¹¹⁰ Therefore, our nanoparticle strategy is able to sustain a constant release of Rosi at the physiological level of glucose without affecting its efficiency.

3.3.2 Fabrication and characterization of browning agent MN-array patch

The NPs were further embedded into a polymeric MN-array patch for local delivery of browning reagents. Briefly, the NPs were first loaded into the tip region of a silicone MN-mold by centrifugation, following with the addition of base solution. Methacrylated hyaluronic acid (*m*-HA) was selected as the base material, considering its good biocompatibility and mechanical property.^{20, 61} The *m*-HA base solution mixed with the cross-linker *N,N'*-methylenebis(acrylamide) (MBA) and a photoinitiator was further cross-linked through polymerization reaction upon exposure to UV light (365 nm, 9 mW/cm² for 30s). The cross-linked HA-based matrix can enhance the stiffness of the MNs (Figure 3.4) for efficient penetration through the skin,^{1, 38} as well as enable sustained release of drug from the MN tips, which helps maintain local constitutive high drug concentrations in adipose tissues. The MN-array contains 121 needles in a 7 \times 7 mm² patch with a center-to-center interval of 600 μ m. Each MN was of a conical shape, with 300 μ m in diameter at the base and 800 μ m in height (Figure 3.3h). The zoomed SEM image confirmed the distribution of NPs in the tip (Figure 3.3i).

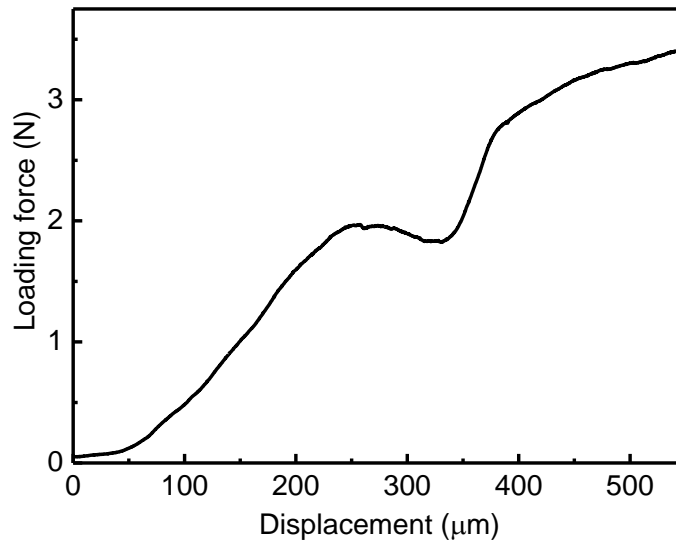


Figure 3.4 Mechanical behavior of one NP-loaded MN.

3.3.3 *In vivo* studies of the MNs on lean mice

We next examined the *in vivo* browning efficacy of the system in a mouse model. In addition to Rosi, we employed CL 316243, a β 3-adrenergic receptor agonist, in the dextran NPs and loaded in the MNs. CL 316243 is a potent thermogenic activator but through a distinct mechanism from Rosi.¹¹¹⁻¹¹³ It stimulates G protein G_{α_s} to activate adenylate cyclase, and consequently causes the accumulation of cyclic adenosine monophosphate (cAMP), which leads to thermogenesis and lipolysis.¹¹⁴⁻¹¹⁵ By including this distinctive browning agent, we would like to evaluate the applicability of our system to other drugs. Specifically, wide-type C57BJ/6 mice were randomly divided into three groups (n=6) and treated with the empty vehicle MN (EV) made of only cross-linked *m*-HA, the HA MN encapsulating Rosi NPs (10 mg/kg bw) (Rosi), and the CL 316243 NP-loaded MN (1 mg/kg bw) (CL) at inguinal WAT. The MNs could penetrate the mouse skin at the inguinal site efficiently, as evidenced by the trypan blue staining of the MN-treated tissue (Figure 3.3k). It allowed the tips of MN expose

to the inguinal adipose tissue and successfully delivered model drugs into the adipocytes, as evidenced in the fluorescence microscope image (Figure 3.5). *In vivo* fluorescence imaging of the Cy5.5-labeled nondegradable NPs without GOx loaded MNs verified that the NPs were able to be well restricted in the treated skin region during the whole treatment (Figure 3.6). The SEM of the MN revealed the collapsed tips after application, further verifying the complete release of drug (Figure 3.3j). The *in vivo* sustained release within 3 days was also confirmed by *in vivo* fluorescence imaging. Compared to the rapid release of free Cy5.5-loaded MN patch, the degradable NPs-loaded patch showed excellent sustained release capability (Figure 3.7). The mice were treated with MN patches every 3 days. Six days post-treatment, the mice were sacrificed and the inguinal adipose tissues were collected for histological and gene analysis. The hematoxylin and eosin (H&E) staining of inguinal WAT depicted shrinkage of unilocular white adipocytes and appearance of paucilocular adipocytes, the typical morphology of beige adipocyte, in Rosi MN and CL 316243 MN treated groups, particularly the latter (Figure 3.8a). Gene expression analyses further support the browning transformation of the inguinal WAT by MN delivery of browning agents (Figure 3.8b). The representative brown adipocyte genes including *Ucp1*, *Dio2*, *Elovl3*, *Cidea*, *Pgc-1 α* , *Cox7a1*, and *Cox8b*, which are involved in mitochondrial activity and lipid utilization, were up-regulated in both groups, while the inflammatory gene *IL-6* was tended to be down-regulated. Interestingly, pan-adipocyte marker *Adiponectin* was not affected, suggesting a selective regulation on browning. Notably, the canonical PPAR γ target *aP2* was up-regulated by Rosi MN but not CL 316243 MN, buttressing their distinct browning mechanisms.

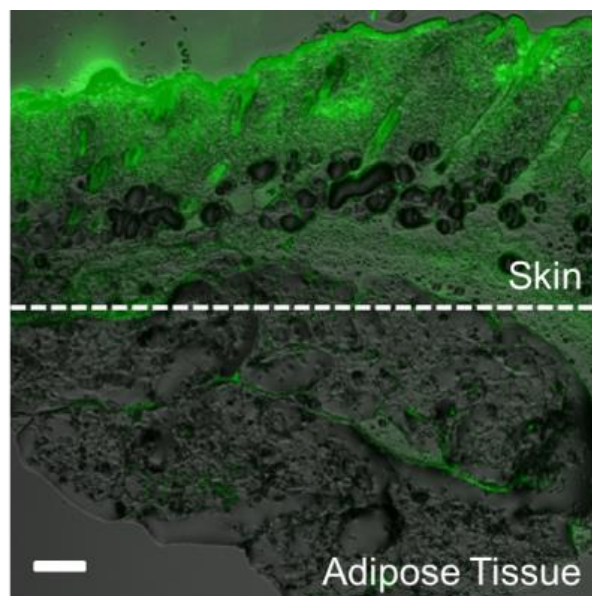


Figure 3.5 Fluorescence microscopy image of inguinal adipose tissue section after treatment of fluorescein isothiocyanate (FITC)-encapsulated NP through the microneedle patch (scale bar: 200 μm).

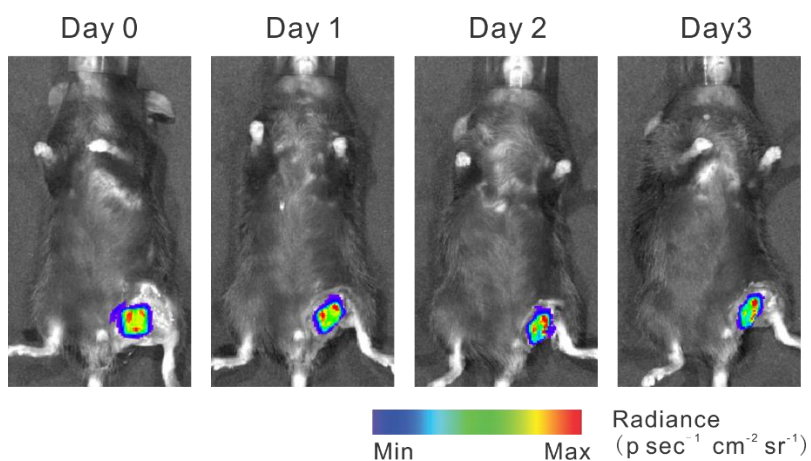


Figure 3.6 *In vivo* fluorescence imaging of the mouse treated with Cy5.5-labelled NPs-loaded MNs at different time points. Cy5.5-labelled non-degradable NPs without glucose specific enzyme were loaded into crosslinked HA MNs.

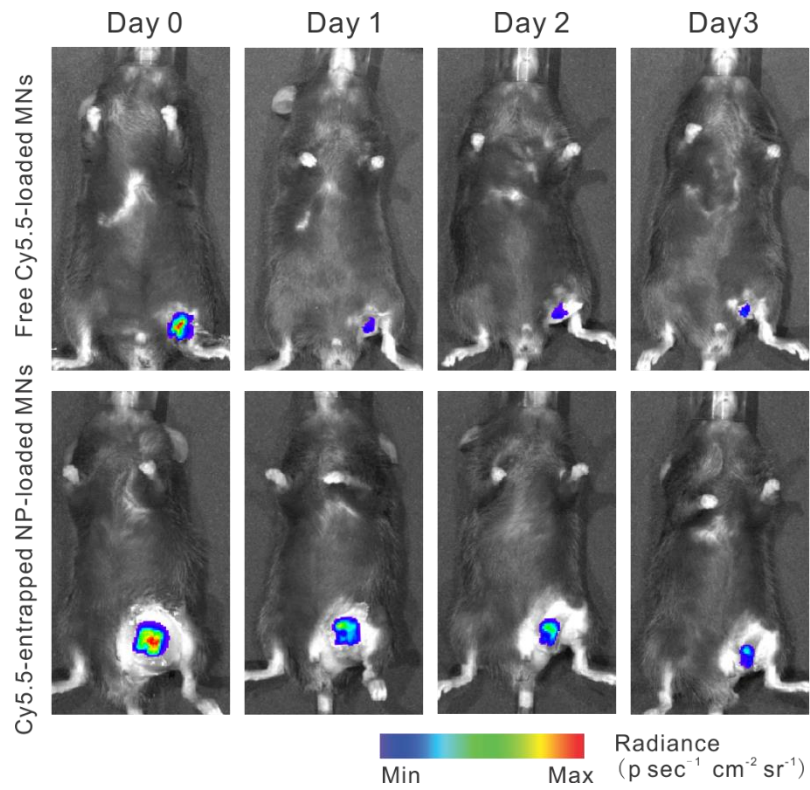


Figure 3.7 *In vivo* fluorescence imaging of the MN-treated mice at different time points. The fluorescent signal showed the MN patch loaded with free Cy5.5 (upper panel) or Cy5.5-entrapped NPs (lower panel).

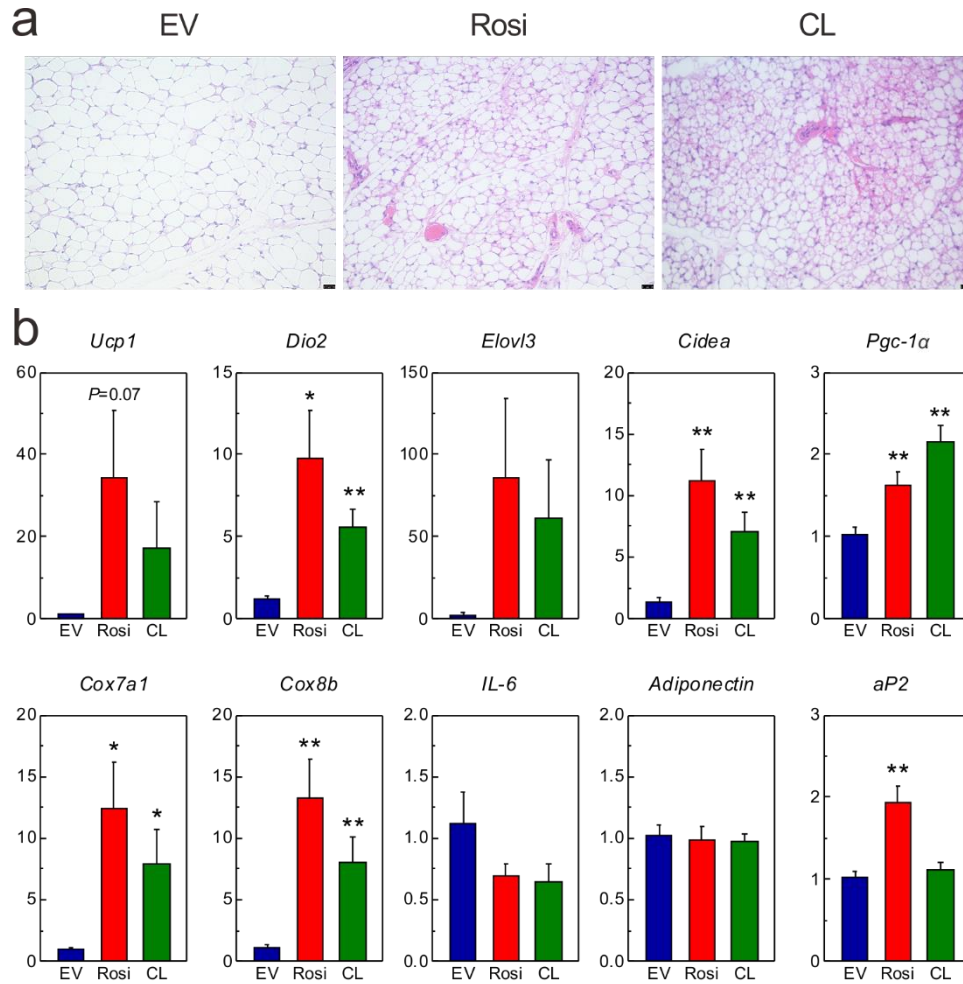


Figure 3.8 *In vivo* browning induction by MN patches in the lean mice. (a) H&E-stained section of the cross-sectional mouse inguinal adipose tissue treated with HA empty MN patch (left), Rosi NP-loaded MN patch (middle), and CL 316243 NP-loaded MN patch (right) (scale bar: 25 μ m). (b) Q-PCR analysis of gene expression in inguinal WAT treated with MN patches loaded with HA empty vehicle (EV), Rosi, or CL 316243 (CL). NP-loaded MN patch. Error bars indicate standard error of the mean (SEM), two-tailed Student's *t*-test, * $P < 0.05$, ** $P < 0.01$ compared to EV (n=6).

After establishing the feasibility of our MN approach to induce browning *in vivo*, we set out to test whether the browning effects of Rosi MN and CL 316243 MN, if genuine, are lasting and physiologically significant. To this end, we exposed Rosi MN- or CL 316243 MN-treated mice together with vehicle MN-treated control mice to indirect calorimetric analysis to measure their systemic metabolic response. All three groups of mice lost weight during the experiment due

to the stress from single-housing, but the CL 316243 MN group tended to lose more (Figure 3.9a).¹¹⁶⁻¹¹⁸ Their higher body weight loss arose from reduced fat mass particularly visceral epididymal WAT (eWAT) (Figure 3.9b, c). The changes in energy homeostasis were merely caused by energy expenditure since neither Rosi MN nor CL 316243 affected calorie intake (Figure 3.9d). Strikingly, both treatments increased oxygen consumption (Figure 3.9e) as an outcome from induced browning (Figure 3.8). Unlike CL 316243 MN, Rosi MN reduced the locomotor activity during the dark cycle when mice are more active (Figure 3.9e), in line with their distinct browning mechanisms. Furthermore, both Rosi and CL 316243 decreased respiration exchange ratio (RER) (Figure 3.9g), reflected by released CO₂/consumed O₂, indicating their preference of fatty acid utilization after browning since only 75% oxygen is needed to fully oxidize carbohydrates compared to fatty acids (3:4 ratio). Taken together, our calorimetric studies completely supported the notion that MN delivery of Rosi or CL 316243 browning reagents is an efficient way to induce browning and improve metabolism.

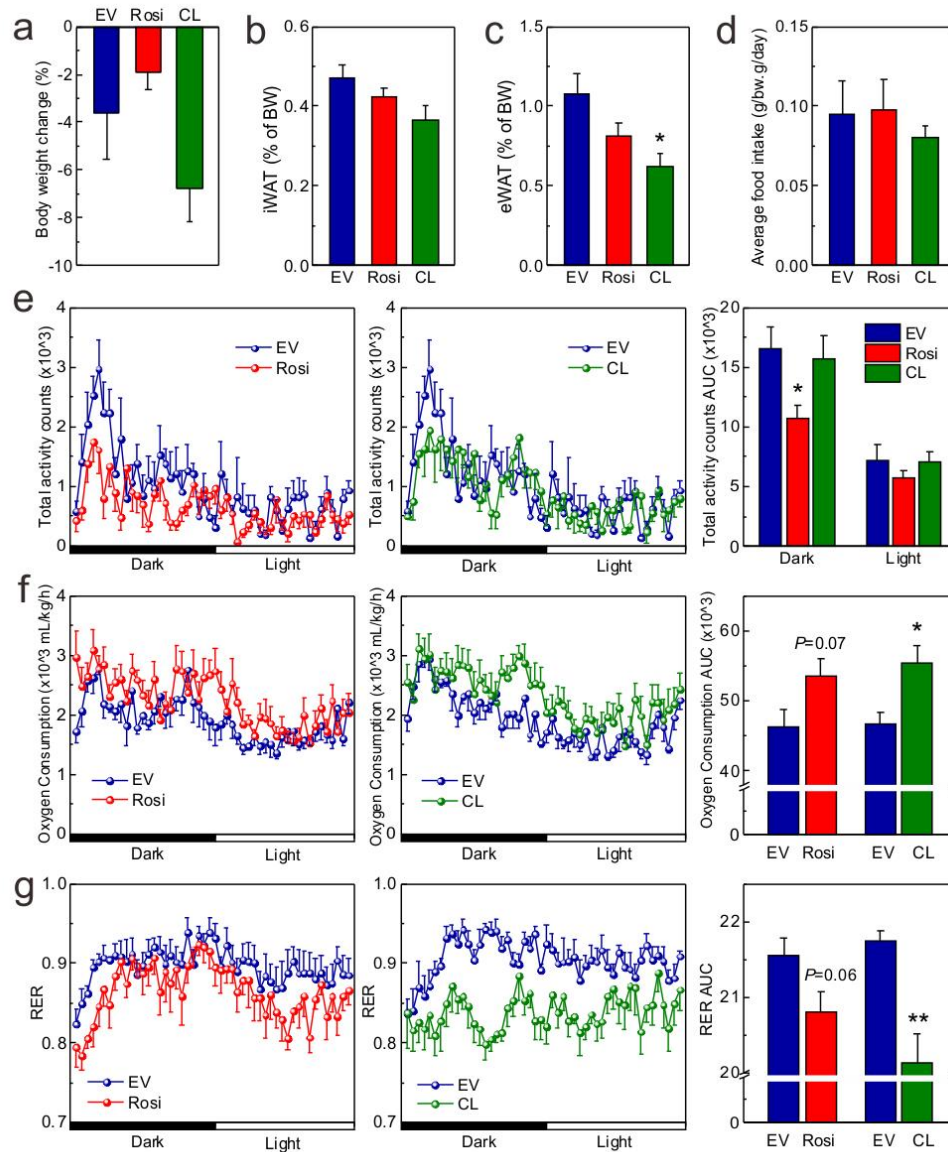


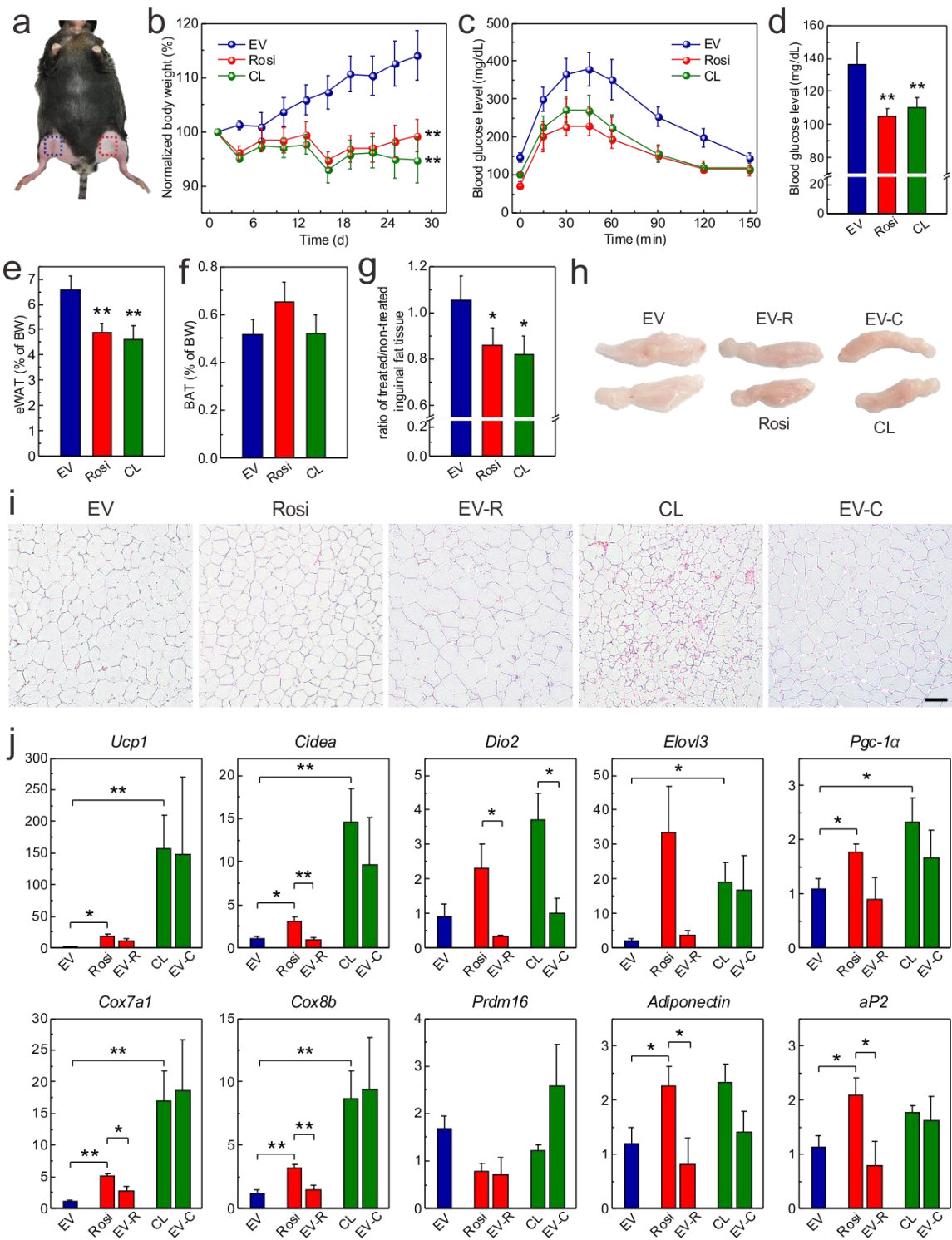
Figure 3.9 Indirect calorimetric analysis of healthy mice treated with HA empty MN patch (EV), Rosi NP-loaded MN patch (Rosi), or CL 316243 NP-loaded MN patch (CL). (a) Body weight change after the 6-day treatment. (b) Normalized inguinal fat pad size. (c) Normalized epididymal fat pad size. (d) Average food intake during the treatment. (e) Locomotor activity during one 24-h dark/light cycle. The panel on the right is the area under curve (AUC). (f) Oxygen consumption and AUC. (g) Respiration exchange ratio (RER) and AUC during one dark/light cycle. Error bars indicate SEM, two-tailed Student's *t*-test, * $P < 0.05$, ** $P < 0.01$ compared to EV ($n=6$).

3.3.4 *In vivo* studies of the MNs on diet-induced obese mice

Encouraged by these striking physiological effects of our MN browning agent patches, we further evaluated their therapeutic potentials in obese mice. In high-fat diet (HFD)-induced obese C57BL/6 mice, we applied the MN browning agent patch to one side inguinal region (Rosi and CL) and the empty HA MN to the other side as vehicle control (EV-R and EV-C) (Figure 3.10a). For the control mice, both sides were treated with empty HA MN (EV). Rosi is a potent insulin sensitizer but also causes weight gain. Surprisingly, MN delivery of Rosi also prevented weight gain as CL 316243 MN did, resulting in a ~15% inhibition at the end of this four-week treatment (Figure 3.10b). Both Rosi MN and CL 316243 MN efficiently improved glucose clearance rate after injecting the mice a bolus of glucose, named intraperitoneal glucose tolerance testing (IPGTT) (Figure 3.10c), and decreased fasting blood glucose levels (the diagnostic indicator of diabetes) from 140 mg/dL in control mice to ~110 mg/dL (Figure 3.10d), indicating an improvement of insulin sensitivity. Intriguingly, this improvement is caused by browning rather than by the insulin sensitizing function of Rosi itself since CL 316243 showed the same effect. As a consequence of increased browning and lipid utilization as we see in Figure 3.9, we observed a ~30% reduction of eWAT (Figure 3.10e) but not in the classic interscapular BAT (Figure 3.10f). More importantly, the MN delivery of browning agents reduced inguinal fat pad locally. The sizes of treated sides, either by Rosi MN or CL 316243 MN, were reduced compared to untreated side (EV-R or EV-C) (Figure 3.10g, h). Supportively, the H&E stained sections revealed apparently smaller adipocytes in inguinal WAT only in the groups administered with drug-containing patches, but no obvious browning observed on the other site that injected with empty patches (Figure 3.10i). Brown adipocyte genes were more highly induced in the treated side, particularly by Rosi MN (Figure 3.10j),

indicating a restricted browning effect of MN patches. As an indicator of improved adipose health, *Adiponectin* was up-regulated in both Rosi MN and CL 316243 MN treated side (Figure 3.10j). Whereas PPAR γ downstream target *aP2* was only induced by MN Rosi (Figure 3.10j), further supporting a local effect of MN patch. Additionally, as presented in the H&E stained histological images of the mouse skin surrounding the MN-treated area after one-month administration, there were insignificant lesions in the skin, indicating excellent biocompatibility of the MN patches (Figure 3.11).

Figure 3.10 *In vivo* antiobesity and antidiabetic effects of MN patches in an HFD-induced obese mouse model. (a) Picture illustrating the mice treated with browning agent patch on one inguinal side (red) and empty vehicle patch on the other side (blue). (b) Normalized body weight of mice without treatment or treated with browning agent patches. (c) IPGTT test in mice 2 weeks post-treatment. (d) Blood glucose levels of mice treated with browning agent patches or empty patches after 16 h fasting. (e) Normalized epididymal fat pad size in mice with different treatments. (f) Normalized weight of interscapular fat pad size in mice with different treatments. (g) Ratio of the treated inguinal fat pad size to untreated side. (h) Photos of two sides of inguinal adipose tissues from obese mice 4-weeks post treatment. (i) H&E staining of inguinal adipose tissues (scale bar: 50 μm). (j) Q-PCR analysis of adipocyte gene expressions in inguinal tissues. (b-g) Error bars indicate SD, two-tailed Student's *t*-test, * $P < 0.05$, ** $P < 0.01$ compared to EV (n=5); (j) Error bars indicate SEM, two-tailed Student's *t*-test, * $P < 0.05$, ** $P < 0.01$ compared to EV (n=5).



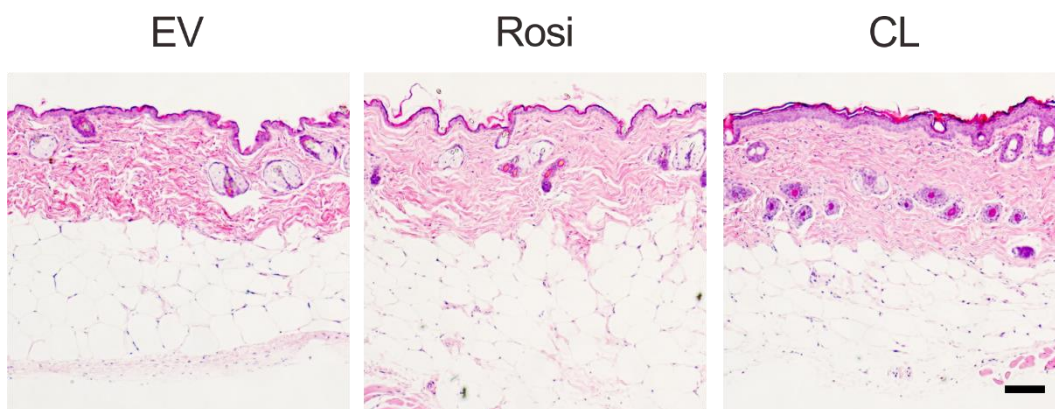


Figure 3.11 H&E-stained skin sections administered empty, Rosi NP-loaded, and CL 316243 NP-loaded MNs (from left to right) with surrounding tissues after one month treatment (scale bar: 100 μ m).

3.4 Conclusion

In conclusion, we developed a technique based on a NPs integrated microneedle patch that enables local browning of WAT. The degradable NPs released browning agents into the subcutaneous region in the presence of glucose and promoted the transformation of WAT toward the brown-like adipose tissue. More importantly, MNs restricted the browning reagents in the treated region and thus are expected to minimize potential side effects of browning reagents on other organs if administered orally or intravenously. Our *in vivo* studies further demonstrated systemically increase of energy expenditure and fatty acid oxidation, effective body weight control in diet-induced obese mice, as well as improved insulin sensitivity. Taken together, our work provides an alternative strategy in applying drugs through MN as potential therapeutics for the clinical treatment of obesity and its comorbidities such as type-2 diabetes.³⁹

CHAPTER 4 ROS-RESPONSIVE MICRONEEDLE PATCH FOR ACNE VULGARIS

TREATMENT

4.1 Introduction

Acne vulgaris, a chronic inflammatory skin disorder, is one of the most prevalent diseases that affects more than 80% of the population worldwide.¹²⁰⁻¹²³ A variety of factors such as genetics, hormones, infections, as well as environmental factors have been identified as the causes of acne development.¹²⁴⁻¹²⁵ Acne usually generates as a result of blockage in the pilosebaceous unit (including hair follicle, hair shaft and sebaceous gland) due to the over-produced sebum by sebaceous gland, which further triggers the excessive proliferation of the bacterium *Propionibacterium acnes* (*P. Acnes*).¹²⁶ *P. acnes* is a Gram-positive anaerobic bacterium that normally presents on the skin, and has been found to have a crucial role in the development of inflammatory acne.¹²⁷⁻¹²⁸ The lipases in *P. acnes* can catalyze the hydrolysis of sebum triglycerides to free fatty acids, which may disrupt follicular epithelium.¹²⁹ Moreover, several chemotactic factors secreted by *P. acnes* also attract the immune cells to the pilosebaceous unit and stimulate the production of proinflammatory cytokines.¹³⁰⁻¹³² Those cellular damage, metabolic byproducts and bacterial debris caused by the rapid growth of *P. acnes* exacerbate the inflammation reaction.^{127, 133} Severely inflamed acne lesions commonly result in hyperpigmentation and permanent skin scarring,¹³⁴ which subsequently cause profound negative psychological and social impact on the quality of life of patients, including stress, embarrassment, and low self-esteem.¹³⁵⁻¹³⁸

Although many antimicrobial agents have been explored for acne treatment such as erythromycin, clindamycin (CDM), and benzoyl peroxide,¹³⁹ there are limited effective and safe administration routes.¹⁴⁰ Most of the anti-acne products are epicutaneous medications;

however, they hardly kill the bacterium effectively due to the poor penetration into dermis.¹⁴¹ Oral antibiotics or isotretinoin show better therapeutic efficacy, while they often pose the risk of harming the intestinal microflora and other side effects such as teratogenicity.¹⁴²⁻¹⁴⁴ In addition, *in vitro* study suggested that *P. acnes* could form a biofilm within follicles, thus enhancing the direct interaction between antibiotics and *P. acnes* is essential to improve the antimicrobial effect.¹⁴⁵ Therefore, alternative formulations with both excellent therapeutic efficacy and negligible adverse side effects are highly desirable.

In this chapter, we took the advantage of skin penetration capability of microneedles (MNs) to improve antibiotics interaction with bacterial for efficient treatment of acne vulgaris (Figure 4.1). In order to achieve on-demand drug release and reduce side effect, the MNs was prepared from a drug-loaded reactive oxygen species (ROS)-responsive poly(vinyl alcohol) (RR-PVA) matrix. The ROS level under pathological conditions can exceed 500 μM in inflammatory tissues,¹⁴⁶ which is much higher than that in normal tissue (1-15 μM).¹⁴⁷⁻¹⁴⁹ Therefore, the ROS-responsive MNs were able to release drug within the *P. acnes*-infected follicle in a sustained manner once penetrating through epidermis,¹⁵⁰ thus enabled effective inhibition of the proliferation of bacteria. Of note, a methacrylated hyaluronic acid (*m*-HA)/diatomaceous earth (DE)-contained base was utilized as the supporting substrate for MNs, which may adsorb pus as well as other purulent exudates and debris for promoted healing, as well as potential prevention of future relapse. A transparent plastic film was further applied to cover the patch as a waterproof, sterile barrier to external contaminants. We have demonstrated that this ROS-responsive MN patch with adsorption capability can effectively deliver antimicrobial therapeutic into dermis to eliminate *P. acnes* in a simple manner.

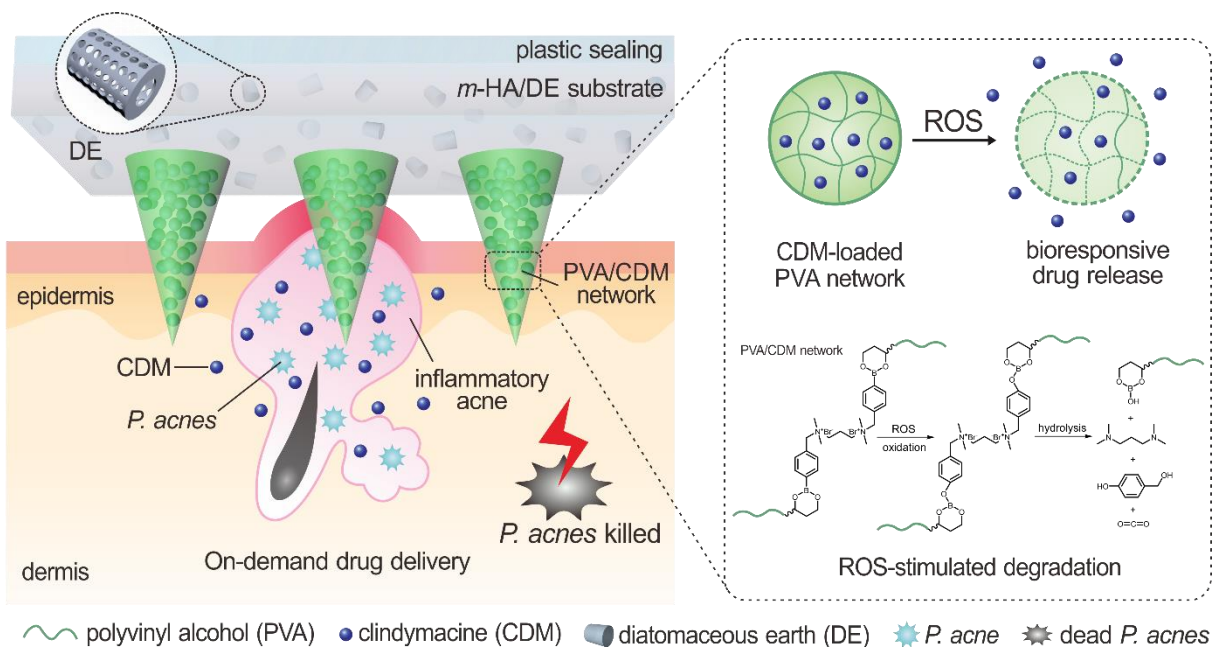


Figure 4.1 Schematic illustration of the formation and mechanism of a ROS-responsive microneedle patch for acne vulgaris treatment.

4.2 Experimental Section

4.2.1 Materials

All chemicals were purchased from Sigma-Aldrich unless otherwise specified and were used as received. The deionized water was prepared by a Millipore NanoPure purification system (resistivity higher than $18.2 \text{ M}\Omega \text{ cm}^{-1}$).

4.2.2 Synthesis of ROS-responsive crosslinker (TSPBA)

4-(Bromomethyl) phenylboronic acid (1 g, 4.6 mmol) and *N, N, N', N'*-tetramethyl-1,3-propanediamine (0.2 g, 1.5 mmol) were dissolved in DMF (40 mL) and the solution was stirred at $60 \text{ }^\circ\text{C}$ for 24 h. Afterward, the mixture was poured into THF (100 mL), filtrated, and washed by THF ($3 \times 20 \text{ mL}$). After dried under vacuum overnight, pure TSPBA (0.6 g, yield 70%) was

obtained. ¹H-NMR (300 MHz, D₂O, δ): 7.677 (d, 4H), 7.395 (d, 4H), 4.409 (s, 4H), 3.232 (t, 4H), 2.936 (s, 6H), 2.81 (m, 2H).

4.2.3 Preparation of RR-PVA hydrogels

PVA (MW: 72 kDa, 98% hydrolyzed) were dissolved in deionized (DI) water to obtain 10 wt% clear PVA solution. The RR-PVA hydrogel were formed instantly by mixing PVA and TSPBA (5 wt% in H₂O) together at a ratio of 3:1. Predetermined amount of drug or dye was added to the PVA aqueous solution to prepare drug/dye-loaded hydrogel.

4.2.4 Preparation of NR-PVA hydrogels

Non-responsive (NR) PVA network was prepared by crosslinking methacrylated PVA (*m*-PVA) with *N, N'*--methylenebis(acrylamide) (MBA) at a ratio of 3:1 in the presence of photoinitiator (Irgacure 2959) under ultraviolet (UV) light. *m*-PVA was synthesized following the previous reported method.¹⁵¹

4.2.5 *In vitro* release profiles

The *in vitro* release profiles of CDM from RR-PVA gel were evaluated through incubation of the hydrogel in 12 mL PBS buffer (NaCl, 137 mM; KCl, 2.7 mM; Na₂HPO₄, 10 mM; KH₂PO₄, 2 mM; pH 7.4) at 37°C on an orbital shaker, to which H₂O₂ was added to reach 1 mM concentration. At predetermined time points, the concentrations of CDM in the supernatant were determined by HPLC. Samples were analyzed at 205 nm by high pressure liquid chromatography on a Zorbax Eclipse Plus RRHD C18 column (2.1 × 50 mm, 1.8 μm particle size) (Agilent, USA) using an isocratic mobile phase consisting of 80% water (HPLC grade

with 0.1% v/v trifluoroacetic acid) and 20% acetonitrile (HPLC grade with 0.1% v/v trifluoroacetic acid). The cumulative release (%) is expressed as the percent of total drug released over time.

4.2.6 *In vitro* antibacterial effect

P. acnes (ATCC 6919) (American Type Culture Collection, Manassas, VA) were cultured on reinforced clostridial medium (RCM) at 37 °C in an anaerobic environment. The stock culture of *P. acnes* was transferred to RCM broth and incubated anaerobically at 37 °C overnight. The cultures were later used to prepare bacterial suspensions (2×10^8 colony forming units (CFUs)/mL). The antimicrobial efficiency against *P. acnes* was determined by incubating *P. acnes* with the incubation medium with RR-PVA gel in the absence of H₂O₂, CDM solution (5 µg/mL), or the incubation medium with RR-PVA gel in the presence of H₂O₂ for 5 h, while *P. acnes* in PBS was used as a negative control. Following incubation, the samples were diluted 1:10³ in PBS, and 10 µL of each sample was spotted on RCM agar plates. The samples were incubated at 37 °C under an anaerobic condition for another 72 h. The CFU of *P. acnes* was quantified.

4.2.7 Fabrication of ROS-responsive (RR) microneedle patch

All the MN patches in this study were prepared using the uniform silicone molds from Blueacre Technology Ltd. There are 11 × 11 needle array in the mold, where each needle has a height of 600 µm and a round base of 300 µm in diameter. The space from tip-to-tip is 600 µm. First, the PVA MNs were formed pipetting premixed PVA (3 wt%)/ TSPBA (3 wt%) (ratio 3:1) solution (400 µL) onto the MN mold surface. The molds were kept under vacuum (600 mmHg)

for 30 min to allow the solution deposit into the MN cavities. Afterwards, the covered mold was centrifuged for 20 min at 500 rpm using a Hettich Universal 32R centrifuge to condense the PVA network in the MNs. Drug-loaded MNs were fabricated by adding predetermined amount of drug in PVA/TSPBA solution at the first step. The non-responsive (NR) microneedle were prepared by changing the MN solution to a mixed solution consisting of *m*-PVA (3 wt%), MBA (1 wt%), and photoinitiator (Irgacure 2959, 0.5 wt%). For CDM MN, 4 wt% HA containing CDM were used to form the MNs for fast release of drug. Then the base of the patch was formed by adding 3 mL *m*-HA solution (4 wt%) containing diatomaceous earth (DE) (0.4 wt%), MBA (0.2%) and 2959 (0.1 wt%) into the prepared micromold reservoir and drying at room temperature under vacuum desiccator for 3 days. *m*-HA was synthesized following the previous reported method.¹⁵² After completely desiccation, the MN patch was carefully detached from the silicone mold and stored in a sealed six well container for later study. Finally, a plastic film (3M Tegaderm, USA) was sealed on top of MN patch during *in vivo* administration. The morphology of the MNs was characterized *via* a FEI Verios 460L field-emission scanning electron microscope.

4.2.8 Microneedle mechanical strength test

The mechanical strength of MN was determined by pressing MNs against a stainless steel plate at a speed of 1 $\mu\text{m/s}$ on an MTS 30G tensile testing machine. The failure force of the microneedle was recorded as the force at which the needle began to buckle.

4.2.9 Oil adsorption capacity test of diatomaceous earth (DE)

The oil adsorption capacity of DE was determined by mixing free acid solution with 1 g DE until no more free acid can be adsorbed at room temperature. The ratio of the weight of free acid and DE was calculated.

4.2.10 *In vivo* acne treatment efficacy evaluation

Eight-week old male Balb/c nude mice ordered from Qinglongshan Animal Center (Nanjing, China) were used. To examine the bactericidal effect of MN patches, *P. acnes* (2×10^6 CFUs/mL) was intradermally injected into back skin of the mouse to establish the acne vulgaris animal model. All animal studies were approved by the Institutional Animal Care and Use Committee (IACUC) of University of North Carolina at Chapel Hill and North Carolina State University, or by the Model Animal Research Center (MARC) of Nanjing University. Mice were divided into seven groups with seven mice in each group. Six-group of mice were induced by *P. acnes* injection, and treated with different formulations for six days: CDM cream (1% v/v CDM in 4% v/v HA solution), RR-MN patches, blank MN patches, CDM MN patches, NR-MN patches (CDM dosage: 0.4 mg/patch). The swelling volumes of the acne were measured using a micro-caliper every day during the treatment period.

4.2.11 Histological analysis of infected skin

The skin tissue samples were excised from the mice 6 days after treatment and were fixed in 10% formalin for 18 h. Then, the tissues were embedded in paraffin, cut into 50 μ m sections, and stained using hematoxylin and eosin (H&E) for histological analysis.

4.2.12 Statistical analysis

All results were presented as Mean \pm SD. Statistical analysis was performed using Student's *t*-test or one-way ANOVA. With a *p* value < 0.05 , the differences between experimental groups and control groups were considered statistically significant.

4.3 Results and Discussion

4.3.1 Preparation and characterization of ROS-responsive gel

ROS-responsive gel was first prepared by crosslinking PVA using a dual phenylboronic acid contained linker (Figure 4.2), which can be cleavable by ROS through oxidation and further hydrolysis.¹⁵³ To substantiate the responsiveness of the crosslinker, RR-PVA tough gel was incubated in 1 mM H₂O₂ contained phosphate buffered saline (PBS) buffer (pH 7.4) at 37 °C. Rapid degradation of the RR-PVA hydrogel was observed due to the oxidation of the crosslinkers (Figure 4.3a), while the nonresponsive (NR) PVA gel without the ROS-sensitive linker was stable in the presence of H₂O₂ (Figure 4.4). On the other hand, there was no obvious change in morphology or size of the RR-PVA gel in the buffer without H₂O₂, indicating the high stability of the RR-PVA matrix. CDM, a common antibiotic for acne treatment,¹⁵⁴ was entrapped into RR-PVA matrix for *P. acnes* elimination. When incubating with the PBS solution containing 1 mM H₂O₂, the ROS-triggered sustained drug release was also detected from the RR-PVA/CDM gel (Figure 4.3b). In addition, the RR-PVA gel showed faster degradation and drug release rate under a higher H₂O₂ concentration at 10 mM, further confirming the ROS-dependent degradation of the RR-PVA gel (Figure 4.5 and 4.6).

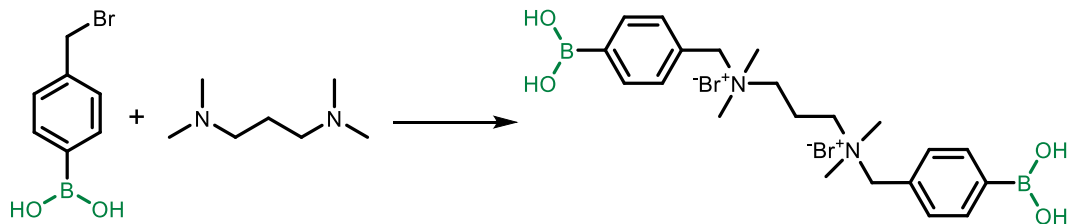


Figure 4.2 Synthesis route of ROS-responsive linker TSPBA.

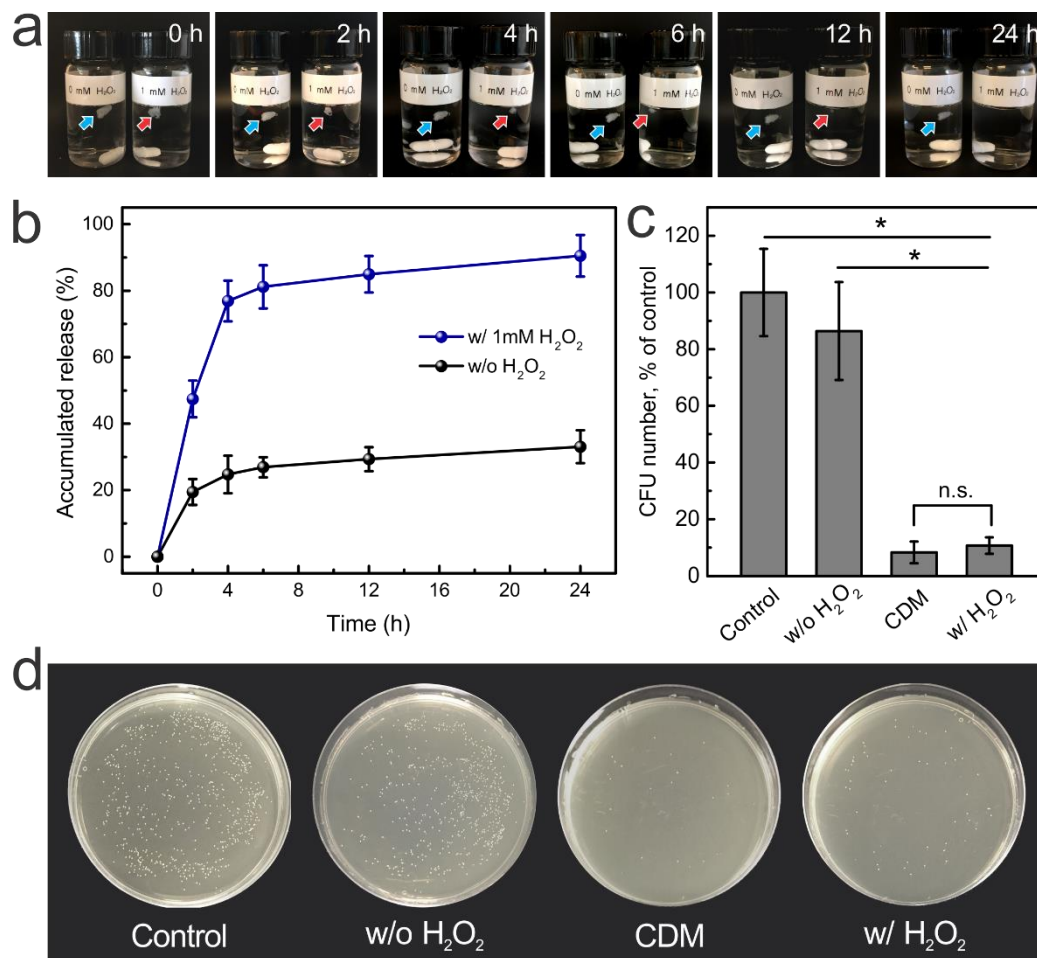


Figure 4.3 *In vitro* responsiveness and antibacterial effect of the RR-PVA gel. a) Degradation of RR-PVA gel in the PBS solution with 1 mM H₂O₂ or without H₂O₂. b) Accumulated release profile of CDM from RR-PVA gel with or without H₂O₂. c) Quantitative analysis of colony-forming units (CFUs) in each group. d) *P. acne* suspension cultured on RCM agar plate for 72 h, with addition of PBS buffer, the incubation medium with RR-PVA gel in the absence of H₂O₂, free CDM solution and the incubation medium with RR-PVA gel in the presence of H₂O₂. Error bars indicate s.d. (n = 3), two-tailed Student's *t*-test, * *P* < 0.05.

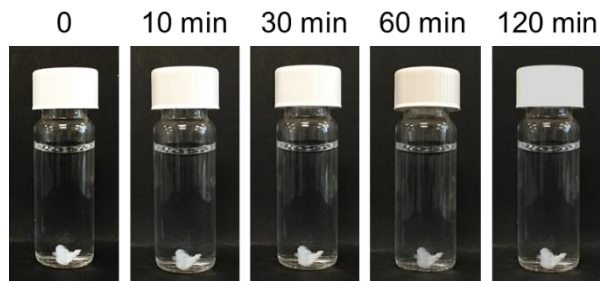


Figure 4.4 Incubation of NR-PVA gel in PBS buffer with 10 mM H₂O₂ at 37 °C.

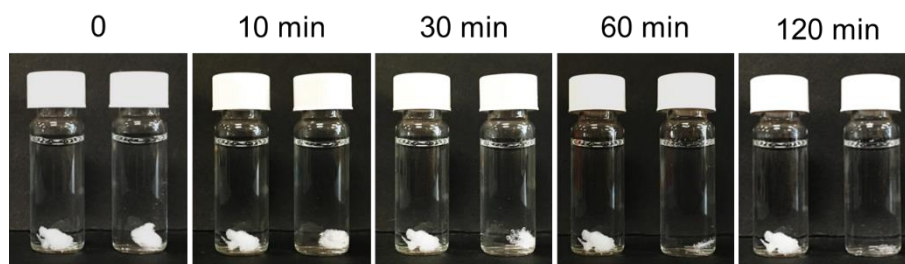


Figure 4.5 Degradation of RR-PVA gel in PBS solution with 10 mM H₂O₂ at 37 °C.

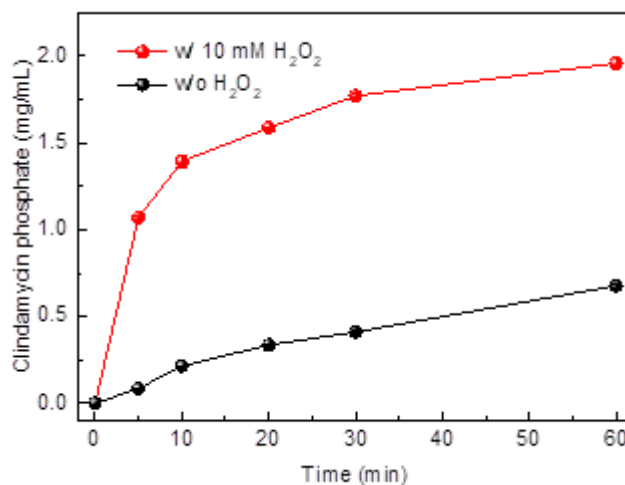


Figure 4.6 Accumulated release of CDM from RR-PVA gel in the presence of 10 mM H₂O₂.

4.3.2 *In vitro* antibacterial effect evaluation

Next, *in vitro* antibacterial effect was evaluated by culturing *P. acnes* with the media incubating RR-PVA/CDM gel (Figure 4.3c and d). The H₂O₂-contained incubation media with RR-PVA/CDM gel displayed significant inhibitory effect on bacterial growth compared with the

control group treated with PBS solution. In contrast, the incubation media without H₂O₂ showed insignificant effect on the growth of bacterial since the limited drug diffusion from RR-PVA/CDM gel in the absence of H₂O₂. Collectively, these results demonstrated that the drug release from RR-PVA was in a ROS-mediated manner, which could achieve an on-demand treatment effect for inflammatory acne therapy.

4.3.3 Fabrication and characterization of drug-loaded MN-array patch

For further efficient drug delivery into acne underneath the skin,^{1, 150} a MN-array patch was fabricated through a micromolding method.²⁰ Briefly, the drug containing responsive MNs were first formed by depositing diluted PVA/CDM solution with ROS-responsive crosslinker into the tip region of a silicone micro-scale mold under a vacuum condition and then condensing by centrifugation. As shown in the SEM image, each MN was of a conical shape, with a base diameter of 300 μm and a height of 600 μm (Figure 4.7a). The mechanical strength of each MN was determined as 2.2 N (Figure 4.7e), which sufficiently enables skin penetration without breaking.^{38, 152, 155} Afterward, a layer of *m*-HA/DE matrix was integrated as the supporting substrate. HA was chosen considering its excellent biocompatibility and biodegradability,⁶¹ and DE was additionally doped for its physical adsorption property.¹⁵⁶ DE, typically consists of 87-91% silicon dioxide,¹⁵⁷ has been widely applied as absorbent because of its porous structure (Figure 4.8).¹⁵⁸⁻¹⁶¹ It turned out to have ~95% oil adsorption capability, which was 3-fold higher than the activated carbon (~32%) (Figure 4.9).¹⁶² The adsorption capability of small molecule such as fluorescent dye was also demonstrated (Figure 4.10 and 4.11). Therefore, the DE could be useful to adsorb pus and purulent exudates in acne. The fluorescence image in Figure 3b displayed a cross-sectional view of the MN patch with rhodamine-labeled PVA needle tips and a fluorescein-labeled HA base. The obtained device

was arranged in an 11×11 array with an interval of $600 \mu\text{m}$ from tip to tip on a $7 \times 7 \text{ mm}^2$ patch (Figure 4.7c). Additionally, the patch can also be applied on a cotton swab for an alternative temporary administration method (Figure 4.7d).

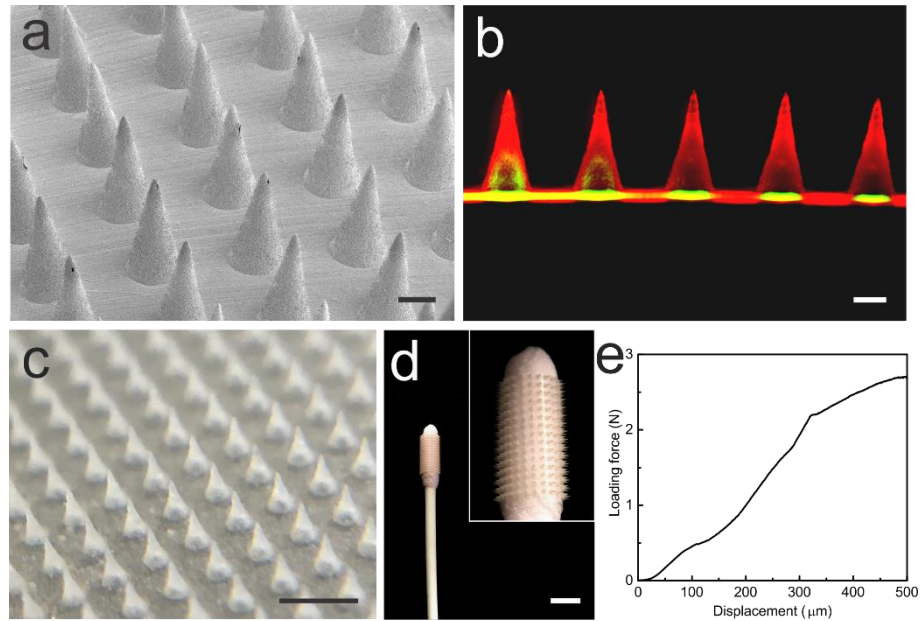


Figure 4.7 Fabrication and characterization of the RR-MN array patch. a) An SEM image of the MN array. Scale bar: $200 \mu\text{m}$. b) A fluorescence microscopy image showing rhodamine-labeled PVA MN and FITC-labeled HA base. Scale bar: $200 \mu\text{m}$. c) A photograph of the MN patch. Scale bar: 1 mm . d) Photos showing the MN patch wrapped on a cotton stick for temporary usage. Scale bar: 10 mm . e) Mechanical strength of one MN.

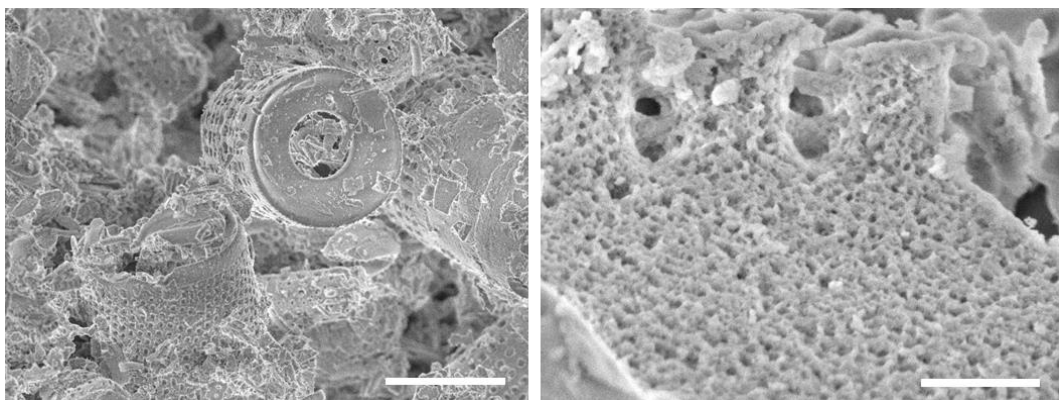


Figure 4.8 SEM images of DE showing its porous structure. Scale bars: $10 \mu\text{m}$ (left), 500 nm (right).

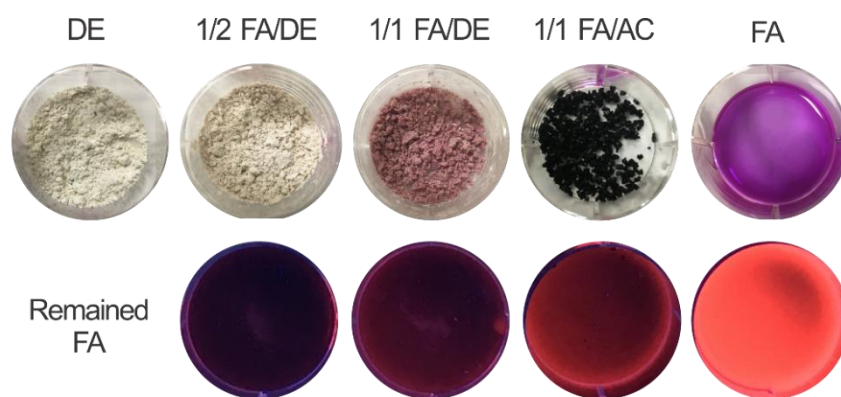


Figure 4.9 Oil adsorption test of DE. The upper row presents DE or activated carbon (AC) adsorption of Nile red (NR) containing fatty acids (FA) with different weight ratios. The bottom row shows remained FA/NR under UV light.



Figure 4.10 Adsorption capability of small molecular dye by DE. a) Adsorption of Rhodamine B (RhB) by different amount of DE in aqueous solution. b) Quantitative analysis of remained RhB in figure S7a.

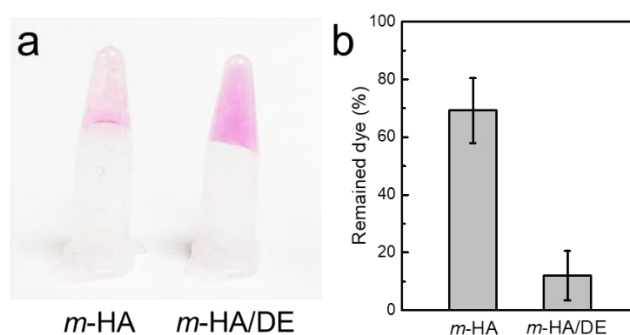


Figure 4.11 Adsorption of RhB by *m*-HA or *m*-HA/DE film with incubation in RhB containing PBS solution at 37°C for 30 min. a) A photo showing the *m*-HA and *m*-HA/DE films after incubation in RhB solution. b) Quantitative analysis of remained RhB in solution after adsorption by the *m*-HA and *m*-HA/DE films.

4.3.4 *In vivo* antibacterial studies on an acne-mouse model

The *in vivo* antibacterial performance of MN patches was investigated in a *P. acnes*-induced inflammation mouse model. The Balb/c nude mice were randomly divided into seven groups (n=7), with six groups infected by *P. acnes* via intradermal injection into the skin on the back, and one group injected with PBS solution as a positive control group (labeled as normal). No swelling was detected in the PBS-injected mice, while a considerable volume raise was observed 1 day after *P. acnes* infection.

Then the *P. acnes*-infected mice were treated with different formulations to evaluate the treatment efficiency. One group was chosen as negative control without treatment (control), another one group was administered with 1 wt% CDM cream, and other four groups were respectively administered with ROS-responsive PVA/CDM microneedle patches (RR-MN), CDM loading HA microneedle patches (CDM MN), nonresponsive PVA/CDM microneedle patches (NR-MN), and blank microneedle patches without CDM (blank MN) (CDM dose: 0.4 mg per mouse). The volume size of the swollen skin was monitored every day during the treatment (Figure 4.12a and b). Without treatment, the skin of mice in control group continued to swell up to day 4. In contrast, the skin treated with RR-MN remarkably shrank its size ~90% after administration and part of the swell even started to disappear on day 5, suggesting the effective inhibitory effect of acne growth by RR-MN. However, the group applied with CDM cream barely decreased the size of the swollen skin, neither did the groups administered with blank MN or NR-MN. The slight skin size reduction caused by blank MN or NR-MN may be attributed to the physical adsorption of pus and cell debris by the patches through the microchannels generated by MNs. Although the CDM MN delivered drugs into the infected

skin, there was no significant inhibition of the acne growth, which is due to the fast release and clearance of the drug. On the contrary, the RR-MN allowed a sustained antibiotic release within the acne area and resulted in the enhanced bactericidal effect (Figure 4.13).

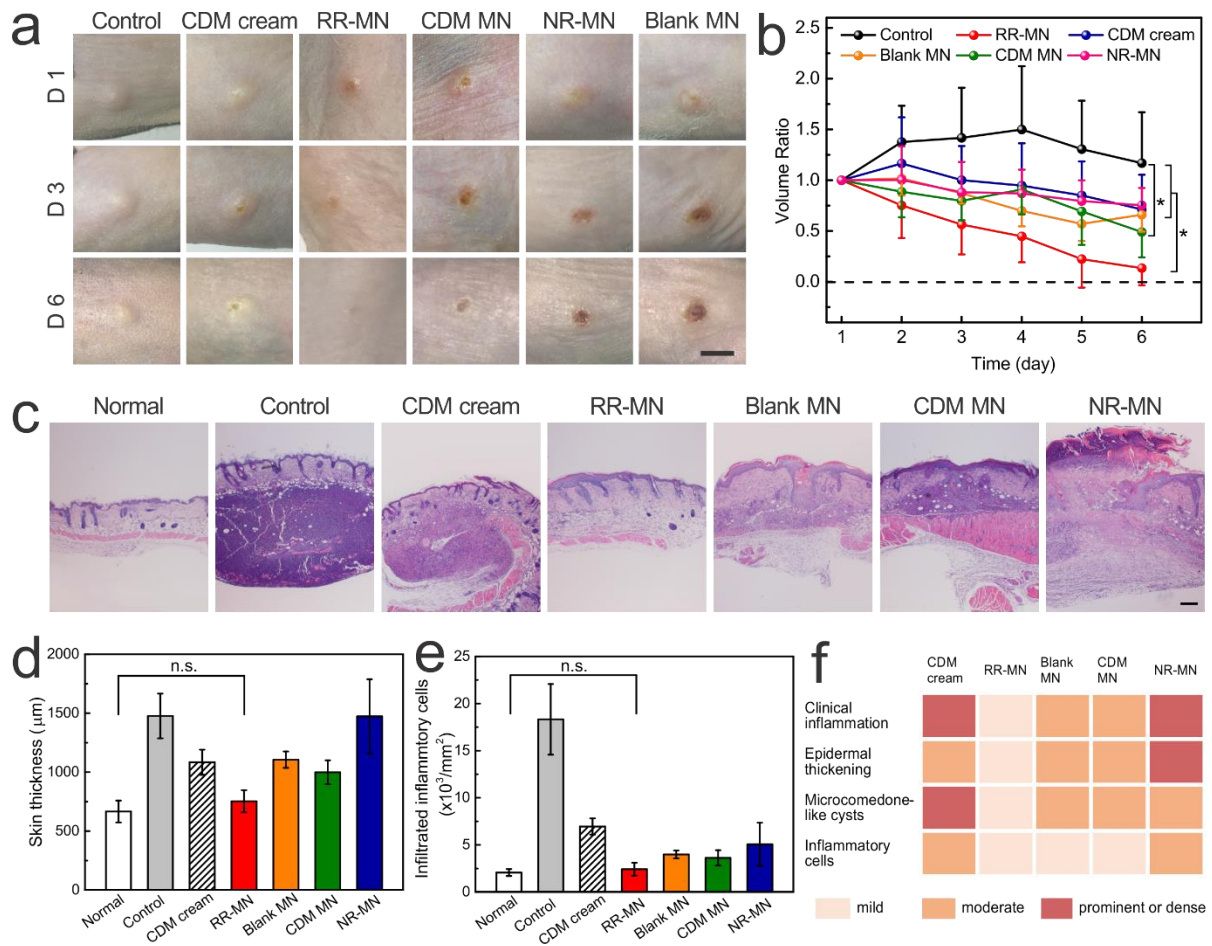


Figure 4.12 *In vivo* treatment of acne using different MN array patches. a) Images showing the dramatic decrease in swelling volume of the RR-MN treated back skin of *P. acnes*-induced mice after 6-day treatment. Scale bar: 5mm. b) Comparison of swelling volume size in the back skins of *P. acnes*-induced mice during the treatment period. Statistical significance was calculated by one-way ANOVA, * $P < 0.05$. c) Histological analysis of skin tissues obtained from normal mice, *P. acnes*-induced mice, and *P. acnes*-induced mice treated with CDM cream, RR-MN, blank MN, CDM MN and NR-MN. Scale bar: 200 μm . d) Quantitative analysis of thickness of skin from mice in each group. e) Quantitative analysis of infiltrated inflammation cells in each group. f) Semiquantitative summary of the histological analysis results with a 3-point scale. Error bars indicate s.d. (n = 7).

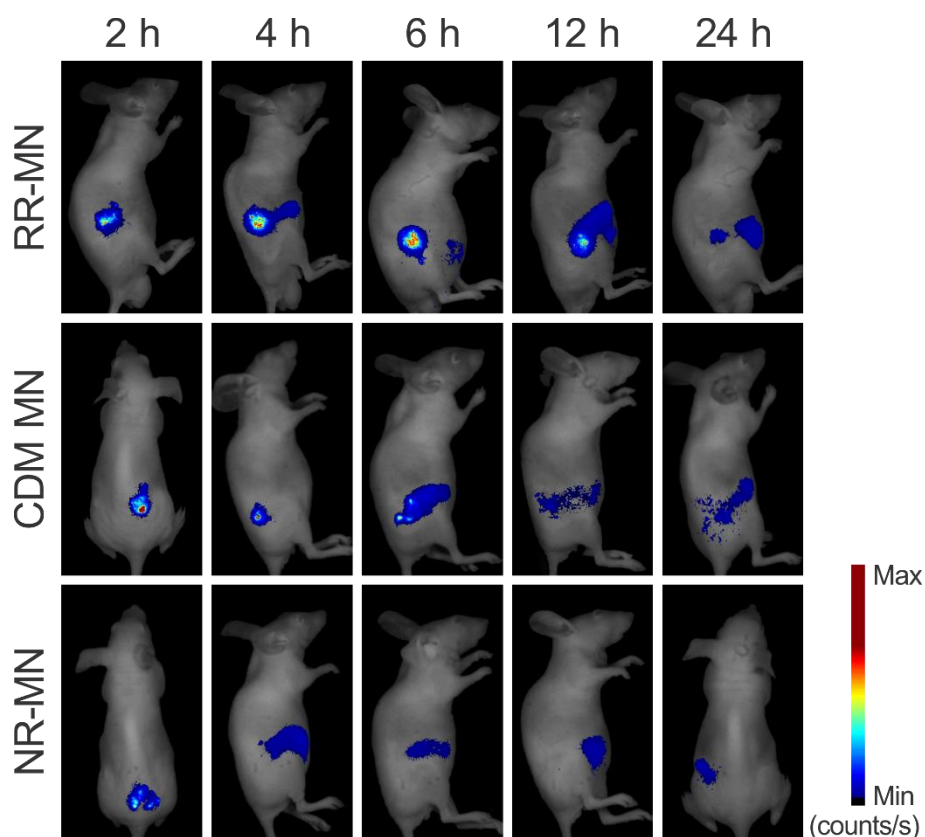


Figure 4.13 *In vivo* fluorescence whole body imaging showing the release of Cy5.5 from RR-MN, CDM MN and NR-MN in acne area.

After a period of 6 day treatment, the mice were sacrificed and the skin tissues with the acne were excised for histological analysis (Figure 4.12c). Consistent with the acne growth curve, the clinical inflammatory lesions were significantly improved in the skin tissues treated with RR-MN, comparing to other treated groups as shown in the hemotoxylin and eosin (H&E) staining images. The number of the microcomedone-like cysts in the upper dermis above the focus of inflammation in the RR-MN-treated group also decreased to an extent similar to that in the normal skin tissues. The quantitative measurement of skin thickness demonstrated there was no significant difference between the skin applied with RR-MN and the normal skin thickness (Figure 4.12d), validating the efficacy of the RR-MN. In addition, the number of

infiltrated inflammatory cells into the dermis also dramatically decreased in the skin administered with RR-MN patches compared to that in *P. acnes*-induced skin without treatment (Figure 4.12e). Nevertheless, CDM cream did not effectively inhibit the skin thickening or inflammation in comparison with RR-MN-treated groups, implying insufficient drug penetration into the dermis. These results strongly indicated that transdermal administration of the RR-MN patch effectively suppressed *P. acnes*-induced inflammatory (Figure 4.12f), without causing noticeable side effects in the surrounding skin tissue.

4.4 Conclusion

In conclusion, we have generated a ROS-responsive MN patch to effectively deliver antibiotic into dermis for enhancing acne treatment. Unlike the traditional anti-acne cream, the drug-loaded MNs are able to penetrate stratum corneum to improve the drug interaction against *P. acnes*. Meanwhile, the inflammation-mediated sustained drug release continuously keeps a sufficient drug concentration in the therapeutic levels around acne area. An HA/DE contained substrate of the patch can also absorb the pus and dead cell debris to accelerate the healing of skin. This biosignal-responsive MN patch-based strategy can also be extended to enhance the therapeutic efficiency for the treatment of various other skin diseases.³⁹207

CHAPTER 5 BIORESPONSIVE MICRONEEDLE WITH A SHEATH STRUCTURE FOR H₂O₂ AND pH CASCADE-TRIGGERED INSULIN DELIVERY

5.1 Introduction

Diabetes mellitus is a global burden affecting 422 million people in 2016.¹⁶³ It is characterized by a deficit of endogenously-produced insulin and thereafter elevated blood glucose levels (BGLs).^{29, 164} Open-loop subcutaneous injection of insulin cannot regulate BGLs tightly and is associated with a risk of severe hypoglycemia.¹⁶⁵⁻¹⁶⁶ Thus, a closed-loop system that can “secret” desirable amounts of insulin in response to hyperglycemia while maintaining basal insulin release kinetics under normoglycemia is urgently needed. Electronic closed-loop devices that have been developed to this end remain challenges associated with algorithm accuracy and sensor reliability.¹⁶⁷⁻¹⁶⁸ Alternatively, chemically-engineered formulations or devices with the assistance of glucose oxidase (GOx),^{20, 104, 169-174} phenylboronic acid (PBA)¹⁷⁵⁻¹⁸¹ and glucose binding protein¹⁸²⁻¹⁸⁷ have attracted increasing attention.^{107, 188-191} For example, GOx catalyzes the oxidation of glucose to gluconic acid in the presence of oxygen and generates hydrogen peroxide (H₂O₂).¹⁹² Accordingly, GOx-mediated enzymatic reaction can create a local oxidative and acidic environment triggered by elevated glucose levels to promote the release of insulin preloaded in acid-responsive systems.³² However, the typical pH change-triggered response of materials is often accompanied by slow changes in conformation and morphology of materials and formulations under a physiological condition.^{31, 171} In addition, the *in vivo* release of GOx from medical devices may cause potential toxicity,¹⁹³ as well as the concerns over long-term biocompatibility of the H₂O₂ generated during oxidation of glucose.¹⁹⁴ Therefore, the ongoing development of smart insulin delivery systems is focused

on achieving several merits, including rapid responsiveness, ease of preparation and administration as well as excellent biocompatibility.^{39, 119, 195}

In this chapter, we describe a new glucose-responsive microneedle (MN) array patch¹⁹⁶⁻¹⁹⁷ for self-regulated insulin delivery, utilizing H₂O₂ and pH cascade-responsive NCs. Briefly, insulin was first entrapped into degradable complex micelles (designated Ins-NCs); while GOx was encapsulated into nondegradable complex micelles (designated GOx-NCs) *via* crosslinking with uncleavable bonds (Figure 5.1a). Both Ins-NCs and GOx-NCs were then loaded into the crosslinked gel core matrix of microneedle. Under a hyperglycemic condition, the Ins-NCs could respond to H₂O₂ and gluconic acid generated by the GOx-catalyzed oxidation of glucose and be dissociated to promote insulin release because of the disruption of micelle structure as well as charge reductions of polymer (positive charge) and insulin (negative charge) (Figure 5.1a-b). Inspired by the protection function against oxidation in the peroxisome,¹⁹⁸ catalase nanogel (CAT-NG)^{104, 170} was embedded into the crosslinked-poly(vinyl alcohol) (PVA) sheath structure, covering the surface of the microneedle core matrix (Figure 5.1c), to mitigate the injury of H₂O₂ generated in the core part toward normal tissues (Figure 5.2). After painless administration of MN patch, Ins-NCs could be decomposed when MN was exposed to elevated interstitial fluid glucose under a hyperglycemic state, thereby rapidly releasing insulin to capillary vessels and consequently restoring homeostasis.

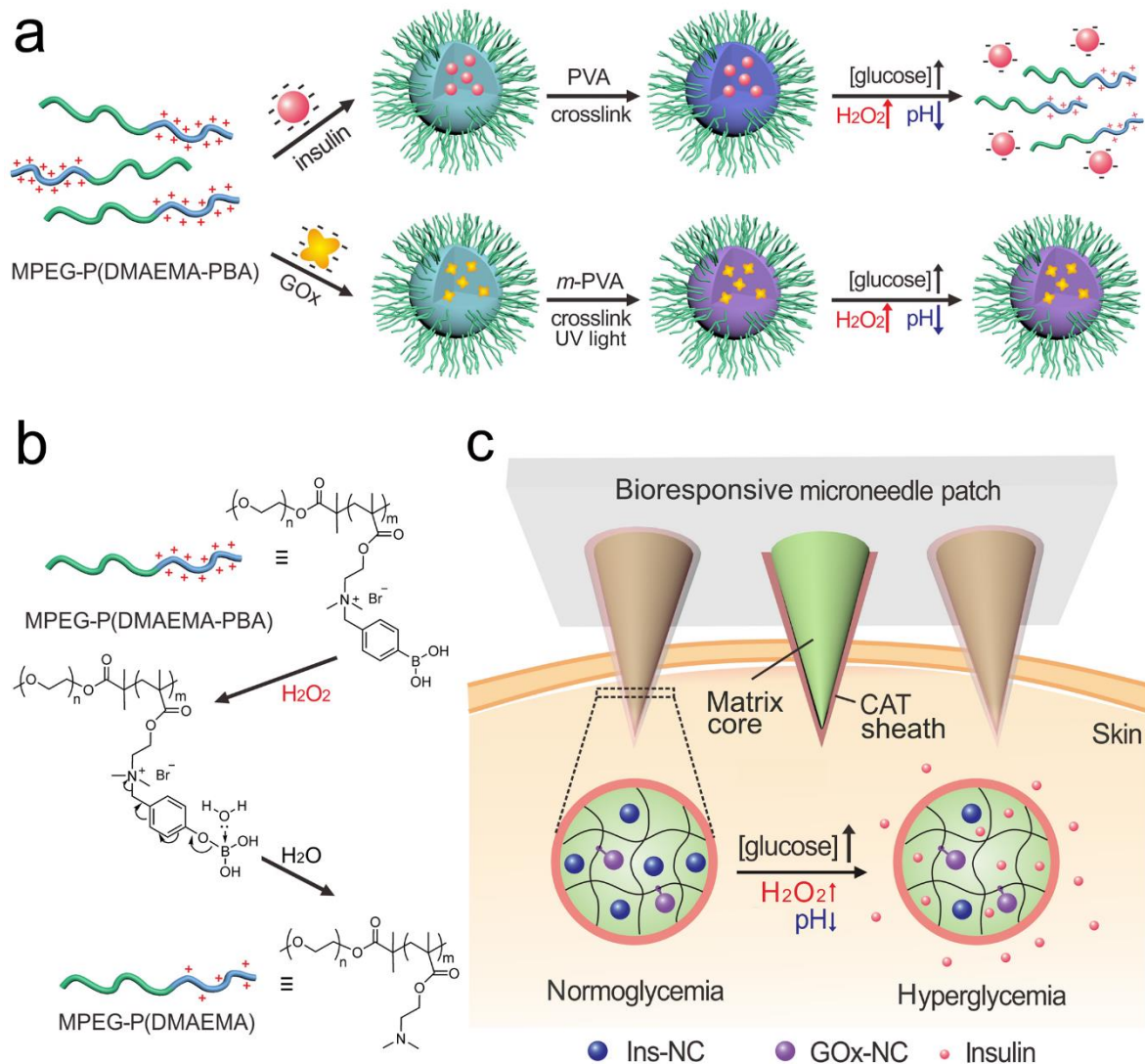


Figure 5.1 Schematic of the glucose-responsive insulin delivery system utilizing H_2O_2 and pH cascade-responsive NC-loading MN-array patch. (a) Formation of Ins-NCs and GOx-NCs and mechanism of glucose-responsive insulin release. (b) Schematic of H_2O_2 -triggered charge reduction of the polymer. (c) Schematic of the NC-containing MN-array patch with a CAT sheath structure for *in vivo* insulin delivery. Insulin release is triggered under a hyperglycemic state.

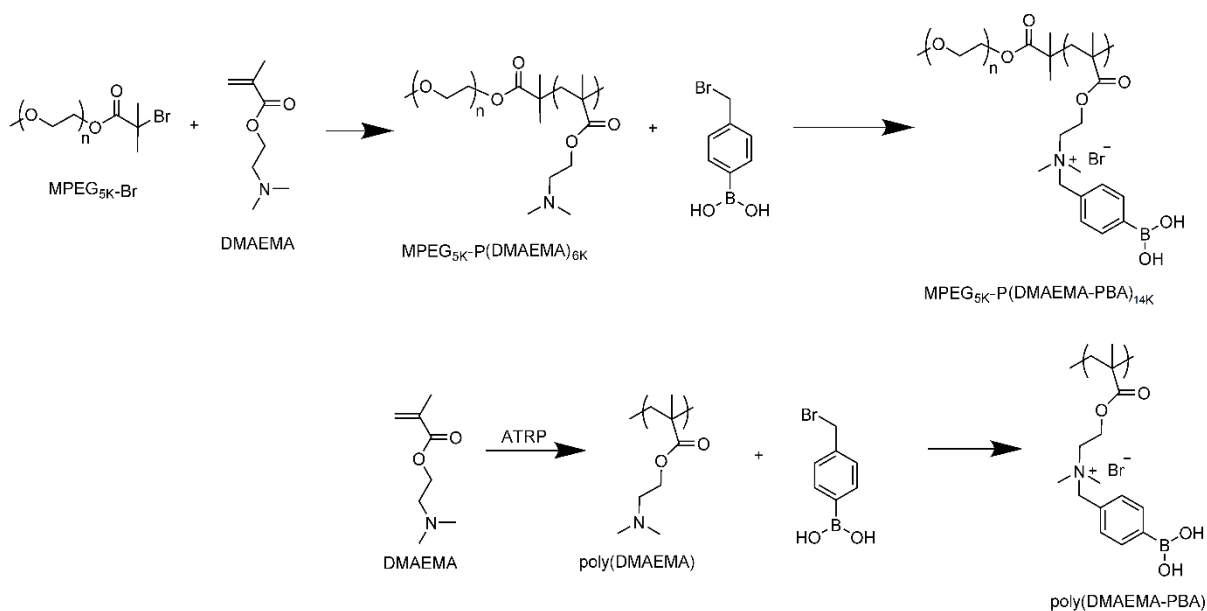


Figure 5.2 Synthetic routes of polymers utilized in this study.

5.2 Experimental Section

5.2.1 Materials

4-(Bromomethyl) phenylboronic acid was purchased from Boron Molecular. All other chemical reagents were purchased from Sigma-Aldrich. Insulin was purchased from Gibco. MPEG_{5K}-Br was synthesized as reported.¹⁹⁹ Poly(vinyl alcohol) (PVA, 89-98 KDa) and polyvinylpyrrolidone (PVP, ~55 KDa) were purchased from Sigma-Aldrich.

5.2.2 Synthesis of MPEG_{5K}-P(DMAEMA)_{6K}

MPEG_{5K}-Br (0.2 g, 0.04 mmol), CuBr (5.7 mg, 0.04 mmol) and 2, 2'-dipyridine (12.5 mg, 0.08 mmol) were added to a round bottom flask and protected with the N₂ atmosphere. To this mixture, THF (2 mL) and DMAEMA (0.2 g, 1.3 mmol) were added sequentially and mixed gently. After three freeze-thaw cycles, the flask was sealed with N₂, immersed in an oil bath and stirred overnight at 60 °C. The resultant solution was poured into ethyl acetate (100 mL)

and washed with NaHCO_3 (0.1 N, 3×50 mL) and dried over anhydrous Na_2SO_4 . After filtration and removing the solvent, slightly yellow viscous solid was obtained (0.2 g, yield 50%). $^1\text{H-NMR}$ (300 MHz, CDCl_3) was shown in Figure 5.3.

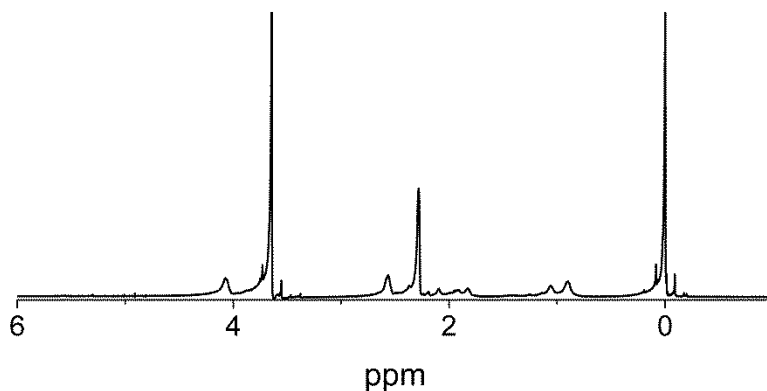


Figure 5.3 The $^1\text{H-NMR}$ spectrum of $\text{MPEG}_{5\text{K}}\text{-P(DMAEMA)}_{6\text{K}}$.

5.2.3 Synthesis of $\text{MPEG}_{5\text{K}}\text{-P(DMAEMA-PBA)}_{6\text{K}}$

$\text{MPEG}_{5\text{K}}\text{-P(DMAEMA)}_{6\text{K}}$ (0.11 g, 0.01 mmol) and 4-(bromomethyl)phenylboronic acid (0.5 g, 2.3 mmol) were dissolved in DMF separately and mixed. The mixture was stirred at 60°C overnight and dialysis against H_2O (3×2 L). After filtration and lyophilization, white product was obtained (0.15 g, yield 75 %). $^1\text{H-NMR}$ (300 MHz, D_2O) was shown in Figure 5.4. Upon comparison of the relative integrations 2 of two proton signals (7.0-8.0 ppm vs 4.0-4.5 ppm), about 90 % of DMAEMA residuals was substituted by PBA.

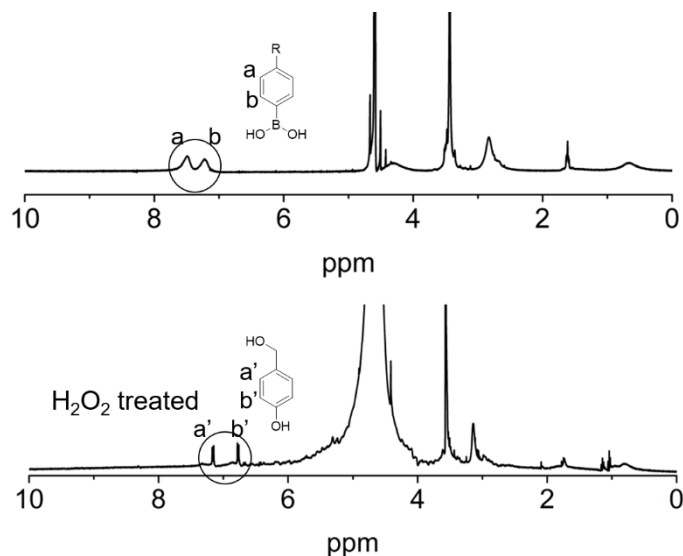


Figure 5.4 The $^1\text{H-NMR}$ spectra of $\text{MPEG}_{5\text{K}}\text{-P(DMAEMA-PBA)}_{14\text{K}}$ before and after H_2O_2 (80 mM) treatment.

5.2.4 Synthesis of poly(DMAEMA)

DMAEMA (0.2 g, 1.3 mmol), CuBr (5.7 mg, 0.04 mmol), ethyl α -bromoisobutyrate (8 mg, 0.04 mmol), and 2, 2'-dipyridine (12.5 mg, 0.08 mmol) were added to a round bottom flask and protected with the N_2 atmosphere. To this mixture, THF (2 mL) and ethyl α -bromoisobutyrate (8 mg, 0.04 mmol) were added sequentially and mixed gently. After three freeze-thaw cycles, the flask was sealed with N_2 , immersed in an oil bath and stirred overnight at $60\text{ }^\circ\text{C}$. The resulted solution was poured into ethyl acetate (100 mL) and washed with NaHCO_3 (0.1 N, $3 \times 50\text{ mL}$) and dried over anhydrous NaSO_4 . After filtration and removing the solvent, slightly yellow viscous solid was obtained and was used directly (0.14 g, yield 70%). $^1\text{H-NMR}$ (300 MHz, CDCl_3) was shown in Figure 5.5.

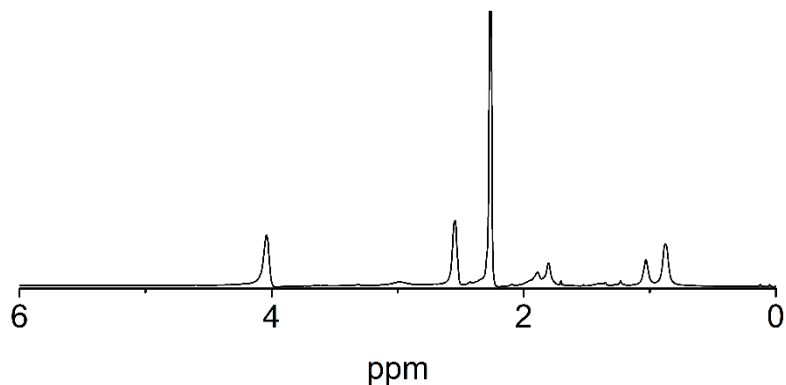


Figure 5.5 The ^1H -NMR spectrum of poly(DMAEMA) synthesized by ATRP initiated by ethyl α -bromoisobutyrate.

5.2.5 Synthesis of poly(DMAEMA-PBA)

Poly(DMAEMA) (0.1 g) and 4-(bromomethyl) phenylboronic acid (0.5 g, 2.3 mmol) were dissolved in DMF separately and mixed. The mixture was stirred at 60 °C overnight and dialysis against H_2O (3×2 L). After filtrated and lyophilized, white product was obtained. ^1H -NMR (300 MHz, D_2O) was shown in Figure 5.6. Upon comparison of the relative integrations 2 of two proton signals (7.0-8.0 ppm vs 4.0-4.5 ppm), about 95 % of DMAEMA residuals was substituted by PBA.

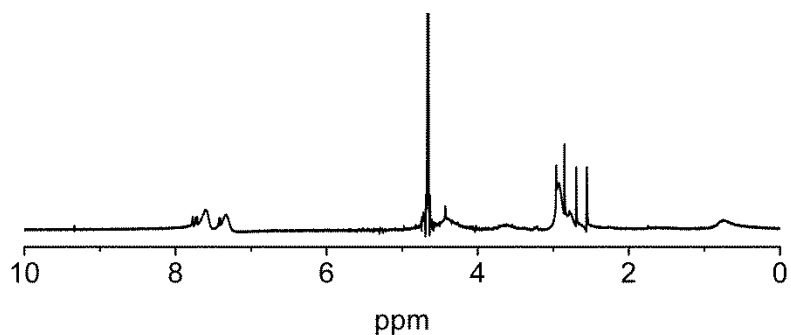


Figure 5.6 The ^1H -NMR spectrum of poly(DMAEMA-PBA).

5.2.6 Synthesis of poly(vinyl alcohol) methacrylate

Poly(vinyl alcohol) (1 g) and methyl anhydride (1 g) were dissolved in DMSO (20 mL), and Et₃N (1 mL) was added as a catalyst. The mixture was stirred overnight at room temperature and dialysis against H₂O (3×2 L) and lyophilized to obtain the product. ¹H-NMR (300 MHz, d-DMSO) was shown in Figure 5.7.

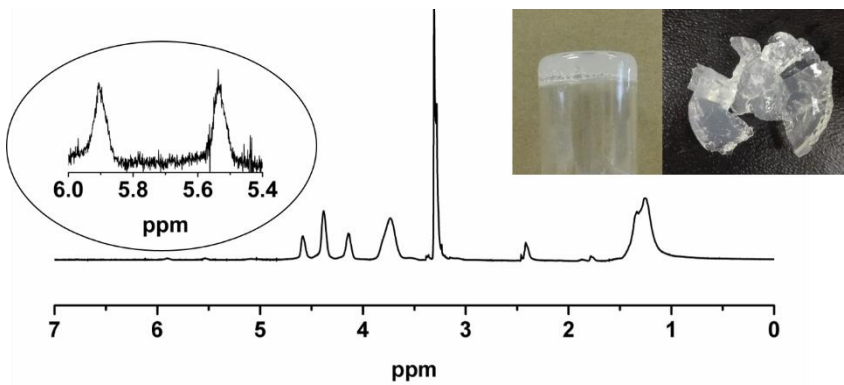


Figure 5.7 ¹H-NMR of PVA methacrylate and its gel in aqueous solution.

5.2.7 Rhodamine B or FITC labeled insulin or CAT

Rhodamine B isothiocyanate (0.5 mg) dissolved in DMSO (1 mL) was added to insulin (20 mg) dissolved in NaHCO₃ aqueous solution (100 mM, 1 mL). The mixture was stirred for one hour and dialyzed against H₂O (3×2 L). The resultant solution was lyophilized to obtain rhodamine B labeled insulin. Other fluorescence-labeled proteins were obtained with the same method. The fluorescence-labeled insulin or CAT were used in the same way as the one not labeled, and the fluorescence images were taken on a fluorescence microscope (Olympus, IX71).

5.2.8 H₂O₂ generation rate assay

The H₂O₂ concentration in solution was evaluated using a fluorometric hydrogen peroxide assay kit according to the manufacturer's protocol (Sigma-Aldrich). Glucose solutions (100 or 400 mg/dL) containing GOx-NC or GOx (0.2 mg/mL) were incubated at 37 °C. Samples (10 µL each tube) were withdrawn and diluted at timed intervals, and the fluorescence intensity was detected.

5.2.9 Preparation of insulin-NCs or GOx-NCs

Typically, insulin (2 mg/mL, 5 mL) or GOx (1 mg/mL, 5 mL) and MPEG_{5K}-P(DMAEMA-PBA)_{14K} (1 mg/mL, 5 mL) were mixed, and the pH was adjusted to 7.4. During this process, complex micelles were generated, and PVA (1 wt%, 0.5 mL) (for insulin-NC) or PVA methacrylate (1 wt%, 0.5 mL) (for GOx-NC) was added as a stabilizer to obtain insulin-NC without or GOx-NC with further exposure to UV light (365 nm, 6 × 10 s).

5.2.10 *In vitro* insulin release from the complex of insulin and poly(DMAEMA-PBA)

The complex was suspended in 10 mM PBS at pH 7.4 and allocated to centrifuge tubes. Various amounts of glucose (0, 100 or 400 mg/dL final concentration) and GOx (0.2 mg/mL) were added to the solutions. At predetermined time intervals, solution (20 µL each tube) was withdrawn and centrifuged, supernatant (10 µL) was stained with Coomassie blue (200 µL), and the absorbance at 595 nm was detected on an Infinite 200 PRO multimode plate reader (Tecan Group Ltd.). The insulin concentration was calibrated by a standard curve.

5.2.11 *In vitro* insulin (or GOx) release from Ins-NCs (or GOx-NCs) from the PVA methacrylate gel (with insulin as an example)

Ins-NCs (1 mg/mL) solution and radical initiator were mixed with PVA methacrylate solution (5 wt% in H₂O) and irradiated to form a gel. The gel was added to centrifuge tubes containing glucose (100 or 400 mg/dL). At predetermined time intervals, solution (10 µL each tube) was withdrawn, stained with Coomassie blue (200 µL) and the absorbance at 595 nm was detected on an Infinite 200 PRO multimode plate reader (Tecan Group Ltd.). The insulin concentration was calibrated by a standard curve.

5.2.12 Fabrication of microneedle array patch (with MN(G+C+I) as an example)

All the MNs in this study were prepared using commercial silicone moldspurchased from Blueacre Technology Ltd. Each MN had a round base of 300 µm in diameter, which tapers over a height of 600 µm to a tip of 5 µm diameter. The MNs were arranged in a 20×20 array with 600 µm tip-tip spacing. First, diluted aqueous solutions of PVA (contain 10 % PVA methacrylate, 3.5 wt% in H₂O, 500 µL), CAT-NG (1 mg in 400 µL H₂O) and a photoinitiator (Irgacure 2959; 5 wt%) were prepared and mixed. After deposition of this solution (100 µL) in a silicone mold, the solution was kept under reduced vacuum for 30 minutes and then transferred to a Hettich Universal 32R centrifuge for 30 min at 2000 rpm. Then, diluted aqueous solutions of PVA: PVP (2:1), PVA methacrylate (5 % in total), GOx-NCs, Ins-NCs and photoinitiator (Irgacure 2959; 5 wt%) were loaded into a mold, and this procedure was repeated for several times until predetermined amount of Ins-NCs was loaded. Finally, the microneedle array patch was dried under vacuum for 2 days. After the desiccation, the MN arrays were carefully peeled off the silicone mold, and the MNs underwent crosslinking via

UV irradiation (365 nm, BlueWave® 75 UV Curing Spot Lamp) for six cycles of 10-second exposure. The morphology of the MNs was characterized on an FEI Verios 460L field-emission scanning electron microscope.

5.2.13 Mechanical strength test

The mechanical strength of microneedles with a stress-strain gauge was determined by pressing a stainless-steel plate against microneedles on an MTS 30G tensile testing machine. The initial gauge was 2.00 mm between the tips of microneedle and the plate, with 10.00 N as the load cell capacity. The speed of the plate approaching microneedles was set as 0.1 mm/s. The failure force of microneedles was recorded as the force at which the needle began to buckle.

5.2.14 *In vitro* cytotoxicity assay

The cytotoxicity of materials to HeLa cells was determined using 3-(4,5-dimethylthiazol-2-yl)-2,5-diphenyltetrazolium bromide (MTT) assay. Briefly, HeLa cells (5000 cells per well) were plated into 96-well plates and incubated overnight. Then cells were exposed to serial dilutions of carrier materials for 40 h. Subsequently, the medium in each well was replaced with fresh culture medium containing 0.5 mg/mL MTT. The plates were incubated for another 2 h before the addition of DMSO to dissolve the formazan crystals. The absorbance of each individual well was measured at 562 nm with a microplate spectrophotometer. Each drug concentration was tested in triplicate and in three independent experiments.

5.2.15 *In vivo* studies using streptozotocin-induced diabetic mice

The *in vivo* efficacy of MN-array patches for diabetes treatment was evaluated in adult diabetic mice (male C57B6, age 8 weeks; Jackson Laboratory) induced using streptozotocin. The animal study protocol was approved by the Institutional Animal Care and Use Committee at North Carolina State University and the University of North Carolina at Chapel Hill. The blood glucose levels were measured using tail vein blood samples (~3 μ L) of mice using the Clarity GL2Plus glucose meter (Clarity Diagnostics). The mouse glucose levels were consistently measured before treatment. For each group, five mice were selected to be treated using MN patches or native insulin. The glucose level of each mouse was monitored until stabilization.

5.2.16 *In vitro* skin penetration test

To evaluate the *in vitro* skin penetrating ability of MNs, the MNs were inserted into the mouse skin for 10 min. The skin was excised and stained with trypan blue for 10 min before imaging by optical microscopy (Leica EZ4 D stereomicroscope).

5.2.17 Animal experiment

The sample size calculated by power analysis: G*power 3.1. The experiments did not use a method of randomization. The investigators were not blinded to allocation during experiments and outcome assessment.

5.2.18 Statistical analysis

Differences in blood glucose levels between the treated groups and controlled groups were determined by unpaired Student's *t*-test. The results were considered statistically significant if

the two-tailed *P*-values were less than 0.05. The statistical approach remained consistent throughout all analyses.

5.3 Results and Discussion

5.3.1 Synthesis and characterization of nano-complexes

Through the atom transfer radical polymerization (ATRP) initiated by polyethylene glycolyl monomethyl ether 2-bromoisobutyrate (MPEG_{5K}-Br), 2-(dimethylamino)ethyl methacrylate (DMAEMA) was polymerized to obtain MPEG_{5K}-P(DMAEMA)_{6K} (Figure 5.2, 5.3 and 5.8), which was subsequently modified with 4-(bromomethyl)phenylboronic acid to obtain the positively charged MPEG_{5K}-P(DMAEMA-PBA)_{14K} (Figure 5.4 and 5.9). In the presence of H₂O₂, phenylboronic acid on MPEG_{5K}-P(DMAEMA-PBA)_{14K} was oxidized and hydrolyzed, generating MPEG_{5K}-P(DMAEMA)_{6K} with reduced positive charge (Figure 5.1b), as demonstrated by ¹H-NMR (Figure 5.4).²⁰⁰ In addition, poly(DMAEMA) and poly(DMAEMA-PBA) were synthesized *via* ATRP initiated by ethyl α -bromoisobutyrate and subsequent quaternarization by 4-(bromomethyl)phenylboronic acid, respectively (Figure 5.5, 5.6, 5.10 and 5.11). Given its isoelectric point of ~ 5.3 ,²⁰¹ insulin is negatively charged at pH 7.4 and capable of complexing with positively charged MPEG_{5K}-P(DMAEMA-PBA)_{14K}²⁰² to form Ins-NCs with a PEG corona and a complex core.²⁰³ To further stabilize the micelle structure, PVA was incorporated *via* forming acid-inert ester bonds between the phenylboronic acids on poly(DMAEMA-PBA) and *cis*-1, 3-diols on PVA.²⁰⁴ Therefore, Ins-NCs with a loading capacity of 50 wt%, an average hydrodynamic size around 60 nm, and ζ -potential of 4.4 ± 0.5 mV were achieved as measured by dynamic light scattering (DLS) (Figure 5.12a) and transmission electronic microscopy (TEM) (Figure 5.12b).²⁰⁴⁻²⁰⁵ When Ins-NCs were degraded,

the solution gradually became transparent after incubation with glucose (400 mg/dL) in the presence of GOx (Figure 5.13). Meanwhile, GOx was also integrated into *m*-PVA stabilized nanocomplex micelles (GOx-NCs), with an average hydrodynamic size of around 50 nm (Figure 5.14) and ζ -potential of 2.1 ± 0.4 mV. In addition, a non-egradable network of *m*-PVA on GOx-NCs formed upon exposure to UV light (365 nm, 6×10 s). GOx-NCs had a GOx loading capacity of 33 wt%, and showed similar activity to native GOx regarding catalyzing the oxidation of glucose to produce H₂O₂ (Figure 5.12c).²⁰⁶ Furthermore, a different pH value after GOx-NC catalysis indicated a glucose concentration-dependent manner of gluconic acid generation (Figure 5.12d).

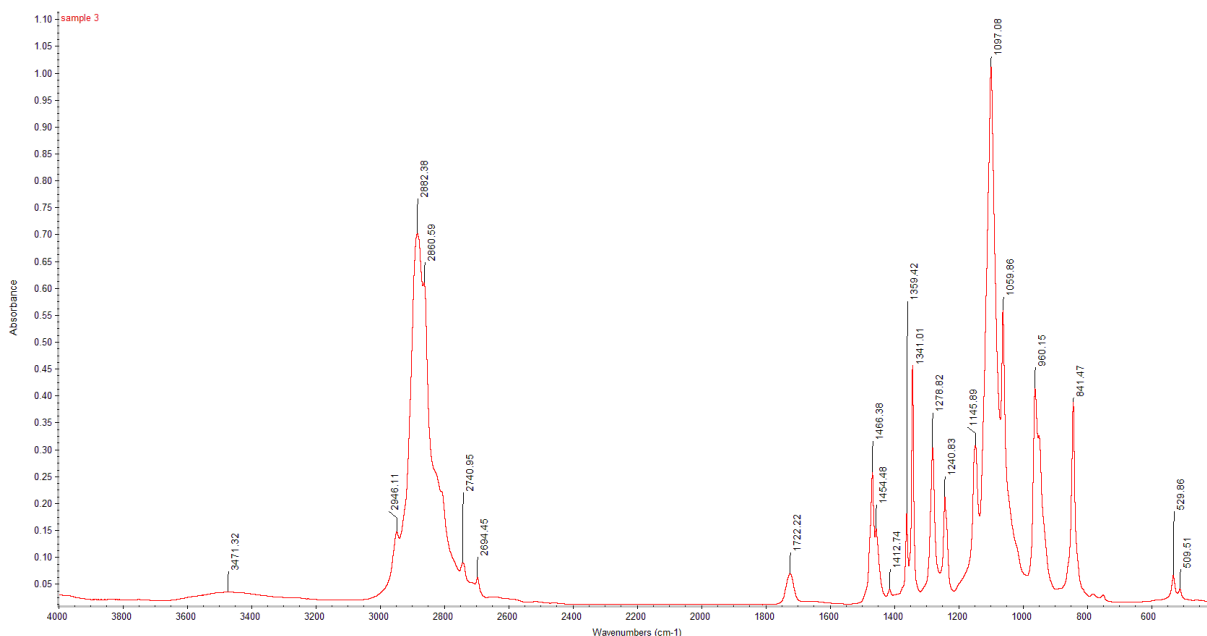


Figure 5.8 The FT-IR spectrum of MPEG_{5K}-P(DMAEMA)_{6K}.

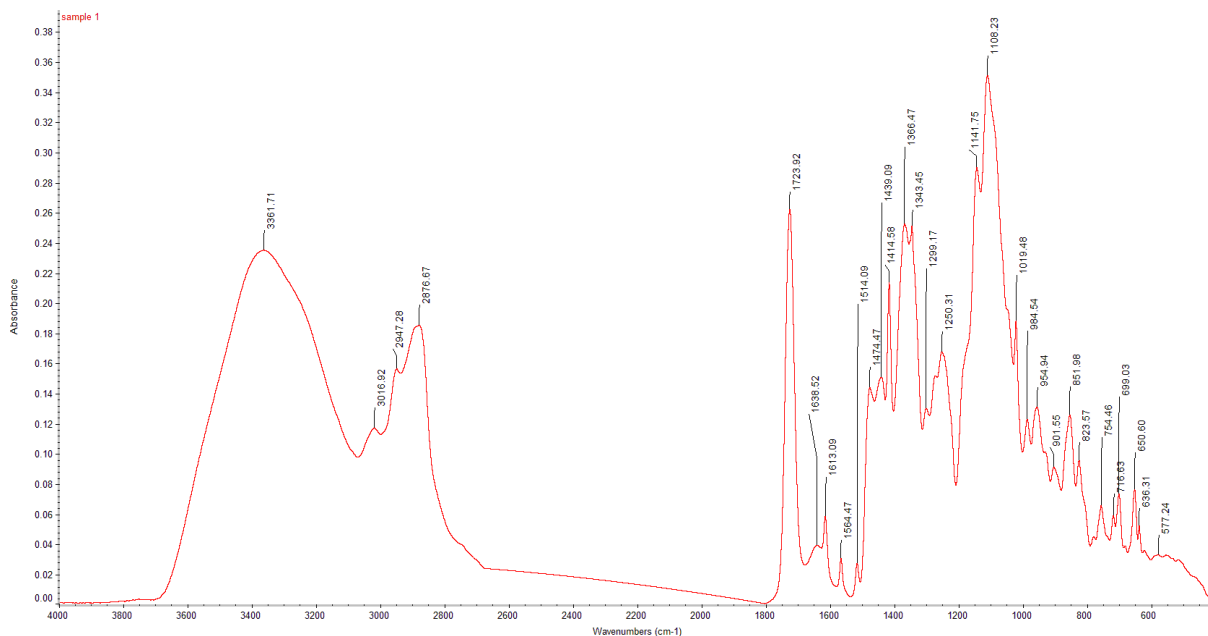


Figure 5.9 The FT-IR spectrum of MPEG_{5K}-P(DMAEMA-PBA)_{14K}.

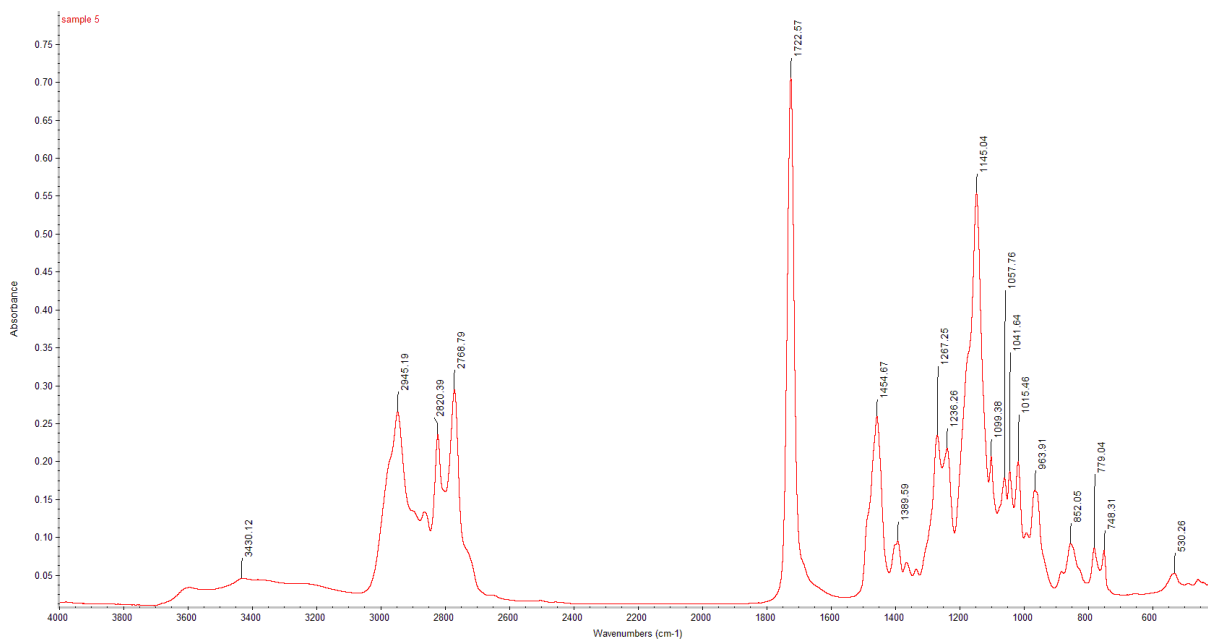


Figure 5.10 The FT-IR spectrum of poly(DMAEMA) synthesized by ATRP initiated by ethyl α -bromoisobutyrate.

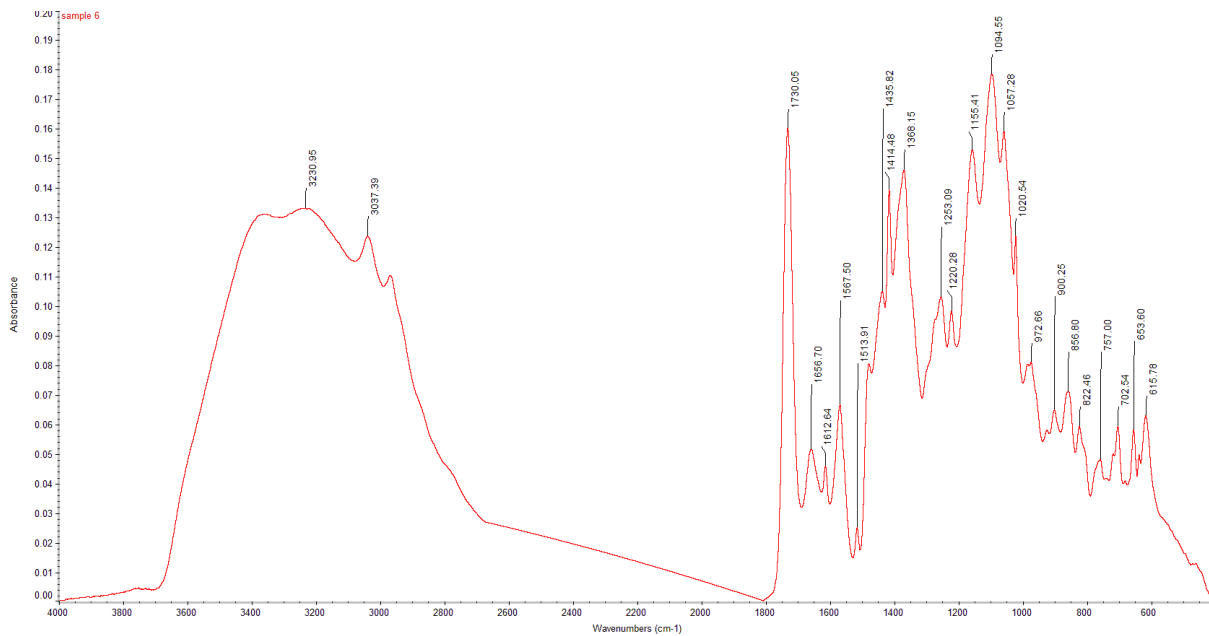


Figure 5.11 The FT-IR spectrum of poly(DMAEMA-PBA).

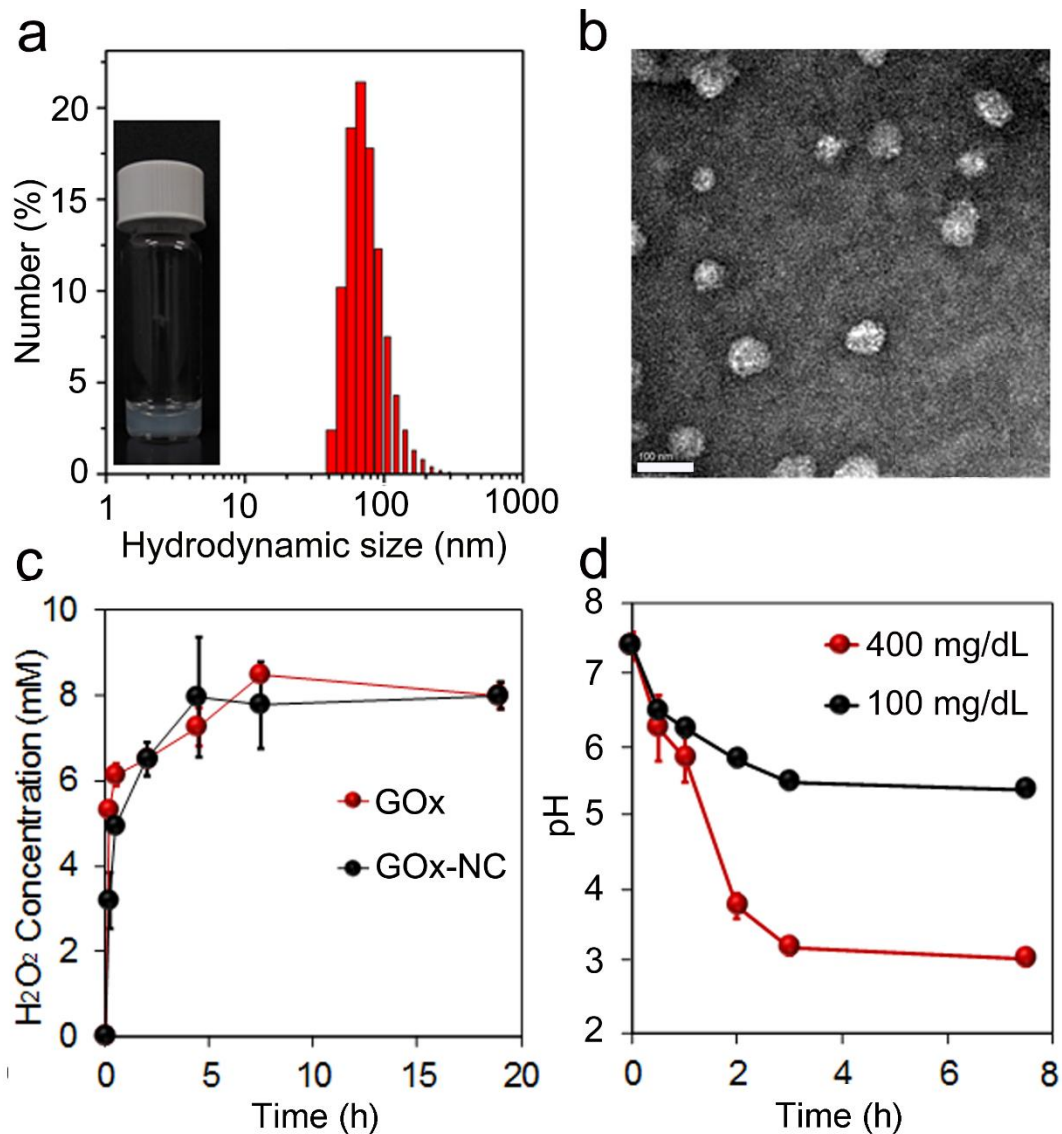


Figure 5.12 Characterizations of Ins-NCs and GOx-NCs. (a) Representative image of Ins-NC solution and hydrodynamic size distribution of Ins-NCs as determined by DLS. Inset: A representative picture of the Ins-NC solution sample (insulin concentration: 1 mg/mL). (b) Representative TEM image of Ins-NCs. Scale bar: 100 nm. (c) H₂O₂ generation in PBS (10 mM, pH 7.4) of various glucose (400 mg/dL) as catalyzed by GOx and GOx-NCs. (d) The pH change of PBS solution containing different glucose concentrations (100 or 400 mg/dL) in the presence of GOx-NCs (0.2 mg/mL GOx-eq. concentration). Data points represent mean \pm SD (n=3). Error bars indicate SD.

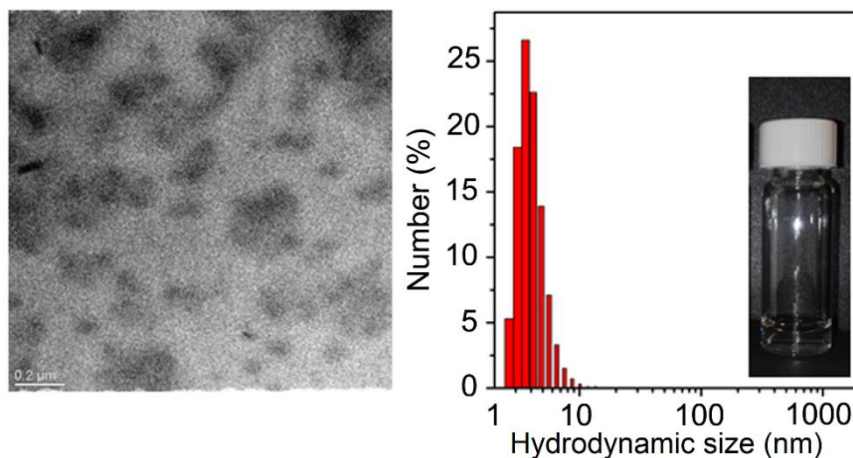


Figure 5.13 Representative TEM image and size distribution of Ins-NCs after treatment with PBS containing glucose (400 mg/dL) in the presence of GOx.

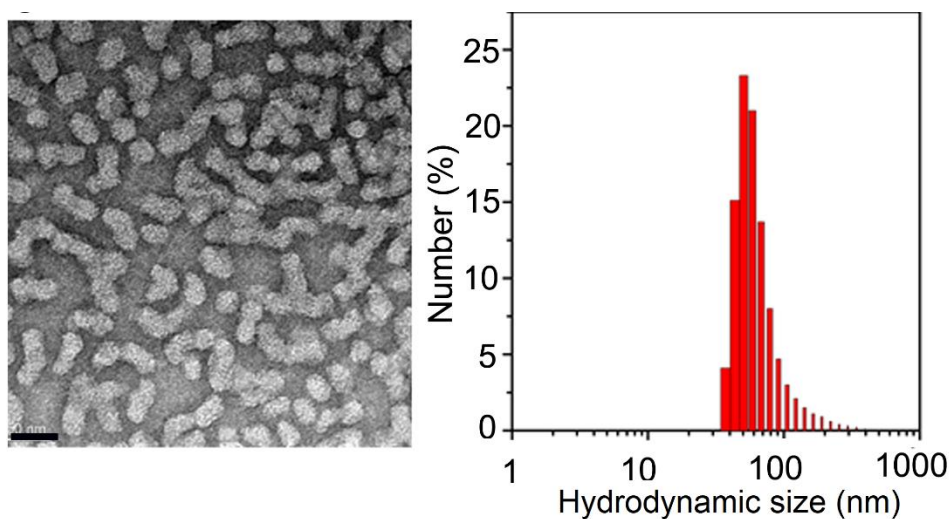


Figure 5.14 Representative TEM images and size distribution of GOx-NCs. Scale bar: 50 nm.

5.3.2 *In vitro* glucose-responsive insulin release

Next, the insulin release rate was evaluated in the presence of GOx in phosphate buffered saline (PBS) at pH 7.4 with three different glucose concentrations, including a typical hyperglycemic level (400 mg/dL), a normoglycemic level (100 mg/dL), and a control level (0 mg/dL). The insulin release rate was remarkably promoted under a hyperglycemic state compared to those of other two groups (Figure 5.15a).

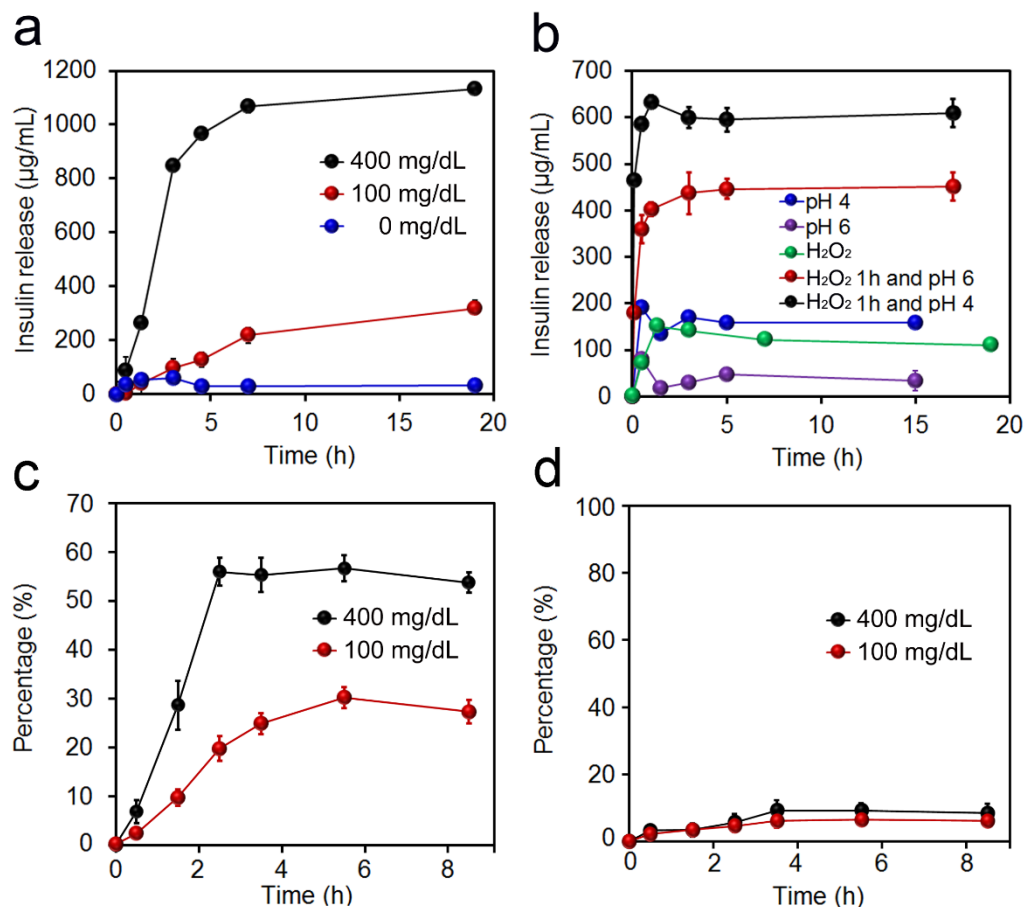


Figure 5.15 *In vitro* characterization of glucose-responsive insulin release. (a) Glucose concentration-dependent insulin release from a complex of insulin in PBS 7.4 in the presence of GOx (0.2 mg/mL). The glucose concentration was set as 0, 100 and 400 mg/dL. (b) H₂O₂ (5 mM) and pH cascade-triggered insulin release from a complex of insulin. (c) Glucose concentration-dependent insulin release from Ins-NCs loaded in *m*-PVA gel in PBS 7.4 in the presence of GOx (0.2 mg/mL). (d) Glucose concentration-dependent GOx release from GOx-NCs encapsulated in *m*-PVA gel in PBS 7.4. Additional GOx (0.2 mg/mL) was added. The glucose concentration was set as 100 and 400 mg/dL. Data points represent mean \pm SD ($n = 3$). Error bars indicate SD.

Furthermore, the mechanism of glucose-triggered insulin release was investigated. Prior to PVA crosslinking, instant insulin release was triggered in both 100 and 400 mg/dL glucose solution (Figure 5.16). However, the addition of PVA stabilized the complex and significantly reduced insulin release in 100 mg/dL glucose solution (Figure 5.15a). Further studies indicated that neither H₂O₂ nor slightly acidic environment could individually achieve insulin release

(Figure 5.15b). Moreover, insulin was found to be instantly released in slightly acidic pH from the complex that was pretreated with H₂O₂, indicating that the insulin was released in a cascade: 1) poly(DMAEMA-PBA) was oxidized and hydrolyzed to poly(DMAEMA), leading to reduced positive charge of polymer and crosslinking density of Ins-NCs; 2) the gradually decreased pH led to reduced negative charge or even charge reversal of insulin (from negative to positive charge under pH lower than isoelectronic point), thereby resulting in the dissociation of complex and subsequent release of insulin. This two-step pattern of insulin release endows the insulin delivery system enhanced safety for *in vivo* application to avoid the unwanted insulin release solely triggered by either H₂O₂ or acid, for example, generated in a nonrelevant condition of inflammation.²⁰⁷ Moreover, the release rate of insulin from complex was steadily enhanced when gradually increasing the glucose concentrations of the tested solutions from normoglycemic to hyperglycemic conditions, where a 50-fold difference in insulin release rate was achieved in 1 h when the glucose concentration was increased from 100 to 400 mg/dL (Figure 5.17). Additionally, the pulsatile release profile of insulin was achieved when the complex was alternatively exposed to the normoglycemic and hyperglycemic levels (Figure 5.18).

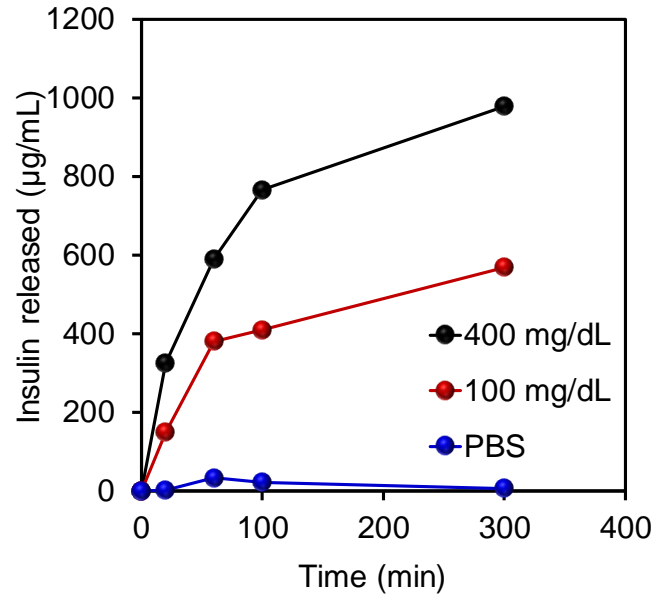


Figure 5.16 Insulin release profile from complex formed between insulin and poly(DMAEMA-PBA) in PBS at pH 7.4 in the presence of GOx (0.2 mg/mL) with different glucose concentration (400, 100 and 0 mg/dL).

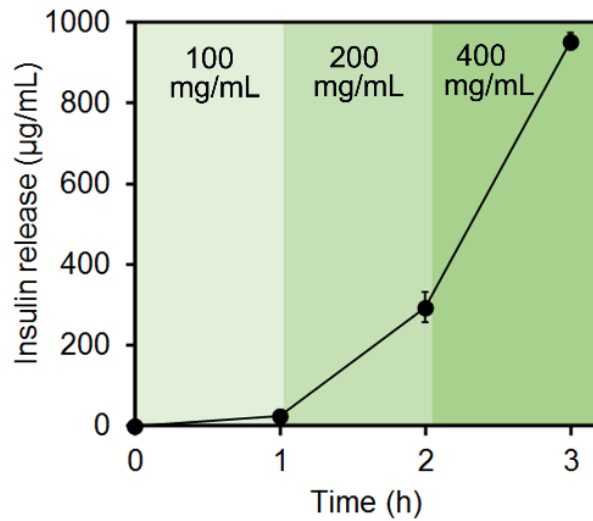


Figure 5.17 Self-regulated insulin release profile as a function of glucose concentration. Data points represent mean \pm SD (n = 3). Error bars indicate SD.

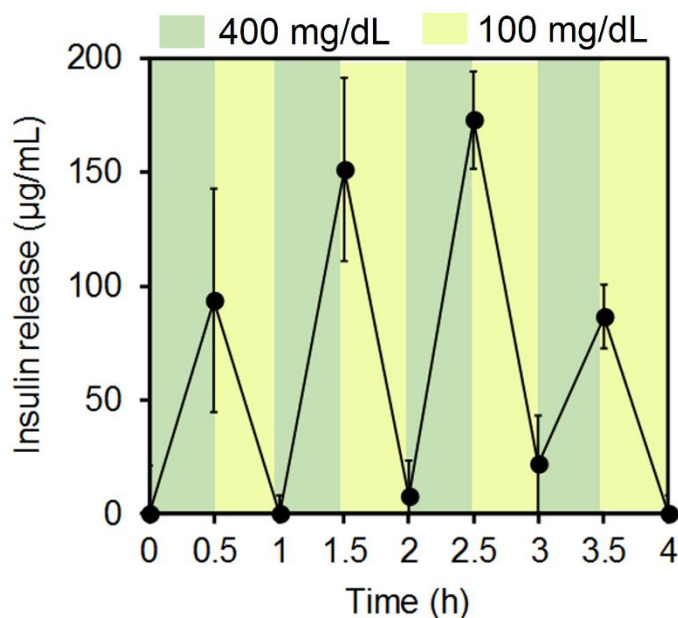


Figure 5.18 Pulsatile insulin release profile as a function of glucose concentrations over time. Data points represent mean \pm SD ($n = 3$). Error bars indicate SD.

The insulin and GOx release profiles from nanocomplex micelles encapsulated in *m*-PVA gel were critical for their *in vivo* application. The *m*-PVA gel was prepared from *m*-PVA aqueous solution *via* exposure to UV light in the presence of a radical initiator (Figure 5.7). The release rate of insulin from Ins-NCs entrapped in the gel was two-fold faster at a glucose concentration of 400 mg/dL than that of 100 mg/dL (Figure 5.15c). Meanwhile, the release rate of GOx was independent on glucose level and occurred in negligible amounts due to the crosslinking of GOx-NCs by *m*-PVA (Figure 5.15d). Additionally, the far-UV circular dichroism spectra of the native and released insulin from gels were nearly identical, suggesting that the released insulin retained α -helical secondary structure associated with bioactivity (Figure 5.19).

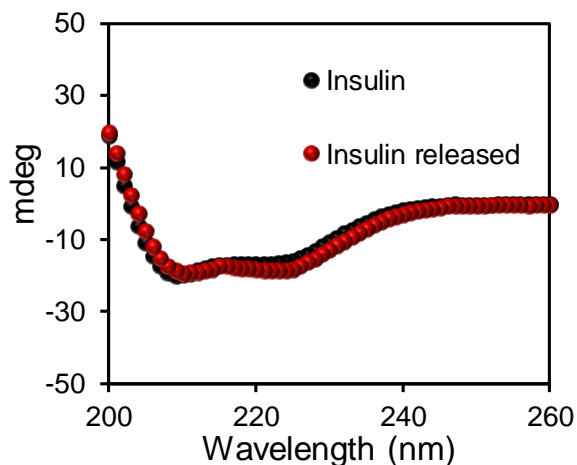


Figure 5.19 CD spectra of native insulin solution and insulin released from the gels incubated with 400 mg/dL glucose.

5.3.3 Fabrication and characterization of insulin-loaded MN-array patch

To facilitate the administration, Ins-NCs and GOx-NCs were integrated into an MN array patch. The MN array patch was prepared using a micromolding approach. First, the CAT was encapsulated into a CAT-NG to inhibit passive release of CAT (Figure 5.20).¹⁰⁴ CAT-NG retained the activity of catalyzing H_2O_2 to H_2O (Figure 5.21), and was then dissolved in an aqueous solution containing *m*-PVA and photoinitiator, loaded into a silicone micromold, and kept under reduced pressure for 30 min. After centrifugation, it was exposed to UV light (6×10 s) to crosslink the matrix to form an MN “sheath”. Ins-NCs, GOx-NCs and radical initiator dissolved in an aqueous solution containing PVA/*m*-PVA and polyvinylpyrrolidone (PVP) were then deposited in silicone molds to form an MN “core”. The addition of a proper ratio of PVP has been shown to enhance the strength of microneedle for better skin penetration.²⁰⁸ The resulting device was arranged in a 20×20 MN array on a patch. The needle had a conical shape (Figure 5.22a-b) and enough strength (Figure 5.23).²⁰⁹⁻²¹⁰ In addition, fluorescein isothiocyanate (FITC)-labeled CAT-NG formed a sheath covering the PVA/*m*-PVA/PVP core

loaded with the rhodamine B-labeled insulin as validated using fluorescence microscope (Figure 5.22c).

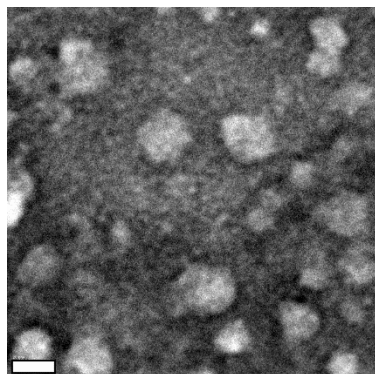


Figure 5.20 Representative TEM image of CAT-NG. Scale bar: 20 nm.

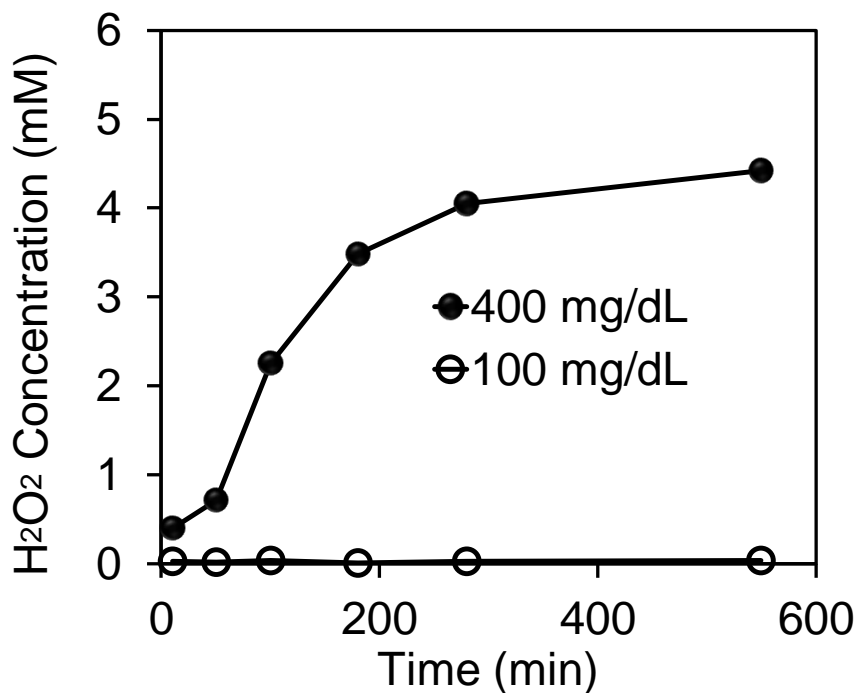


Figure 5.21 The H₂O₂ generation rate *via* glucose oxidation as catalyzed by GOx-NC in the presence of CAT-NG in glucose solution (100 or 400 mg/dL) in PBS with an initial pH at 7.4. The concentration of GOx and CAT was set to 0.2 mg/mL GOx-eq. concentration and 0.08 mg/mL CAT-eq. concentration, respectively.

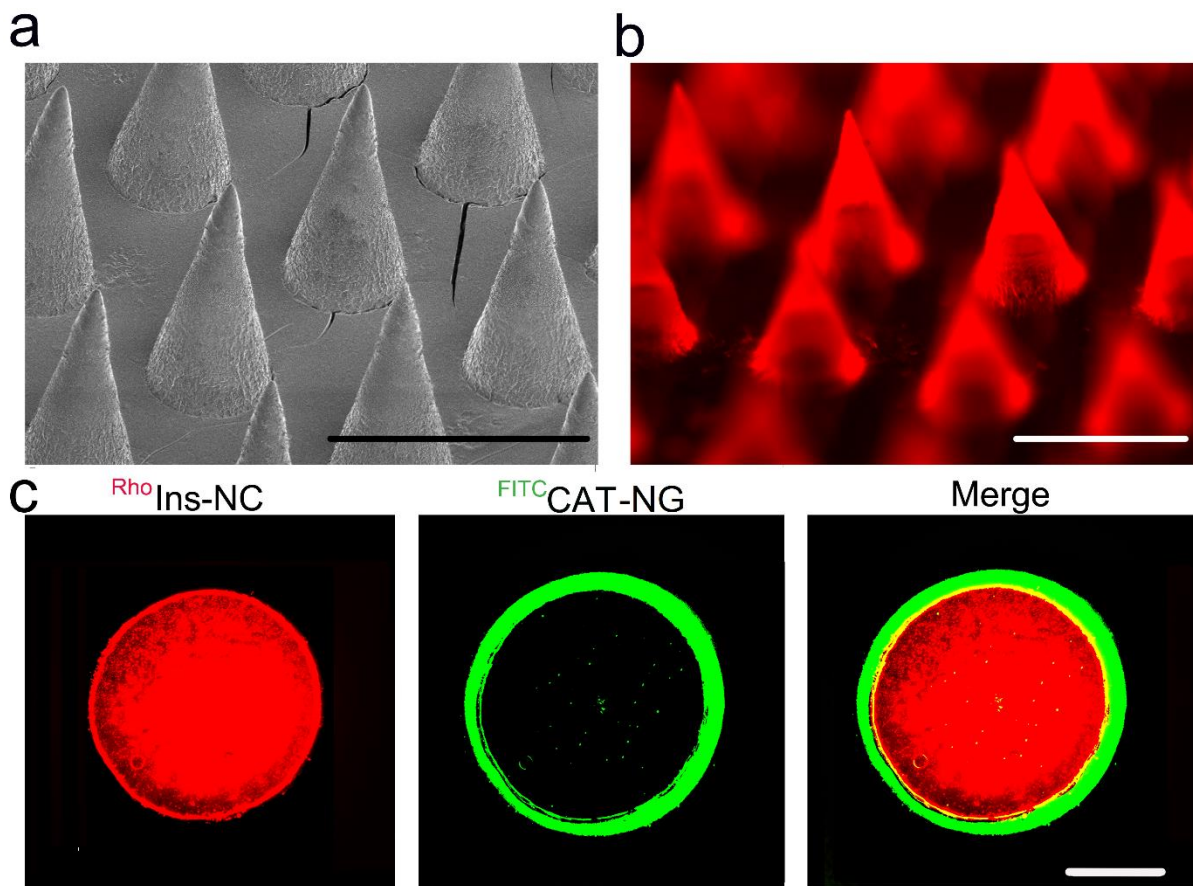


Figure 5.22 Characterization of the MN array patch with a sheath structure. (a) Representative scanning electron microscopy (SEM) image of microneedle array patch. Scale bar: 600 μm . (b) Representative fluorescence microscopy image of MN arrays loaded with rhodamine B-labeled insulin. Scale bar: 600 μm . (c) Representative images of a cross-section of MN with a CAT-NG sheath: rhodamine B labeled insulin (red), FITC labeled CAT sheath layer (green), and merging of both images. The sheath layer was 23 ± 6 μm thick as analyzed using software ImageJ. Scale bar: 100 μm .

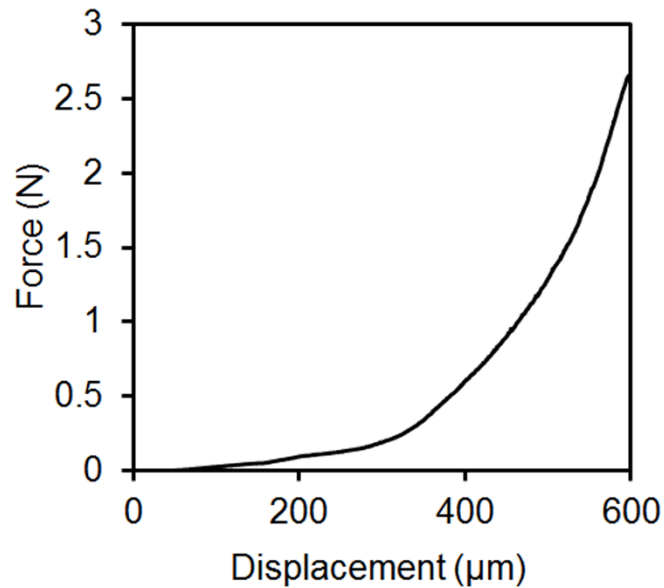


Figure 5.23 The mechanical strength test of microneedle.

5.3.4 *In vivo* studies of the MNs for type 1 diabetes treatment

The *in vivo* performance of the MN array patches was evaluated utilizing a mouse model of type 1 diabetes induced by streptozotocin. The mice were divided into four groups treated with 1) CAT-NG coated MN array patch loaded with GOx-NCs and Ins-NCs (MN-(G+C+I)); 2) subcutaneous injection of human recombinant insulin; 3) microneedle array patch loaded with blank PVA/*m*-PVA and PVP (MN-Gel); and 4) CAT-NG coated MN array patch of Ins-NCs (MN-(C+I)). The staining by trypan blue indicated successful penetration of MNs into the excised skin (Figure 5.24). Besides, the temporal microchannels on the skin caused by MNs could quickly recover within 2 h posttreatment (Figure 5.25).

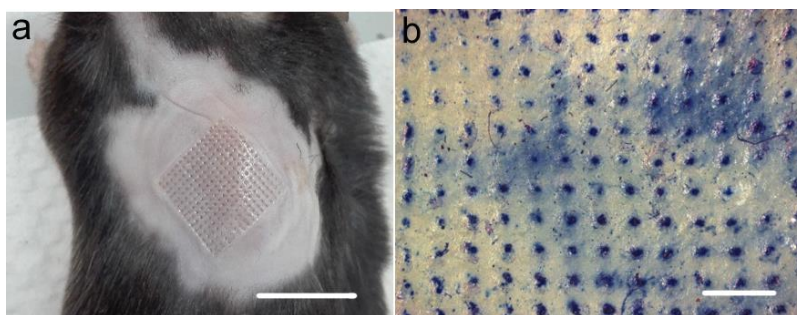


Figure 5.24 Images of a mouse treated by MN (a) and the trypan blue staining (b). Scale bars: 1 cm for (a) and 600 μm for (b).



Figure 5.25 Skin puncture marks at 0, 5 and 120 min post-treatment of MNs. Scale bar: 0.5 cm.

BGLs of the mice were monitored over time following treatment with MN patches. It was observed that the BGLs of mice treated by MN-(G+C+I) were quickly decreased to around 100 mg/dL in 30 min post-administration and maintained below 200 mg/dL for almost 4 h, considerably longer than those of the mice subcutaneously injected with insulin (Figure 5.26a). This fast dynamic in BGL change was attributed to the rapid establishment of the local oxidative and acidic environment through oxidation of glucose absorbed from interstitial fluid, which has a similar glucose level to that in blood,²¹¹ as well as the high sensitivity of Ins-NCs to these stimuli. In contrast, the negligible BGL reduction was observed in the mice treated with MN-(C+I) and MN-Gel. Additionally, the plasma human insulin levels in mice treated with MN-(G+C+I) were significantly higher than those treated with MN-(C+I) (Figure 5.26b).

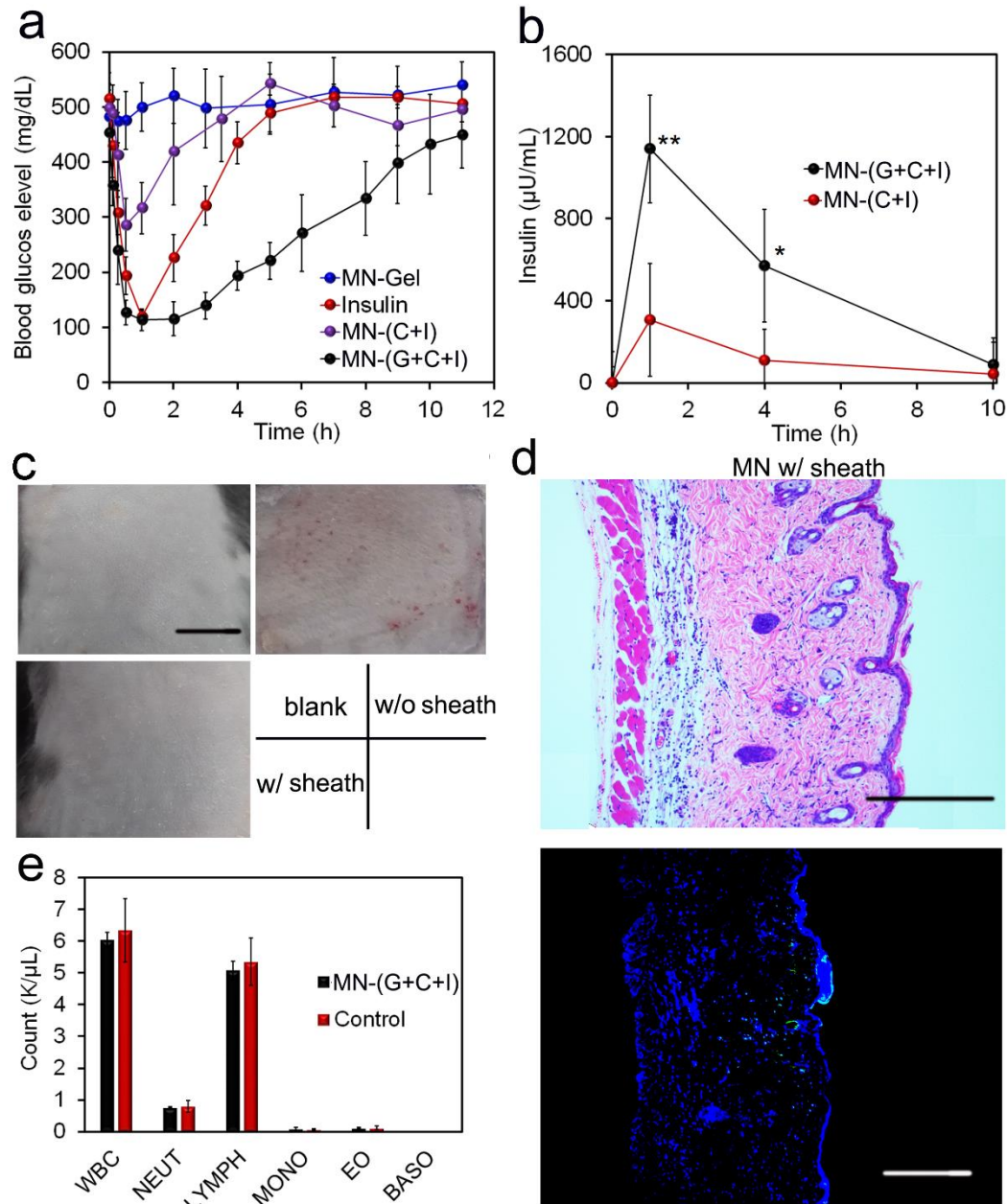


Figure 5.26 *In vivo* evaluation of MN array patches for type 1 diabetes treatment. (a) Blood glucose levels of type 1 diabetic mice treated with various kinds of microneedle array patches. (b) Blood insulin level of mice treated with MN array patches. Data points represent mean \pm SD ($n = 3$). $*P < 0.05$, $**P < 0.01$ (analyzed by two-tailed Student's t-test) for MN-(G+C+I) compared with control MN-(C+I). (c) Representative images of skins at the treated site of mice. Mice were treated with MN-Gel, MN-(G+I) and MN-(G+C+I) for 12 h, and the skins were gathered after the mice were euthanized. Scale bar: 1 cm. (d) H&E staining and immunohistologic staining with TUNEL assay (green) and Hoechst (blue) of skins treated with MN-(G+C+I). Scale bar: 300 μm . (e) Analysis of blood white cells of mice treated with MN-(G+C+I). Blood samples were obtained 2 d posttreatment. WBC: white blood cells; NEUT: neutrophils; LYMPH: lymphocytes; MONO: monocytes; EO: eosinophils; BASO: basophils.

Moreover, the intraperitoneal glucose tolerance test was carried out 1 h post-administration of MNs or insulin. A spike in BGLs was observed for all groups after the intraperitoneal injection of glucose. However, only healthy mice and MN-(G+C+I) could restore blood glucose levels to a normoglycemic level within a short period, and the mice treated with MN-(G+C+I) showed significantly enhanced glucose tolerance to the glucose challenge (Figure 5.27). To assess the risk of hypoglycemia associated with treatment by MN-(G+C+I), the BGLs of healthy mice treated with different MN array patches were observed. The BGLs of mice treated with insulin showed a remarkable decrease, while the BGLs of mice treated with MN-(G+C+I) showed only a slight decrease, consistent with the slow release of insulin from gels under a normoglycemic state (Figure 5.28a). Additionally, the MN-(G+C+I) treated group showed significantly lower hypoglycemia index than insulin (Figure 5.28b).

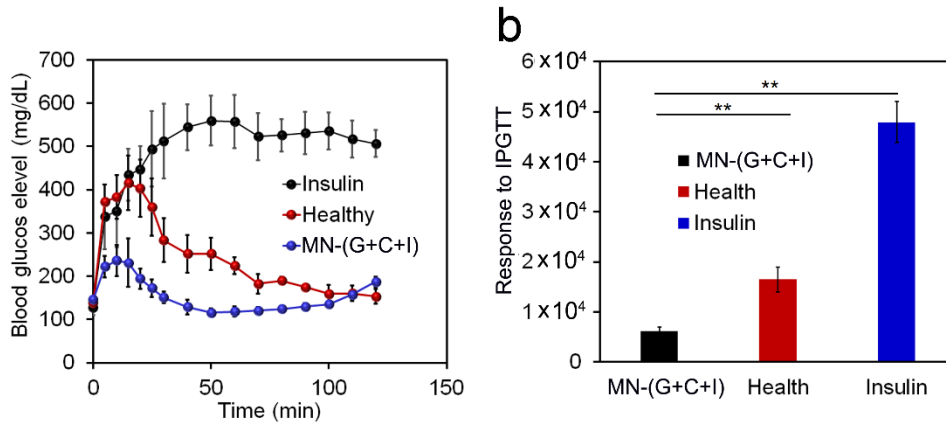


Figure 5.27 IPGTT and responsiveness. (a) *In vivo* glucose tolerance test toward diabetic mice at one-hour post-treatment of MN-(G+C+I) or subcutaneously injected with insulin. Healthy mice were used as the control. (b) Responsiveness was calculated based on the area under the curve (AUC) in 120 min, with the baseline set at the 0-min blood glucose reading. Data points represent mean \pm SD ($n = 5$). $**P < 0.01$ (analyzed by one-way ANOVA) for MN-(G+C+I) compared with control groups.

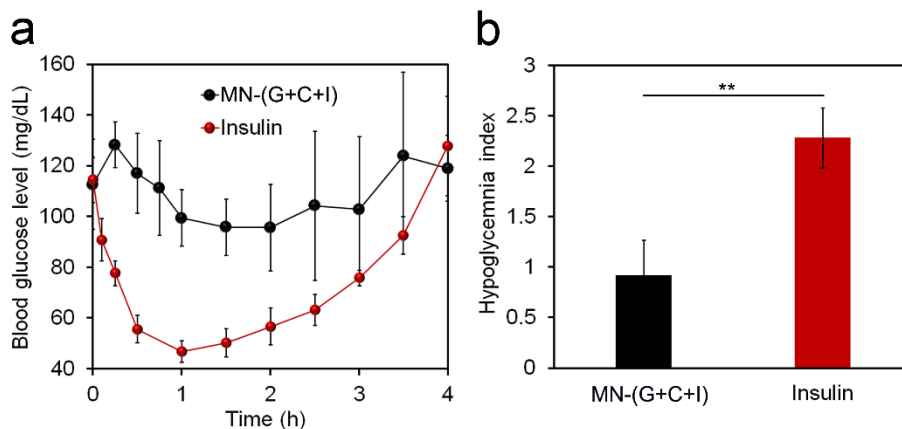


Figure 5.28 Hypoglycemic test of MN on healthy mice. (a) Blood glucose levels change of healthy mice treated with MN array patch or subcutaneously injected insulin. The treatment was given at 0 min. (b) Quantification of the hypoglycemia index, identified as the difference between the initial and nadir blood glucose readings divided by the time at which nadir was reached. Data points represent mean \pm SD (n = 5). ** $P < 0.01$ (analyzed by two-tailed Student's *t*-test) for MN-(G+C+I) compared with the insulin-treated group.

Importantly, the matrix materials used for insulin delivery have shown negligible *in vitro* cytotoxicity (Figure 5.29). For *in vivo* toxicity, compared to the skin tissues treated by MN-Gel (Figure 5.26c), a clear damage of skin tissue was observed for MN-(G+I). In sharp contrast, only negligible inflammation was observed on the skin of mice treated with MN-(G+C+I) due to the presence of a CAT-embedded sheath (Figure 5.26c). These findings were further validated by hematoxylin and eosin (H&E) staining results. Compared with the skin treated with MN-Gel (Figure 5.30), the skin samples treated with MN-(G+I) (Figure 5.30) were significantly thicker and showed apparent neutrophil infiltration, indicating a pathophysiological response and tissue damage induced by H_2O_2 .²¹² However, reduced neutrophil infiltration was observed in skin samples from mice treated with MN-(G+C+I) (Figure 5.26d). Additionally, the skin tissue stained with the *in situ* terminal deoxynucleotidyl transferase deoxyuridine triphosphate (dUTP) nick end labeling (TUNEL) assay clearly demonstrated the negligible cell apoptosis in the skin sample treated with MN-(G+C+I) as

compared to that associated with the control group (Figure 5.26d and 5.30). Accordingly, the counts of white blood cells from mice treated by MN-(G+C+I) were similar to that of the healthy mice (Figure 5.26e). For the long-term usage, the frequent exposure of skin tissues to the leaking H₂O₂ could cause some side effects. However, with the optimization of the ratio of CAT and GOx, as well as regular change of the MN administration position, the side effects toward skin could be minimized for daily usage.

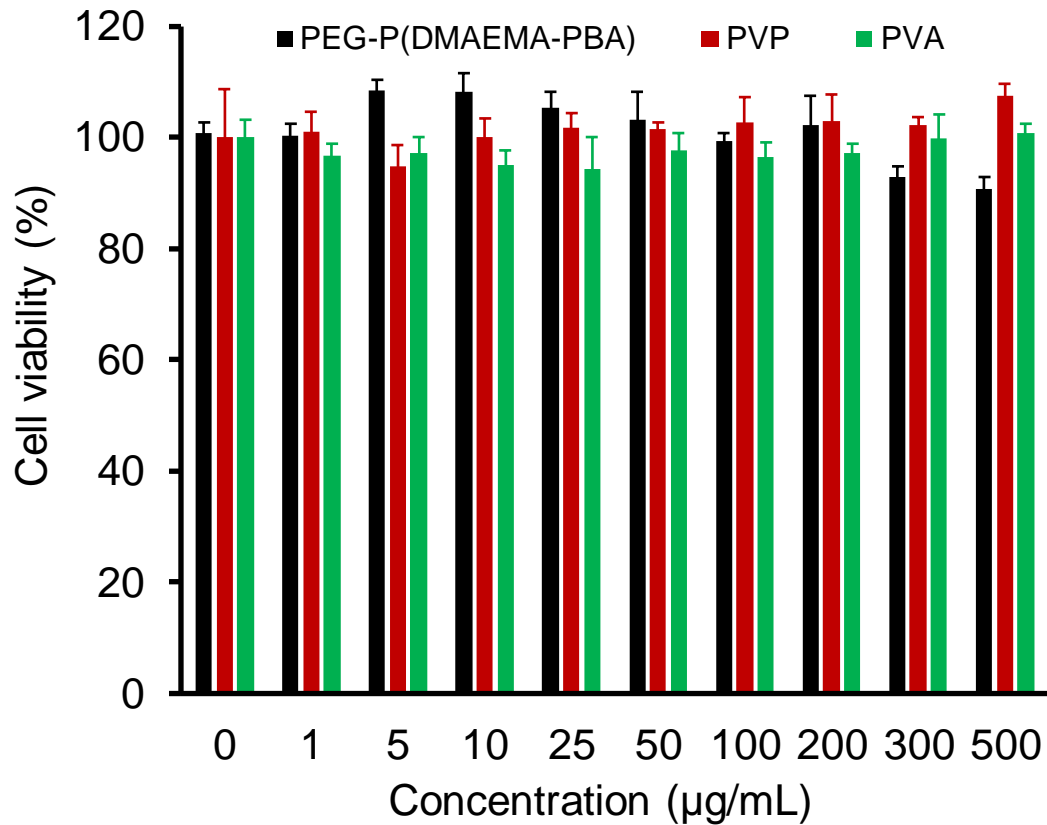


Figure 5.29 Cytotoxicity evaluation of the matrix materials utilized in this study toward HeLa cell.

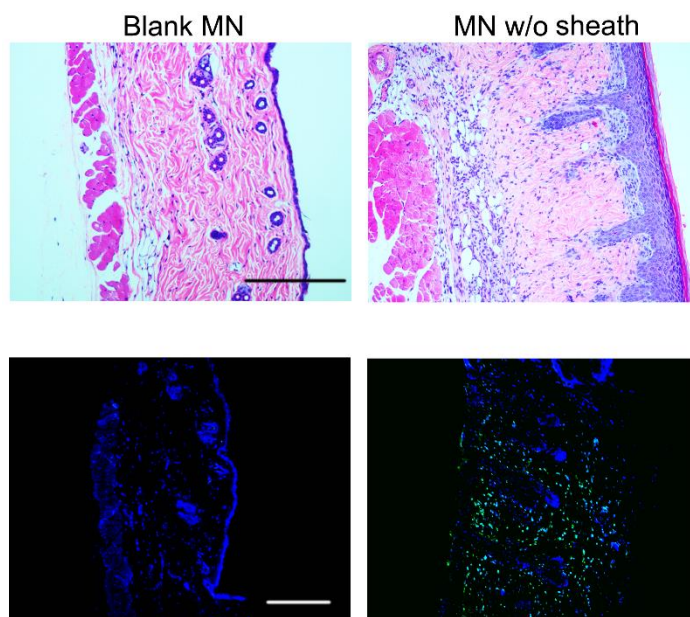


Figure 5.30 H&E staining and immunohistologic staining results of skins treated by blank MN and MN-(G+I). Scale bar: 300 μm .

5.4 Conclusion

In summary, we have developed a new MN-array patch with a sheath structure, loaded with dual sequential stimuli-responsive nanocomplex micelles for self-regulated insulin delivery. It was demonstrated that this patch could rapidly and safely release insulin triggered by locally generated H_2O_2 and an acidic microenvironment under a hyperglycemic condition. *In vivo* experiments indicated that the MN-(G+C+I) was effective in regulating BGLs under a normoglycemic state while reducing the risk of hypoglycemia. Importantly, utilization of CAT sheath-like coating significantly mitigated the skin inflammation caused by the production of H_2O_2 .

CHAPTER 6 SUMMARY AND OUTLOOK

In this dissertation, we have reviewed recent advances in the development of bioresponsive transdermal drug delivery systems based on microneedle (MN) patches by leveraging physiological signals associated with diseases or skin-specific tissues. Four individual projects based on transcutaneous patches of arrayed MNs were specifically introduced for the smart drug delivery to treat several diseases including thromboembolism, obesity, acne, and diabetes.

In this chapter, we will summarize each project as following:

- 1) We developed a thrombin-responsive patch for auto-regulation of blood coagulation by integrating thrombin-sensitive heparin-hyaluronic acid matrix with MN-arrays. The MNs can sense the activated thrombin and subsequently release heparin to prevent coagulation in the blood flow. The *in vivo* studies in a thrombolytic challenge mouse model demonstrated effective long-term prevention from the acute pulmonary thromboembolism. In addition, contributed to MN array patch, we obtained 1) fast response; 2) ease of administration; 3) sustained action time and 4) biocompatibility without long-term side effects. This work might open up a platform for the application of closed-loop based drug delivery on the treatment of intravascular diseases.
- 2) We have developed a technique based on a nanoparticles-integrated MN patch that enables local browning of white adipose tissue (WAT). The degradable NPs released browning agents into the subcutaneous region in the presence of glucose and promoted the transformation of WAT towards the brown-like adipose tissue. More importantly, MNs restricted the browning reagents in the treated region and thus are expected to minimize

potential side effects of browning reagents on other organs if administered orally or intravenously. The *in vivo* data further demonstrated systemically increase of energy expenditure and fatty acid oxidation, effective body weight control in diet-induced obese mice, as well as improved insulin sensitivity. Taken together, this work provides a new strategy in applying drugs through MN as potential therapeutics for the clinical treatment of obesity and its comorbidities such as type-2 diabetes.

- 3) We have generated a reactive oxygen species (ROS)-responsive MN patch to effectively deliver antibiotic into dermis for enhancing acne treatment. Unlike the traditional anti-acne cream, the drug-loaded MNs are able to penetrate stratum corneum to improve the drug interaction against *P. acnes*. Meanwhile, the inflammation-mediated sustained drug release continuously keeps a sufficient drug concentration in the therapeutic levels around acne area. A hyaluronic acid/diatomaceous earth contained substrate of the patch can also absorb the pus and dead cell debris to accelerate the healing of skin. This biosignal-responsive MN patch-based strategy can also be extended to enhance the therapeutic efficiency for the treatment of various other skin diseases.

- 4) We have developed a MN-array patch with a sheath structure, loaded with dual sequential stimuli-responsive nano-complex micelles for self-regulated insulin delivery. It was demonstrated that this patch could rapidly and safely release insulin triggered by locally generated H₂O₂ and an acidic microenvironment under a hyperglycemic condition. *In vivo* experiments indicated that this patch was effective in regulating blood glucose levels under a normoglycemic state while reducing the risk of hypoglycemia. Importantly, utilization of

catalase sheath-like coating significantly mitigated the skin inflammation caused by the production of H₂O₂.

In these four projects, we demonstrated several different applications of bioresponsive drug delivery devices based on transcutaneous patches for the treatment of different diseases. The aim of this study was to design and evaluate the pre-clinical concept for the further translation. To realize this goal, some limitations associated with long-term use, delivery efficiency, and reliability should be overcome to improve the performance of the devices. The relationship between the relevant physiological signals and required drug dosage needs a close investigation to achieve on-demand drug release, thus preventing under- or over-dosing. In addition, pharmacokinetics should also be characterized to determine the transport efficiency by MN patches in different patients or in different skin sites within the same patient. Further experiment associated with transdermal patches should be performed to evaluate the short- and long-term side effects, and the potential risk of irritation and inflammation must also be assessed in clinical studies. Finally, identifying new biosignals associated with diseases and thus designing relevant monitor/actuator pairs is significant for the development of bioresponsive MN-based drug delivery systems.

REFERENCES

1. Prausnitz, M. R.; Langer, R., Transdermal drug delivery. *Nat. Biotechnol.* **2008**, *26* (11), 1261-1268.
2. Kim, Y.-C.; Park, J.-H.; Prausnitz, M. R., Microneedles for drug and vaccine delivery. *Adv. Drug Del. Rev.* **2012**, *64* (14), 1547-1568.
3. Quinn, H. L.; Kearney, M.-C.; Courtenay, A. J.; McCrudden, M. T.; Donnelly, R. F., The role of microneedles for drug and vaccine delivery. *Expert. Opin. Drug Deliv.* **2014**, *11* (11), 1769-1780.
4. Kim, Y.-C.; Prausnitz, M. R., Enabling skin vaccination using new delivery technologies. *Drug Deliv. Transl. Res.* **2011**, *1* (1), 7-12.
5. Hoffmann, C.; Buchholz, L.; Schnitzler, P., Reduction of needlestick injuries in healthcare personnel at a university hospital using safety devices. *J. Occup. Med. Toxicol.* **2013**, *8* (1), 20.
6. Larrañeta, E.; McCrudden, M. T.; Courtenay, A. J.; Donnelly, R. F., Microneedles: a new frontier in nanomedicine delivery. *Pharm. Res.* **2016**, *33* (5), 1055-1073.
7. Suh, H.; Shin, J.; Kim, Y.-C., Microneedle patches for vaccine delivery. *Clin. Exp. Vaccine Res.* **2014**, *3* (1), 42-49.
8. Donnelly, R. F.; Singh, T. R. R.; Morrow, D. I.; Woolfson, A. D., *Microneedle-mediated transdermal and intradermal drug delivery*. John Wiley & Sons: 2012.
9. SHINGADE, G., Review on: recent trend on transdermal drug delivery system. *JDDT* **2012**, *2* (1), 66-75.
10. Cheung, K.; Das, D. B., Microneedles for drug delivery: trends and progress. *Drug Deliv.* **2016**, *23* (7), 2338-2354.

11. Rejinold, N. S.; Shin, J.-H.; Seok, H. Y.; Kim, Y.-C., Biomedical applications of microneedles in therapeutics: recent advancements and implications in drug delivery. *Expert. Opin. Drug Deliv.* **2016**, *13* (1), 109-131.
12. Cahill, E. M.; O’Cearbhaill, E. D., Toward biofunctional microneedles for stimulus responsive drug delivery. *Bioconj. Chem.* **2015**, *26* (7), 1289-1296.
13. Li, N.; Wang, N.; Wang, X.; Zhen, Y.; Wang, T., Microneedle arrays delivery of the conventional vaccines based on nonvirulent viruses. *Drug Deliv.* **2016**, *23* (9), 3234-3247.
14. Yun, J.; Im, J. S.; Lee, Y.-S.; Kim, H.-I., Electro-responsive transdermal drug delivery behavior of PVA/PAA/MWCNT nanofibers. *Eur. Polym. J.* **2011**, *47* (10), 1893-1902.
15. Alexander, A.; Dwivedi, S.; Giri, T. K.; Saraf, S.; Saraf, S.; Tripathi, D. K., Approaches for breaking the barriers of drug permeation through transdermal drug delivery. *J. Controlled Release* **2012**, *164* (1), 26-40.
16. Hardy, J. G.; Larraneta, E.; Donnelly, R. F.; McGoldrick, N.; Migalska, K.; McCrudden, M. T.; Irwin, N. J.; Donnelly, L.; McCoy, C. P., Hydrogel-forming microneedle arrays made from light-responsive materials for on-demand transdermal drug delivery. *Mol. Pharm.* **2016**, *13* (3), 907-914.
17. Chen, M.-C.; Ling, M.-H.; Wang, K.-W.; Lin, Z.-W.; Lai, B.-H.; Chen, D.-H., Near-infrared light-responsive composite microneedles for on-demand transdermal drug delivery. *Biomacromolecules* **2015**, *16* (5), 1598-1607.
18. Di, J.; Yao, S.; Ye, Y.; Cui, Z.; Yu, J.; Ghosh, T. K.; Zhu, Y.; Gu, Z., Stretch-triggered drug delivery from wearable elastomer films containing therapeutic depots. *ACS Nano* **2015**, *9* (9), 9407-9415.

19. Lu, Y.; Sun, W.; Gu, Z., Stimuli-responsive nanomaterials for therapeutic protein delivery. *J. Controlled Release* **2014**, *194*, 1-19.
20. Yu, J.; Zhang, Y.; Ye, Y.; DiSanto, R.; Sun, W.; Ranson, D.; Ligler, F. S.; Buse, J. B.; Gu, Z., Microneedle-array patches loaded with hypoxia-sensitive vesicles provide fast glucose-responsive insulin delivery. *Proc. Natl. Acad. Sci. U.S.A.* **2015**, *112* (27), 8260-8265.
21. Schmid-Wendtner, M.-H.; Korting, H. C., The pH of the skin surface and its impact on the barrier function. *Skin Pharmacol. Physiol.* **2006**, *19* (6), 296-302.
22. Giusti, F.; Martella, A.; Bertoni, L.; Seidenari, S., Skin barrier, hydration, and pH of the skin of infants under 2 years of age. *Pediatr. Dermatol.* **2001**, *18* (2), 93-96.
23. Ke, C.-J.; Lin, Y.-J.; Hu, Y.-C.; Chiang, W.-L.; Chen, K.-J.; Yang, W.-C.; Liu, H.-L.; Fu, C.-C.; Sung, H.-W., Multidrug release based on microneedle arrays filled with pH-responsive PLGA hollow microspheres. *Biomaterials* **2012**, *33* (20), 5156-5165.
24. Van der Maaden, K.; Yu, H.; Sliedregt, K.; Zwier, R.; Leboux, R.; Oguri, M.; Kros, A.; Jiskoot, W.; Bouwstra, J. A., Nanolayered chemical modification of silicon surfaces with ionizable surface groups for pH-triggered protein adsorption and release: application to microneedles. *J. Mater. Chem. B* **2013**, *1* (35), 4466-4477.
25. Kim, N. W.; Lee, M. S.; Kim, K. R.; Lee, J. E.; Lee, K.; Park, J. S.; Matsumoto, Y.; Jo, D.-G.; Lee, H.; Lee, D. S.; Jeong, J. H., Polyplex-releasing microneedles for enhanced cutaneous delivery of DNA vaccine. *J. Controlled Release* **2014**, *179*, 11-17.
26. Van der Maaden, K.; Sekerdag, E.; Schipper, P.; Kersten, G.; Jiskoot, W.; Bouwstra, J., Layer-by-layer assembly of inactivated poliovirus and N-trimethyl chitosan on pH-sensitive microneedles for dermal vaccination. *Langmuir* **2015**, *31* (31), 8654-8660.

27. Harvey, A. J.; Kaestner, S. A.; Sutter, D. E.; Harvey, N. G.; Mikszta, J. A.; Pettis, R. J., Microneedle-based intradermal delivery enables rapid lymphatic uptake and distribution of protein drugs. *Pharm. Res.* **2011**, *28* (1), 107-116.
28. Veiseh, O.; Tang, B. C.; Whitehead, K. A.; Anderson, D. G.; Langer, R., Managing diabetes with nanomedicine: challenges and opportunities. *Nat. Rev. Drug Discov.* **2015**, *14* (1), 45-57.
29. Mo, R.; Jiang, T.; Di, J.; Tai, W.; Gu, Z., Emerging micro-and nanotechnology based synthetic approaches for insulin delivery. *Chem. Soc. Rev.* **2014**, *43* (10), 3595-3629.
30. Ye, Y.; Yu, J.; Wang, C.; Nguyen, N. Y.; Walker, G. M.; Buse, J. B.; Gu, Z., Microneedles Integrated with Pancreatic Cells and Synthetic Glucose-Signal Amplifiers for Smart Insulin Delivery. *Adv. Mater.* **2016**, *28* (16), 3115-3121.
31. Hu, X.; Yu, J.; Qian, C.; Lu, Y.; Kahkoska, A. R.; Xie, Z.; Jing, X.; Buse, J. B.; Gu, Z., H₂O₂-Responsive Vesicles Integrated with Transcutaneous Patches for Glucose-Mediated Insulin Delivery. *ACS Nano* **2017**, *11* (1), 613-620.
32. Yu, J.; Qian, C.; Zhang, Y.; Cui, Z.; Zhu, Y.; Shen, Q.; Ligler, F. S.; Buse, J. B.; Gu, Z., Hypoxia and H₂O₂ Dual-Sensitive Vesicles for Enhanced Glucose-Responsive Insulin Delivery. *Nano Lett.* **2017**, *17* (2), 733-739.
33. Wang, C.; Ye, Y.; Hochu, G. M.; Sadeghifar, H.; Gu, Z., Enhanced Cancer Immunotherapy by Microneedle Patch-Assisted Delivery of Anti-PD1 Antibody. *Nano Lett.* **2016**, *16* (4), 2334-2340.
34. Chung, J. E.; Tan, S.; Gao, S. J.; Yongvongsoontorn, N.; Kim, S. H.; Lee, J. H.; Choi, H. S.; Yano, H.; Zhuo, L.; Kurisawa, M.; Ying, J. Y., Self-assembled micellar

- nanocomplexes comprising green tea catechin derivatives and protein drugs for cancer therapy. *Nat. Nanotechnol.* **2014**, *9* (11), 907-912.
35. De La Rica, R.; Aili, D.; Stevens, M. M., Enzyme-responsive nanoparticles for drug release and diagnostics. *Adv. Drug Del. Rev.* **2012**, *64* (11), 967-978.
 36. Stern, R., Hyaluronan metabolism: a major paradox in cancer biology. *Pathol. Biol.* **2005**, *53* (7), 372-382.
 37. Ye, Y.; Wang, J.; Hu, Q.; Hochu, G. M.; Xin, H.; Wang, C.; Gu, Z., Synergistic transcutaneous immunotherapy enhances antitumor immune responses through delivery of checkpoint inhibitors. *ACS Nano* **2016**, *10* (9), 8956-8963.
 38. Zhang, Y.; Yu, J.; Wang, J.; Hanne, N. J.; Cui, Z.; Qian, C.; Wang, C.; Xin, H.; Cole, J. H.; Gallippi, C. M., Thrombin-Responsive Transcutaneous Patch for Auto-Anticoagulant Regulation. *Adv. Mater.* **2017**, *29* (4).
 39. Lu, Y.; Aimetti, A. A.; Langer, R.; Gu, Z., Bioresponsive materials. *Nat. Rev. Mater.* **2016**, *1*, 16075.
 40. Pisal, D. S.; Kosloski, M. P.; Balu - Iyer, S. V., Delivery of therapeutic proteins. *J. Pharm. Sci.* **2010**, *99* (6), 2557-2575.
 41. Du, A. W.; Stenzel, M. H., Drug carriers for the delivery of therapeutic peptides. *Biomacromolecules* **2014**, *15* (4), 1097-1114.
 42. Torchilin, V. P., Multifunctional, stimuli-sensitive nanoparticulate systems for drug delivery. *Nat. Rev. Drug Discov.* **2014**, *13* (11), 813-827.
 43. Mackman, N., Triggers, targets and treatments for thrombosis. *Nature* **2008**, *451* (7181), 914-918.

44. Geerts, W. H.; Bergqvist, D.; Pineo, G. F.; Heit, J. A.; Samama, C. M.; Lassen, M. R.; Colwell, C. W., Prevention of venous thromboembolism. *Chest* **2008**, *133* (6 Suppl), 381S-453S.
45. Engelmann, B.; Massberg, S., Thrombosis as an intravascular effector of innate immunity. *Nat. Rev. Immunol.* **2013**, *13* (1), 34-45.
46. Doshi, N.; Orje, J. N.; Molins, B.; Smith, J. W.; Mitragotri, S.; Ruggeri, Z. M., Platelet mimetic particles for targeting thrombi in flowing blood. *Adv. Mater.* **2012**, *24* (28), 3864-3869.
47. Hu, Q.; Qian, C.; Sun, W.; Wang, J.; Chen, Z.; Bomba, H. N.; Xin, H.; Shen, Q.; Gu, Z., Engineered Nanoplatelets for Enhanced Treatment of Multiple Myeloma and Thrombus. *Adv. Mater.* **2016**, *28* (43), 9573-9580.
48. Mannucci, P. M.; Franchini, M., Old and new anticoagulant drugs: a minireview. *Ann. Med.* **2011**, *43* (2), 116-123.
49. Collins, R.; Scrimgeour, A.; Yusuf, S.; Peto, R., Reduction in fatal pulmonary embolism and venous thrombosis by perioperative administration of subcutaneous heparin. *New Engl. J. Med.* **1988**, *318* (18), 1162-1173.
50. Jin, L.; Abrahams, J. P.; Skinner, R.; Petitou, M.; Pike, R. N.; Carrell, R. W., The anticoagulant activation of antithrombin by heparin. *Proc. Natl. Acad. Sci. U.S.A.* **1997**, *94* (26), 14683-14688.
51. Cohen, M.; Demers, C.; Gurfinkel, E. P.; Turpie, A. G.; Fromell, G. J.; Goodman, S.; Langer, A.; Califf, R. M.; Fox, K. A.; Premmreur, J., A comparison of low-molecular-weight heparin with unfractionated heparin for unstable coronary artery disease. *New Engl. J. Med.* **1997**, *337* (7), 447-452.

52. Moscucci, M., Frequency and costs of ischemic and bleeding complications after percutaneous coronary interventions. *J. Invasive Cardiol.* **2002**, *14* (SUPPL. B).
53. Prandoni, P.; Lensing, A. W.; Piccioli, A.; Bernardi, E.; Simioni, P.; Girolami, B.; Marchiori, A.; Sabbion, P.; Prins, M. H.; Noventa, F., Recurrent venous thromboembolism and bleeding complications during anticoagulant treatment in patients with cancer and venous thrombosis. *Blood* **2002**, *100* (10), 3484-3488.
54. Davies, M. J.; Thomas, A., Thrombosis and acute coronary-artery lesions in sudden cardiac ischemic death. *New Engl. J. Med.* **1984**, *310* (18), 1137-1140.
55. Korin, N.; Kanapathipillai, M.; Matthews, B. D.; Crescente, M.; Brill, A.; Mammoto, T.; Ghosh, K.; Jurek, S.; Bencherif, S. A.; Bhatta, D., Shear-activated nanotherapeutics for drug targeting to obstructed blood vessels. *Science* **2012**, *337* (6095), 738-742.
56. Chen, C.; Li, S.; Liu, K.; Ma, G.; Yan, X., Co-Assembly of Heparin and Polypeptide Hybrid Nanoparticles for Biomimetic Delivery and Anti-Thrombus Therapy. *Small* **2016**, *12* (34), 4719-4725.
57. Maitz, M. F.; Freudenberg, U.; Tsurkan, M. V.; Fischer, M.; Beyrich, T.; Werner, C., Bio-responsive polymer hydrogels homeostatically regulate blood coagulation. *Nat. Commun.* **2013**, *4*.
58. Dahlbäck, B., Blood coagulation. *Lancet* **2000**, *355* (9215), 1627-1632.
59. Bhat, R.; Ribes, À.; Mas, N.; Aznar, E.; Sancenón, F.; Marcos, M. D.; Murguía, J. R.; Venkataraman, A.; Martínez-Mañez, R., Thrombin-responsive gated silica mesoporous nanoparticles as coagulation regulators. *Langmuir* **2016**, *32* (5), 1195-1200.

60. Argyo, C.; Cauda, V.; Engelke, H.; Rädler, J.; Bein, G.; Bein, T., Heparin-Coated Colloidal Mesoporous Silica Nanoparticles Efficiently Bind to Antithrombin as an Anticoagulant Drug-Delivery System. *Chem. Eur. J.* **2012**, *18* (2), 428-432.
61. Kogan, G.; Šoltés, L.; Stern, R.; Gemeiner, P., Hyaluronic acid: a natural biopolymer with a broad range of biomedical and industrial applications. *Biotechnol. Lett.* **2007**, *29* (1), 17-25.
62. CHANG, J. Y., Thrombin specificity. *Eur. J. Biochem.* **1985**, *151* (2), 217-224.
63. Jenny, R. J.; Mann, K. G.; Lundblad, R. L., A critical review of the methods for cleavage of fusion proteins with thrombin and factor Xa. *Protein Expression Purif.* **2003**, *31* (1), 1-11.
64. Sullivan, S. P.; Koutsonanos, D. G.; del Pilar Martin, M.; Lee, J. W.; Zarnitsyn, V.; Choi, S.-O.; Murthy, N.; Compans, R. W.; Skountzou, I.; Prausnitz, M. R., Dissolving polymer microneedle patches for influenza vaccination. *Nat. Med.* **2010**, *16* (8), 915-920.
65. DeMuth, P. C.; Min, Y.; Huang, B.; Kramer, J. A.; Miller, A. D.; Barouch, D. H.; Hammond, P. T.; Irvine, D. J., Polymer multilayer tattooing for enhanced DNA vaccination. *Nat. Mater.* **2013**, *12* (4), 367-376.
66. Donnelly, R. F.; Singh, T. R. R.; Garland, M. J.; Migalska, K.; Majithiya, R.; McCrudden, C. M.; Kole, P. L.; Mahmood, T. M. T.; McCarthy, H. O.; Woolfson, A. D., Hydrogel-forming microneedle arrays for enhanced transdermal drug delivery. *Adv. Funct. Mater.* **2012**, *22* (23), 4879-4890.
67. Jiang, T.; Mo, R.; Bellotti, A.; Zhou, J.; Gu, Z., Gel-liposome-mediated co-delivery of anticancer membrane-associated proteins and small-molecule drugs for enhanced therapeutic efficacy. *Adv. Funct. Mater.* **2014**, *24* (16), 2295-2304.

68. Gresele, P.; Corona, C.; Alberti, P.; Nenci, G. G., Picotamide protects mice from death in a pulmonary embolism model by a mechanism independent from thromboxane suppression. *Thromb. Haemost.* **1990**, *64* (1), 80-86.
69. Momi, S.; Nenci, G.; Gresele, P., Thrombin-induced thromboembolism in mice: a model for testing antithrombotic agents acting on coagulation/fibrinolysis. *Thromb. Res.* **1992**, *65*, S162.
70. Paul, W.; Gresele, P.; Momi, S.; Bianchi, G.; Page, C., The effect of defibrotide on thromboembolism in the pulmonary vasculature of mice and rabbits and in the cerebral vasculature of rabbits. *Br. J. Pharmacol.* **1993**, *110* (4), 1565-1571.
71. Basu, D.; Gallus, A.; Hirsh, J.; Cade, J., A prospective study of the value of monitoring heparin treatment with the activated partial thromboplastin time. *New Engl. J. Med.* **1972**, *287* (7), 324-327.
72. Eikelboom, J. W.; Hirsh, J., Monitoring unfractionated heparin with the aPTT: time for a fresh look. *Thromb. Haemost.* **2006**, *96* (5), 547-52.
73. Quick, A. J., The prothrombin in hemophilia and in obstructive jaundice. *J. Biol. Chem.* **1935**, *109* (1), xxiii-xxiv.
74. Rosenberg, R. D., Actions and interactions of antithrombin and heparin. *New Engl. J. Med.* **1975**, *292* (3), 146-151.
75. Damus, P. S.; Hicks, M.; Rosenberg, R. D., Anticoagulant action of heparin. *Nature* **1973**, *246*, 355.
76. Sheehan, J. P.; Sadler, J. E., Molecular mapping of the heparin-binding exosite of thrombin. *Proc. Natl. Acad. Sci. U.S.A.* **1994**, *91* (12), 5518-5522.
77. Hirsh, J., Heparin. *New Engl. J. Med.* **1991**, *324* (22), 1565-1574.

78. Rosenberg, R. D., Biochemistry of heparin antithrombin interactions, and the physiologic role of this natural anticoagulant mechanism. *Am. J. Med.* **1989**, *87* (3), S2-S9.
79. Ignjatovic, V., Thrombin clotting time. *Haemostasis: Methods Protoc.* **2013**, 131-138.
80. Boisclair, M.; Lane, D.; Philippou, H.; Sheikh, S.; Hunt, B., Thrombin production, inactivation and expression during open heart surgery measured by assays for activation fragments including a new ELISA for prothrombin fragment F1+ 2. *Thromb. Haemost.* **1993**, *70* (2), 253-258.
81. Momi, S.; Nasimi, M.; Colucci, M.; Nenci, G. G.; Gresele, P., Low molecular weight heparins prevent thrombin-induced thrombo-embolism in mice despite low anti-thrombin activity. Evidence that the inhibition of feed-back activation of thrombin generation confers safety advantages over direct thrombin inhibition. *Haematologica* **2001**, *86* (3), 297-302.
82. Hirsh, J.; Van Aken, W.; Gallus, A.; Dollery, C.; Cade, J.; Yung, W., Heparin kinetics in venous thrombosis and pulmonary embolism. *Circulation* **1976**, *53* (4), 691-695.
83. Brummel, K. E.; Paradis, S. G.; Butenas, S.; Mann, K. G., Thrombin functions during tissue factor-induced blood coagulation. *Blood* **2002**, *100* (1), 148-152.
84. Comer, M.; Cackett, K.; Gladwell, S.; Wood, L.; Dawson, K., Thrombolytic activity of BB - 10153, a thrombin - activatable plasminogen. *J. Thromb. Haemost.* **2005**, *3* (1), 146-153.
85. Organization, W. H., Obesity and overweight. Fact sheet No 311. 2015. *Google Scholar* **2015**.
86. Ogden, C. L.; Carroll, M. D.; Fryar, C. D.; Flegal, K. M., Prevalence of obesity among adults and youth: United States, 2011–2014. *NCHS data brief* **2015**, *219* (219), 1-8.

87. Friedman, J. M., Obesity: Causes and control of excess body fat. *Nature* **2009**, *459* (7245), 340-342.
88. Heymsfield, S. B.; Wadden, T. A., Mechanisms, pathophysiology, and management of obesity. *New Engl. J. Med.* **2017**, *376* (3), 254-266.
89. Rucker, D.; Padwal, R.; Li, S. K.; Curioni, C.; Lau, D. C., Long term pharmacotherapy for obesity and overweight: updated meta-analysis. *BMJ* **2007**.
90. Dietrich, M. O.; Horvath, T. L., Limitations in anti-obesity drug development: the critical role of hunger-promoting neurons. *Nat. Rev. Drug Discov.* **2012**, *11* (9), 675-691.
91. Chang, S.-H.; Stoll, C. R.; Song, J.; Varela, J. E.; Eagon, C. J.; Colditz, G. A., The effectiveness and risks of bariatric surgery: an updated systematic review and meta-analysis, 2003-2012. *JAMA surgery* **2014**, *149* (3), 275-287.
92. Wu, J.; Cohen, P.; Spiegelman, B. M., Adaptive thermogenesis in adipocytes: Is beige the new brown? *Genes Dev.* **2013**, *27* (3), 234-250.
93. Au-Yong, I. T.; Thorn, N.; Ganatra, R.; Perkins, A. C.; Symonds, M. E., Brown adipose tissue and seasonal variation in humans. *Diabetes* **2009**, *58* (11), 2583-2587.
94. Kajimura, S.; Spiegelman, B. M.; Seale, P., Brown and beige fat: physiological roles beyond heat generation. *Cell Metab.* **2015**, *22* (4), 546-559.
95. Harms, M.; Seale, P., Brown and beige fat: development, function and therapeutic potential. *Nat. Med.* **2013**, *19* (10), 1252-1263.
96. Bartelt, A.; Heeren, J., Adipose tissue browning and metabolic health. *Nat. Rev. Endocrinol.* **2014**, *10* (1), 24-36.

97. Xue, Y.; Xu, X.; Zhang, X.-Q.; Farokhzad, O. C.; Langer, R., Preventing diet-induced obesity in mice by adipose tissue transformation and angiogenesis using targeted nanoparticles. *Proc. Natl. Acad. Sci. U.S.A.* **2016**, 201603840.
98. Bonet, M. L.; Oliver, P.; Palou, A., Pharmacological and nutritional agents promoting browning of white adipose tissue. *Biochim. Biophys. Acta, Mol. Cell. Biol. Lipids* **2013**, 1831 (5), 969-985.
99. Clapham, J. C.; Arch, J. R.; Tadayyon, M., Anti-obesity drugs: a critical review of current therapies and future opportunities. *Pharmacol. Ther.* **2001**, 89 (1), 81-121.
100. Whittle, A.; Relat-Pardo, J.; Vidal-Puig, A., Pharmacological strategies for targeting BAT thermogenesis. *Trends Pharmacol. Sci.* **2013**, 34 (6), 347-355.
101. Colman, E.; Golden, J.; Roberts, M.; Egan, A.; Weaver, J.; Rosebraugh, C., The FDA's assessment of two drugs for chronic weight management. *New Engl. J. Med.* **2012**, 367 (17), 1577-1579.
102. Nedergaard, J.; Cannon, B., The browning of white adipose tissue: some burning issues. *Cell Metab.* **2014**, 20 (3), 396-407.
103. Cai, X.; Jia, X.; Gao, W.; Zhang, K.; Ma, M.; Wang, S.; Zheng, Y.; Shi, J.; Chen, H., A Versatile Nanotheranostic Agent for Efficient Dual-Mode Imaging Guided Synergistic Chemo-Thermal Tumor Therapy. *Adv. Funct. Mater.* **2015**, 25 (17), 2520-2529.
104. Gu, Z.; Aimetti, A. A.; Wang, Q.; Dang, T. T.; Zhang, Y.; Veisoh, O.; Cheng, H.; Langer, R. S.; Anderson, D. G., Injectable nano-network for glucose-mediated insulin delivery. *ACS Nano* **2013**, 7 (5), 4194-4201.
105. Bakopanos, E.; Silva, J. E., Thiazolidinediones inhibit the expression of beta3-adrenergic receptors at a transcriptional level. *Diabetes* **2000**, 49 (12), 2108-2115.

106. Cipolletta, D.; Feuerer, M.; Li, A.; Kamei, N.; Lee, J.; Shoelson, S. E.; Benoist, C.; Mathis, D., PPAR- γ is a major driver of the accumulation and phenotype of adipose tissue Treg cells. *Nature* **2012**, *486* (7404), 549-553.
107. Yu, J.; Zhang, Y.; Bomba, H.; Gu, Z., Stimuli-Responsive Delivery of Therapeutics for Diabetes Treatment. *Bioeng. Transl. Med.* **2016**, *1*, 323-337.
108. Yuqi, Z.; Jicheng, Y.; Qundong, S.; Zhen, G., Glucose-responsive synthetic closed-loop insulin delivery systems. *Prog. Chem.* **2015**, *27* (1), 11-26.
109. Li, D.; Zhang, F.; Zhang, X.; Xue, C.; Namwanje, M.; Fan, L.; Reilly, M. P.; Hu, F.; Qiang, L., Distinct functions of PPAR γ isoforms in regulating adipocyte plasticity. *Biochem. Biophys. Res. Commun.* **2016**, *481* (1), 132-138.
110. Vernochet, C.; Peres, S. B.; Davis, K. E.; McDonald, M. E.; Qiang, L.; Wang, H.; Scherer, P. E.; Farmer, S. R., C/EBP α and the corepressors CtBP1 and CtBP2 regulate repression of select visceral white adipose genes during induction of the brown phenotype in white adipocytes by peroxisome proliferator-activated receptor γ agonists. *Mol. Cell. Biol.* **2009**, *29* (17), 4714-4728.
111. Lowell, M., PhD, BB; Flier, M., JS, Brown adipose tissue, β 3-adrenergic receptors, and obesity. *Annu. Rev. Med.* **1997**, *48* (1), 307-316.
112. Weyer, C.; Gautier, J.; Danforth Jr, E., Development of Beta 3-Adrenoceptor Agonists for the Treatment of Obesity and Diabetes An Update. *Diabetes Metab.* **1999**, *25*, 11-21.
113. Weyer, C.; de Souza, C. J., Development of β 3 - adrenoceptor agonists as antiobesity and antidiabetes drugs in humans: Current status and future prospects. *Drug Dev. Res.* **2000**, *51* (2), 80-93.

114. Klein, J.; Fasshauer, M.; Ito, M.; Lowell, B. B.; Benito, M.; Kahn, C. R., β 3-Adrenergic stimulation differentially inhibits insulin signaling and decreases insulin-induced glucose uptake in brown adipocytes. *J. Biol. Chem.* **1999**, *274* (49), 34795-34802.
115. Yu, S.; Gavrilova, O.; Chen, H.; Lee, R.; Liu, J.; Pacak, K.; Parlow, A.; Quon, M. J.; Reitman, M. L.; Weinstein, L. S., Paternal versus maternal transmission of a stimulatory G-protein α subunit knockout produces opposite effects on energy metabolism. *J. Clin. Invest.* **2000**, *105* (5), 615-623.
116. Voikar, V.; Polus, A.; Vasar, E.; Rauvala, H., Long-term individual housing in C57BL/6J and DBA/2 mice: assessment of behavioral consequences. *Genes, Brain and Behav.* **2005**, *4* (4), 240-252.
117. Nagy, T. R.; Krzywanski, D.; Li, J.; Meleth, S.; Desmond, R., Effect of group vs. single housing on phenotypic variance in C57BL/6J mice. *Obesity Res.* **2002**, *10* (5), 412-415.
118. Kalliokoski, O.; Jacobsen, K. R.; Darusman, H. S.; Henriksen, T.; Weimann, A.; Poulsen, H. E.; Hau, J.; Abelson, K. S., Mice do not habituate to metabolism cage housing—a three week study of male BALB/c mice. *PLoS One* **2013**, *8* (3), e58460.
119. Sun, W.; Hu, Q.; Ji, W.; Wright, G.; Gu, Z., Leveraging Physiology for Precision Drug Delivery. *Physiol. Rev.* **2017**, *97* (1), 189-225.
120. Tuchayi, S. M.; Makrantonaki, E.; Ganceviciene, R.; Dessinioti, C.; Feldman, S. R.; Zouboulis, C. C., Acne vulgaris. *Nat. Rev. Dis. Primers* **2015**, *1*, 15029.
121. Gollnick, H. P.; Finlay, A. Y.; Shear, N., Can we define acne as a chronic disease? *Am. J. Clin. Dermatol.* **2008**, *9* (5), 279-284.
122. Dreno, B.; Poli, F., Epidemiology of acne. *Dermatology* **2003**, *206* (1), 7-10.

123. Ghodsi, S. Z.; Orawa, H.; Zouboulis, C. C., Prevalence, severity, and severity risk factors of acne in high school pupils: a community-based study. *J. Invest. Dermatol.* **2009**, *129* (9), 2136-2141.
124. Zouboulis, C.; Eady, A.; Philpott, M.; Goldsmith, L.; Orfanos, C.; Cunliffe, W.; Rosenfield, R., What is the pathogenesis of acne? *Exp. Dermatol.* **2005**, *14* (2), 143-143.
125. Williams, H. C.; Dellavalle, R. P.; Garner, S., Acne vulgaris. *Lancet* **2012**, *379* (9813), 361-372.
126. Toyoda, M.; Morohashi, M., Pathogenesis of acne. *Med. Electron Microsc.* **2001**, *34* (1), 29-40.
127. Nagy, I.; Pivarcsi, A.; Kis, K.; Koreck, A.; Bodai, L.; McDowell, A.; Seltmann, H.; Patrick, S.; Zouboulis, C. C.; Kemény, L., Propionibacterium acnes and lipopolysaccharide induce the expression of antimicrobial peptides and proinflammatory cytokines/chemokines in human sebocytes. *Microb. Infect.* **2006**, *8* (8), 2195-2205.
128. Brüggemann, H.; Henne, A.; Hoster, F.; Liesegang, H.; Wiezer, A.; Strittmatter, A.; Hujer, S.; Dürre, P.; Gottschalk, G., The complete genome sequence of Propionibacterium acnes, a commensal of human skin. *Science* **2004**, *305* (5684), 671-673.
129. Voss, J. G., Acne vulgaris and free fatty acids: a review and criticism. *Arch. Dermatol.* **1974**, *109* (6), 894-898.
130. Webster, G. F.; Leyden, J. J., Characterization of serum-independent polymorphonuclear leukocyte chemotactic factors produced by Propionibacterium acnes. *Inflammation* **1980**, *4* (3), 261-269.

131. Vowels, B. R.; Yang, S.; Leyden, J. J., Induction of proinflammatory cytokines by a soluble factor of *Propionibacterium acnes*: implications for chronic inflammatory acne. *Infect. Immun.* **1995**, *63* (8), 3158-3165.
132. Kim, J., Review of the innate immune response in acne vulgaris: activation of Toll-like receptor 2 in acne triggers inflammatory cytokine responses. *Dermatology* **2005**, *211* (3), 193-198.
133. Webster, G. F., Inflammation in acne vulgaris. *J. Am. Acad. Dermatol.* **1995**, *33* (2), 247-253.
134. Jacob, C. I.; Dover, J. S.; Kaminer, M. S., Acne scarring: a classification system and review of treatment options. *J. Am. Acad. Dermatol.* **2001**, *45* (1), 109-117.
135. Zouboulis, C. C., Acne as a chronic systemic disease. *Clin. Dermatol.* **2014**, *32* (3), 389-396.
136. Yazici, K.; Baz, K.; Yazici, A.; Köktürk, A.; Tot, S.; Demirseren, D.; Buturak, V., Disease-specific quality of life is associated with anxiety and depression in patients with acne. *J. Eur. Acad. Dermatol. Venereol.* **2004**, *18* (4), 435-439.
137. Aktan, S.; Özmen, E., Anxiety, depression, and nature of acne vulgaris in adolescents. *Int. J. Dermatol.* **2000**, *39* (5), 354-357.
138. Halvorsen, J. A.; Stern, R. S.; Dalgard, F.; Thoresen, M.; Bjertness, E.; Lien, L., Suicidal ideation, mental health problems, and social impairment are increased in adolescents with acne: a population-based study. *J. Invest. Dermatol.* **2011**, *131* (2), 363-370.
139. Gollnick, H.; Schramm, M., Topical drug treatment in acne. *Dermatology* **1998**, *196* (1), 119-125.

140. Gollnick, H. P.; Krautheim, A., Topical treatment in acne: current status and future aspects. *Dermatology* **2003**, *206* (1), 29-36.
141. Thiboutot, D.; Zaenglein, A.; Weiss, J.; Webster, G.; Calvarese, B.; Chen, D., An aqueous gel fixed combination of clindamycin phosphate 1.2% and benzoyl peroxide 2.5% for the once-daily treatment of moderate to severe acne vulgaris: assessment of efficacy and safety in 2813 patients. *J. Am. Acad. Dermatol.* **2008**, *59* (5), 792-800.
142. Dreno, B.; Bettoli, V.; Ochsendorf, F.; Layton, A.; Mobacken, H.; Degreef, H., European recommendations on the use of oral antibiotics for acne. *Eur. J. Dermatol.* **2004**, *14* (6), 391-399.
143. Rademaker, M., Adverse effects of isotretinoin: a retrospective review of 1743 patients started on isotretinoin. *Australas. J. Dermatol.* **2010**, *51* (4), 248-253.
144. Crockett, S. D.; Porter, C. Q.; Martin, C. F.; Sandler, R. S.; Kappelman, M. D., Isotretinoin use and the risk of inflammatory bowel disease: a case-control study. *Am. J. Gastroenterology* **2010**, *105* (9), 1986.
145. Coenye, T.; Honraet, K.; Rossel, B.; Nelis, H., Biofilms in skin infections: Propionibacterium acnes and acne vulgaris. *Infect. Disord. Drug Targets* **2008**, *8* (3), 156-159.
146. Hecquet, C. M.; Ahmmed, G. U.; Vogel, S. M.; Malik, A. B., Role of TRPM2 channel in mediating H₂O₂-induced Ca²⁺ entry and endothelial hyperpermeability. *Circul. Res.* **2008**, *102* (3), 347-355.
147. Briganti, S.; Picardo, M., Antioxidant activity, lipid peroxidation and skin diseases. What's new. *J. Eur. Acad. Dermatol. Venereol.* **2003**, *17* (6), 663-669.

148. Akamatsu, H.; Horio, T., The possible role of reactive oxygen species generated by neutrophils in mediating acne inflammation. *Dermatology* **1998**, *196* (1), 82-85.
149. Briganti, S.; Picardo, M., Antioxidant activity, lipid peroxidation and skin diseases. What's new. *J. Eur. Acad. Dermatol. Venereol.* **2003**, *17* (6), 663-669.
150. Prausnitz, M. R., Microneedles for transdermal drug delivery. *Adv. Drug Del. Rev.* **2004**, *56* (5), 581-587.
151. Zhang, Y.; Wang, J.; Yu, J.; Wen, D.; Kahkoska, A.; Lu, Y.; Zhang, X.; Buse, J.; Gu, Z., Bioresponsive Microneedles with a Sheath Structure for H₂O₂ and pH Cascade-Triggered Insulin Delivery. *Small* **2018**, *14* (14), 1704181.
152. Zhang, Y.; Liu, Q.; Yu, J.; Yu, S.; Wang, J.; Qiang, L.; Gu, Z., Locally Induced Adipose Tissue Browning by Microneedle Patch for Obesity Treatment. *ACS Nano* **2017**, *11* (9), 9223-9230.
153. Wang, C.; Wang, J.; Zhang, X.; Yu, S.; Wen, D.; Hu, Q.; Ye, Y.; Bomba, H.; Hu, X.; Liu, Z., In situ formed reactive oxygen species-responsive scaffold with gemcitabine and checkpoint inhibitor for combination therapy. *Sci. Transl. Med.* **2018**, *10* (429), eaan3682.
154. Lookingbill, D. P.; Chalker, D. K.; Lindholm, J. S.; Katz, H. I.; Kempers, S. E.; Huerter, C. J.; Swinehart, J. M.; Schelling, D. J.; Klauda, H. C., Treatment of acne with a combination clindamycin/benzoyl peroxide gel compared with clindamycin gel, benzoyl peroxide gel and vehicle gel: combined results of two double-blind investigations. *J. Am. Acad. Dermatol.* **1997**, *37* (4), 590-595.
155. Lee, J. W.; Park, J.-H.; Prausnitz, M. R., Dissolving microneedles for transdermal drug delivery. *Biomaterials* **2008**, *29* (13), 2113-2124.

156. Al-Ghouti, M.; Khraisheh, M.; Allen, S.; Ahmad, M., The removal of dyes from textile wastewater: a study of the physical characteristics and adsorption mechanisms of diatomaceous earth. *J. Environ. Manage.* **2003**, *69* (3), 229-238.
157. Tsai, W.-T.; Lai, C.-W.; Hsien, K.-J., Characterization and adsorption properties of diatomaceous earth modified by hydrofluoric acid etching. *J. Colloid Interface Sci.* **2006**, *297* (2), 749-754.
158. Wollrich, G. W., Method of using a diatomaceous earth containing absorbent. Google Patents: 1993.
159. Umemoto, I.; Shimada, F.; Mitsuno, Y., Quick-drying pack-type face-cleansing composition. Google Patents: 1989.
160. Dulog, R. C.; Ferone, J. J.; Reisinger, B. A.; Siuta, P. B., Method for removing dead surface cells, dirt, oil, and blackheads from the skin and related compositions and articles. Google Patents: 2000.
161. Asano, Y.; Nakayama, K.; Yao, S.; Shoji, T., Cosmetic composition. Google Patents: 2008.
162. Okiel, K.; El-Sayed, M.; El-Kady, M. Y., Treatment of oil–water emulsions by adsorption onto activated carbon, bentonite and deposited carbon. *Egypt. J. Pet.* **2011**, *20* (2), 9-15.
163. Mo, R.; Jiang, T.; Di, J.; Tai, W.; Gu, Z., Emerging micro-and nanotechnology based synthetic approaches for insulin delivery. *Chem. Soc. Rev.* **2014**, *43* (10), 3595-3629.
164. Veisoh, O.; Tang, B. C.; Whitehead, K. A.; Anderson, D. G.; Langer, R., Managing diabetes with nanomedicine: challenges and opportunities. *Nat. Rev. Drug Discov.* **2015**, *14* (1), 45-57.

165. Ohkubo, Y.; Kishikawa, H.; Araki, E.; Miyata, T.; Isami, S.; Motoyoshi, S.; Kojima, Y.; Furuyoshi, N.; Shichiri, M., Intensive insulin therapy prevents the progression of diabetic microvascular complications in Japanese patients with non-insulin-dependent diabetes mellitus: a randomized prospective 6-year study. *Diabetes Res. Clin. Pract.* **1995**, *28* (2), 103-17.
166. Owens, D. R.; Zinman, B.; Bolli, G. B., Insulins today and beyond. *Lancet* **2001**, *358* (9283), 739-746.
167. Cengiz, E.; Sherr, J. L.; Weinzimer, S. A.; Tamborlane, W. V., New-generation diabetes management: glucose sensor-augmented insulin pump therapy. *Expert Rev. Med. Devices* **2011**, *8* (4), 449-58.
168. Bequette, B. W., A critical assessment of algorithms and challenges in the development of a closed-loop artificial pancreas. *Diabetes Technol. Ther.* **2005**, *7* (1), 28-47.
169. Peppas, N. A.; Huang, Y.; Torres-Lugo, M.; Ward, J. H.; Zhang, J., Physicochemical, foundations and structural design of hydrogels in medicine and biology. *Annu. Rev. Biomed. Eng.* **2000**, *2*, 9-29.
170. Gu, Z.; Dang, T. T.; Ma, M.; Tang, B. C.; Cheng, H.; Jiang, S.; Dong, Y.; Zhang, Y.; Anderson, D. G., Glucose-responsive microgels integrated with enzyme nanocapsules for closed-loop insulin delivery. *ACS Nano* **2013**, *7* (8), 6758-66.
171. Tai, W.; Mo, R.; Di, J.; Subramanian, V.; Gu, X.; Buse, J. B.; Gu, Z., Bio-inspired synthetic nanovesicles for glucose-responsive release of insulin. *Biomacromolecules* **2014**, *15* (10), 3495-502.

172. Podual, K.; Doyle Iii, F. J.; Peppas, N. A., Glucose-sensitivity of glucose oxidase-containing cationic copolymer hydrogels having poly(ethylene glycol) grafts. *J. Control. Release* **2000**, *67* (1), 9-17.
173. Podual, K.; Doyle, F. J.; Peppas, N. A., Preparation and dynamic response of cationic copolymer hydrogels containing glucose oxidase. *Polymer* **2000**, *41* (11), 3975-3983.
174. Zhang, K.; Wu, X. Y., Modulated insulin permeation across a glucose-sensitive polymeric composite membrane. *J. Control. Release* **2002**, *80* (1), 169-178.
175. Brooks, W. L. A.; Sumerlin, B. S., Synthesis and Applications of Boronic Acid-Containing Polymers: From Materials to Medicine. *Chem. Rev.* **2016**, *116* (3), 1375-1397.
176. Chou, D. H.; Webber, M. J.; Tang, B. C.; Lin, A. B.; Thapa, L. S.; Deng, D.; Truong, J. V.; Cortinas, A. B.; Langer, R.; Anderson, D. G., Glucose-responsive insulin activity by covalent modification with aliphatic phenylboronic acid conjugates. *Proc. Natl. Acad. Sci. U. S. A.* **2015**, *112* (8), 2401-6.
177. Kataoka, K.; Miyazaki, H.; Bunya, M.; Okano, T.; Sakurai, Y., Totally synthetic polymer gels responding to external glucose concentration: their preparation and application to on-off regulation of insulin release. *J. Am. Chem. Soc.* **1998**, *120* (48), 12694-12695.
178. Matsumoto, A.; Yoshida, R.; Kataoka, K., Glucose-responsive polymer gel bearing phenylborate derivative as a glucose-sensing moiety operating at the physiological pH. *Biomacromolecules* **2004**, *5* (3), 1038-1045.
179. Dong, Y.; Wang, W.; Veisoh, O.; Appel, E. A.; Xue, K.; Webber, M. J.; Tang, B. C.; Yang, X.-W.; Weir, G. C.; Langer, R.; Anderson, D. G., Injectable and glucose-responsive hydrogels based on boronic acid–glucose complexation. *Langmuir* **2016**, *32* (34), 8743-8747.

180. Matsumoto, A.; Kurata, T.; Shiino, D.; Kataoka, K., Swelling and shrinking kinetics of totally synthetic, glucose-responsive polymer gel bearing phenylborate derivative as a glucose-sensing moiety. *Macromolecules* **2004**, *37* (4), 1502-1510.
181. Shiino, D.; Murata, Y.; Kubo, A.; Kim, Y. J.; Kataoka, K.; Koyama, Y.; Kikuchi, A.; Yokoyama, M.; Sakurai, Y.; Okano, T., Amine containing phenylboronic acid gel for glucose-responsive insulin release under physiological pH. *J. Control. Release* **1995**, *37* (3), 269-276.
182. Obaidat, A. A.; Park, K., Characterization of glucose dependent gel-sol phase transition of the polymeric glucose-concanavalin A hydrogel system. *Pharmaceut. Res.* **1996**, *13* (7), 989-995.
183. Brownlee, M.; Cerami, A., Glycosylated insulin complexed to Concanavalin A. Biochemical basis for a closed-loop insulin delivery system. *Diabetes* **1983**, *32* (6), 499-504.
184. Brownlee, M.; Cerami, A., A glucose-controlled insulin-delivery system: semisynthetic insulin bound to lectin. *Science* **1979**, *206* (4423), 1190-1.
185. Liu, F.; Song, S. C.; Mix, D.; Baudyš, M.; Kim, S. W., Glucose-Induced release of glycosylpoly(ethylene glycol) insulin bound to a soluble conjugate of concanavalin A. *Bioconjug. Chem.* **1997**, *8* (5), 664-672.
186. Joel, S.; Turner, K. B.; Daunert, S., glucose recognition proteins for glucose sensing at physiological concentrations and temperatures. *ACS Chem. Biol.* **2014**, *9* (7), 1595-1602.
187. Wang, C.; Ye, Y. Q.; Sun, W. J.; Yu, J. C.; Wang, J. Q.; Lawrence, D. S.; Buse, J. B.; Gu, Z., Red Blood Cells for Glucose-Responsive Insulin Delivery. *Adv. Mater.* **2017**, *29* (18).

188. Gordijo, C. R.; Koulajian, K.; Shuhendler, A. J.; Bonifacio, L. D.; Huang, H. Y.; Chiang, S.; Ozin, G. A.; Giacca, A.; Wu, X. Y., Nanotechnology-enabled closed loop insulin delivery device: In vitro and in vivo evaluation of glucose-regulated insulin release for diabetes control. *Adv. Funct. Mater.* **2011**, *21* (1), 73-82.
189. Bratlie, K. M.; York, R. L.; Invernale, M. A.; Langer, R.; Anderson, D. G., Materials for diabetes therapeutics. *Adv. Healthc. Mater.* **2012**, *1* (3), 267-284.
190. Hassan, C. M.; Doyle, F. J.; Peppas, N. A., Dynamic behavior of glucose-responsive poly(methacrylic acid-g-ethylene glycol) hydrogels. *Macromolecules* **1997**, *30* (20), 6166-6173.
191. Bakh, N. A.; Cortinas, A. B.; Weiss, M. A.; Langer, R. S.; Anderson, D. G.; Gu, Z.; Dutta, S.; Strano, M. S., Glucose-responsive insulin by molecular and physical design. *Nat. Chem.* **2017**, *9* (10), 937-943.
192. Wong, C. M.; Wong, K. H.; Chen, X. D., Glucose oxidase: natural occurrence, function, properties and industrial applications. *Appl. Microbiol. Biotechnol.* **2008**, *78* (6), 927-38.
193. Broom, W. A.; Coulthard, C. E.; Gurd, M. R.; Sharpe, M. E., Some pharmacological and chemotherapeutic properties of notatin. *Br. J. Pharmacol. Chemother.* **1946**, *1* (4), 225-233.
194. Saravanakumar, G.; Kim, J.; Kim, W. J., Reactive-Oxygen-Species-Responsive Drug Delivery Systems: Promises and Challenges. *Adv. Sci.* **2016**.
195. Peppas, N. A.; Khademhosseini, A., Make better, safer biomaterials. *Nature* **2016**, *540* (7633), 335-336.
196. Yu, J.; Zhang, Y.; Kahkoska, A. R.; Gu, Z., Bioresponsive transcutaneous patches. *Curr. Opin. Biotechnol.* **2017**, *48*, 28-32.

197. Prausnitz, M. R., Engineering microneedle patches for vaccination and drug delivery to skin. *Annu. Rev. Chem. Biomol.* **2017**, *8*, 177-200.
198. De Duve, C.; Baudhuin, P., Peroxisomes (microbodies and related particles). *Physiol. Rev.* **1966**, *46* (2), 323-357.
199. Wang, J. Q.; Mao, W. W.; Lock, L. L.; Tang, J. B.; Sui, M. H.; Sun, W. L.; Cui, H. G.; Xu, D.; Shen, Y. Q., The role of micelle size in tumor accumulation, penetration, and treatment. *ACS Nano* **2015**, *9* (7), 7195-7206.
200. Liu, X.; Xiang, J.; Zhu, D.; Jiang, L.; Zhou, Z.; Tang, J.; Liu, X.; Huang, Y.; Shen, Y., Fusogenic reactive oxygen species triggered charge-reversal vector for effective gene delivery. *Adv. Mater.* **2016**, *28* (9), 1743-52.
201. Wintersteiner, O.; Abramson, H. A., The isoelectric point of insulin-electrical properties of adsorbed and crystalline insulin. *J. Biol. Chem.* **1933**, *99* (3), 741-753.
202. Scott, D.; Fisher, A., Studies on insulin with protamine. *J. Pharmacol. Exp. Ther.* **1936**, *58* (1), 78-92.
203. Park, W.; Kim, D.; Kang, H. C.; Bae, Y. H.; Na, K., Multi-arm histidine copolymer for controlled release of insulin from poly(lactide-co-glycolide) microsphere. *Biomaterials* **2012**, *33* (34), 8848-8857.
204. Piest, M.; Zhang, X.; Trinidad, J.; Engbersen, J. F., pH-responsive, dynamically restructuring hydrogels formed by reversible crosslinking of PVA with phenylboronic acid functionalised PPO-PEO-PPO spacers (Jeffamines®). *Soft Matter* **2011**, *7* (23), 11111-11118.
205. Springsteen, G.; Wang, B., A detailed examination of boronic acid-diol complexation. *Tetrahedron* **2002**, *58* (26), 5291-5300.

206. Yamamoto, Y.; Koma, H.; Yagami, T., Hydrogen peroxide mediated the neurotoxicity of an antibody against plasmalemmal neuronspecific enolase in primary cortical neurons. *Neurotoxicology* **2015**, *49*, 86-93.
207. Balkwill, F., Inflammation: a double-edged sword. *Eur. J. Cancer* **2006**, *42* (5), 571-571.
208. Lee, I. C.; He, J.-S.; Tsai, M.-T.; Lin, K.-C., Fabrication of a novel partially dissolving polymer microneedle patch for transdermal drug delivery. *J. Mater. Chem. B* **2015**, *3* (2), 276-285.
209. Olatunji, O.; Das, D. B.; Garland, M. J.; Belaid, L.; Donnelly, R. F., Influence of array interspacing on the force required for successful microneedle skin penetration: Theoretical and practical approaches. *J. Pharm. Sci.* **2013**, *102* (4), 1209-1221.
210. Davis, S. P.; Landis, B. J.; Adams, Z. H.; Allen, M. G.; Prausnitz, M. R., Insertion of microneedles into skin: measurement and prediction of insertion force and needle fracture force. *J. Biomech.* **2004**, *37* (8), 1155-1163.
211. Thennadil, S. N.; Rennert, J. L.; Wenzel, B. J.; Hazen, K. H.; Ruchti, T. L.; Block, M. B., Comparison of glucose concentration in interstitial fluid, and capillary and venous blood during rapid changes in blood glucose levels. *Diabetes Technol. Ther.* **2001**, *3* (3), 357-65.
212. Liu, Y.; Du, J.; Yan, M.; Lau, M. Y.; Hu, J.; Han, H.; Yang, O. O.; Liang, S.; Wei, W.; Wang, H.; Li, J.; Zhu, X.; Shi, L.; Chen, W.; Ji, C.; Lu, Y., Biomimetic enzyme nanocomplexes and their use as antidotes and preventive measures for alcohol intoxication. *Nat. Nano.* **2013**, *8* (3), 187-192.